



國立臺灣大學理學院大氣科學研究所

碩士論文

Graduate Institute of Atmospheric Sciences

College of Science

National Taiwan University

Master Thesis

在不同水文氣候特徵下

農業灌溉對陸地-大氣耦合強度之影響

Impacts of Agricultural Irrigation on Land-Atmosphere

Coupling Strength Under Different Hydroclimatological

Characteristics

廖淇雅

Chi-Ya Liao

指導教授：羅敏輝博士、莊振義博士

Advisor: Min-Hui Lo, Ph.D.; Jehn-Yih Juang, Ph.D.

中華民國 107 年 6 月

June 2018

國立臺灣大學碩士學位論文 口試委員會審定書

本論文係 廖淇雅 君 (學號 R05229005) 在國立臺灣大學大氣科學學系、所完成之碩士學位論文，於民國 107 年 6 月 13 日承下列考試委員審查通過及口試及格，特此證明

口試委員：

邱敏如 吳瑞美 (簽名)

(指導教授)

陳奕穎 _____

陳佳正 _____

系主任、所長

林+子雄 (簽名)




摘要

陸地大氣交互作用的「熱點」，也就是土壤濕度距平對當地降雨有顯著影響的位置，通常被發現位於乾燥與潮濕氣候交界之過渡帶。在這些熱點，地表蒸發散仍然受到可用水量的限制，因為此時可用能量比可用水量多，但同時蒸發散的實際量值也大到足以影響當地大氣的穩定度。陸地大氣交互作用的強度隨水文氣候而不同，顯示出它和兩個蒸發散的限制因素(地表可用水量和可用能量)之間的競爭有顯著關係。

近來由於灌溉的廣大面積與高用水量，灌溉對氣候的影響受到許多關注，例如對地表溫度、地表通量、大氣環流和降雨的影響。此外，灌溉對陸地大氣交互作用的影響也是其中一個氣候議題。陸地大氣交互作用強度的改變是重要且值得關注的，因為交互作用強度的減弱可能會使次季節降雨的可預報程度隨之降低。過去有研究發現在亞馬遜雨林和美國中部大平原的灌溉會導致陸地大氣交互作用強度的減弱。然而其中的機制以及灌溉是否在其他地區也會同樣導致陸地大氣交互作用的減弱仍然不清楚。本研究比較在五個不同的灌溉區域(北印度、中國華北平原、西南歐、美國中部大平原和中亞)之間，灌溉對陸地大氣交互作用的影響有何不同。本研究同時使用陸地模式和陸地大氣耦合模式，目的在探討灌溉對地表直接的影響(例如:地表通量的改變)和後續影響到陸地大氣交互作用。此外，我們使用三種陸地大氣交互作用指數以表示陸地影響大氣的三個過程:(一)土壤濕度和蒸發散的關係、(二)地表可感熱通量和邊界層高度的關係以及(三)蒸發散和降雨量的關係。

陸地模式和陸地大氣耦合模式的結果皆顯示在不同的水文氣候下，灌溉能夠增強或減弱陸地大氣交互作用。在陸地模式中由於固定的大氣邊界條件，灌溉造成的變化能夠被當地的水文氣候特徵清楚解釋。在乾燥情況之下，灌溉傾向增強陸地大氣交互作用；在半乾燥及潮濕情況之下，灌溉傾向減弱陸地大氣交互作用。

然而在陸地大氣耦合模式中的模擬結果和陸地模式不同，原因來自大氣的變化及回饋作用。在五個灌溉區中，大部分的情況下灌溉的冷卻效應導致大氣的沉降



距平以及水氣通量的低層水平輻散，除了中國華北平原的夏季初期。由於夏季初期中國華北平原極度潮濕，灌溉後地表蒸發散的增加和冷卻效應皆不顯著。該特性可能進一步抑制灌溉當地直接藉由地表通量變化改變大氣的訊號，相對的使大尺度大氣環流改變的訊號較顯著。大氣環流對灌溉的反應會改變降雨，並對地面可用水量形成回饋作用。此外，地表可用能量也會被大氣環流影響，主要藉由雲和大氣溫度的改變。雖然灌溉前後的陸地大氣交互作用的強度皆顯示出相同的隨水文氣候特徵變化的趨勢，蒸發散可用能量與可用水量的改變卻無法只以當地的水文氣候解釋，因為它們同時被灌溉和大氣環流改變的回饋作用影響。大氣環流在時、空上的變異性也需要被納入分析。

總結來說，本研究結果顯示出灌溉對陸氣交互作用的潛在影響，雖然單以水文氣候特徵的不同無法清楚的解釋所有過程，需要同時考慮大氣的回饋作用。本研究的結論可以被延伸應用在陸地大氣交互作用在聖嬰/反聖嬰現象或氣候變遷下的變化，因為降雨或能量的改變可能和灌溉有類似的效應。

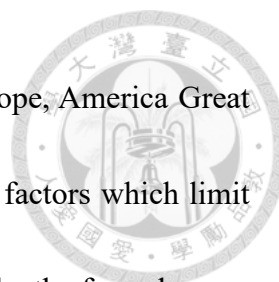
關鍵字: 陸地大氣交互作用、農業灌溉、水文氣候、土壤濕度、地表蒸發散限制因素、蒸發散可用水量(能量)

Abstract



The “hot spots” of land-atmosphere coupling (LAC), where soil moisture anomalies strongly affect local precipitation, are usually found in the transition zones between wet and dry climates. The evapotranspiration of these transition zones is mainly limited by the available water because the available energy is more than the available water, but at the same time, the evapotranspiration is large enough to affect the local atmospheric stability. LAC’s dependence on hydroclimate indicates that LAC strongly relates to competition between two limiting factors on surface evapotranspiration: the available energy and the available water.

Recently, the impacts of agricultural irrigation on climate, including the aspects of surface temperature, surface fluxes, atmospheric circulation, and precipitation, have gained lots of attention due to irrigation’s large area and magnitude. In addition, the impacts of irrigation on LAC is also a crucial climate issue. The shift of LAC is an important issue since if the strength of LAC is weakened, the predictability of sub-seasonal precipitation might decline. Two studies in Amazon and the Great Plains of America both show that irrigation results in the decrease of the LAC. However, the mechanisms behind and whether the irrigation process can lead to the overall reduction of the coupling strength worldwide remain unclear. This study aims to compare the differences of irrigation’s impact on LAC among five selected locations undergoing

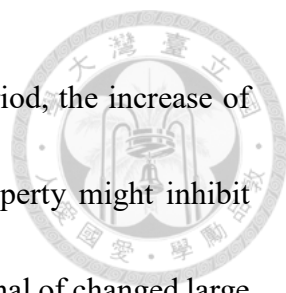


intensive irrigation: North India, North China Plain, Southwest Europe, America Great Plains and Middle East. The spatial and temporal differences of the factors which limit evapotranspiration (i.e., either by the available energy or water) will be the focus here.

Both offline land surface model simulations and coupled land-atmosphere simulations of Community Earth System Model (CESM) are used to explore the direct changes and the subsequent shifts in land-atmosphere interactions. Also, three coupling indices (including the relationships between changes in soil moisture and evapotranspiration; sensible heat flux and boundary layer height; evapotranspiration and precipitation) are adopted to quantify the coupling strength between the land and the atmosphere.

Results from both offline and coupled simulations imply that irrigation can weaken or strengthen the LAC under different mean hydroclimate. In offline simulations, because of fixed atmospheric boundary condition, the impact could be explained well by hydroclimatological characteristics. Under dry conditions, irrigation tends to increase LAC; in contrast, under semiarid and wet conditions, irrigation tends to decline LAC.

However, the changes of LAC are different between offline simulations and coupled land-atmosphere simulations due to the feedbacks from the atmosphere. Mostly the cooling effect of irrigation causes subsidence and further the low-level divergence of water vapor, except for North China Plain during early summer among the five



simulations. Since North China Plain is the wettest place in this period, the increase of evapotranspiration and surface cooling is less significant. This property might inhibit local irrigation signal and contrarily more significantly reflect the signal of changed large scale circulation. Thus, the atmospheric response leads to changes in precipitation and cause feedbacks on the available water. In addition, the available energy is also affected by the atmospheric circulation through changes in cloud and temperature. The LAC before and after irrigation show similar characteristics with the hydroclimate. However, the conversion of the available energy and water for evapotranspiration, which results from both irrigation and its subsequent shifts of atmospheric circulation, could not be explained perfectly only by their original hydroclimatology characteristics. The temporal and spatial diversity of atmospheric circulation also contribute to these differences.

In sum, the results of this study show the potential response of LAC after irrigation although the local hydroclimate could not explain all the process perfectly, and the atmospheric feedback should be considered. The conclusion could be applied to the shift of LAC under ENSO and climate changes because the alteration of precipitation and/or energy may have similar effects as irrigation does.

Key Words: land-atmosphere coupling, agricultural irrigation, hydroclimate, soil moisture, surface evaporation limitation, available water (energy) of evapotranspiration

Contents



口試委員會審定書	I
摘要	II
Abstract.....	IV
Contents	VII
Figure captions	IX
Table captions.....	XVI
Chapter 1 Introduction.....	1
1.1 The limitations of surface evapotranspiration	1
1.2 Land-atmosphere coupling	1
1.3 Agricultural irrigation’s impact on land-atmosphere coupling.....	4
1.4 The scientific question of this study	6
Chapter 2 Methodology	8
2.1 Irrigation area and intensity	8
2.2 Model setup.....	10
2.3 Land-atmosphere coupling indices	11
2.4 Hydroclimatological characteristics	14
2.5 Budget analyses	16
Chapter 3 Results.....	18
3.1 Relationships between land-atmosphere coupling and local hydroclimates.....	18
3.2 Irrigation’s impact on land-atmosphere coupling in offline simulations.....	20
3.3 Irrigation’s impact on land-atmosphere coupling in coupled simulations.....	23
Chapter 4 Summary, discussion and future work.....	28
4.1 Summary	28
4.2 Discussion.....	30
4.3 Future work and application	32
References	37
Figures	42

Tables 87



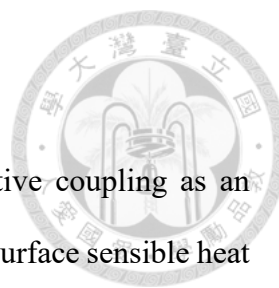
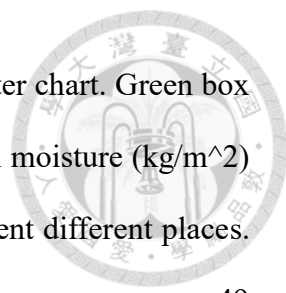


Figure captions

- Figure 1.1** The illustration of the land-atmosphere coupling (positive coupling as an example) adopted in this study. LE: surface latent heat flux; SH: surface sensible heat flux; θ_e : equivalent potential temperature; Δx : the change of x..... 42
- Figure 1.2** Global irrigation map of 2001~2010 average according to Wada and Bierkens (2014). Irrigation unit: \log_{10} (mm/month). 43
- Figure 2.1** Five intense irrigation areas targeted from a monthly irrigation intensity data set derived by Wada and Bierkens (2014): North India (location No 1), North China Plain (location No 3), America Great Plains (location No 4), Southwest Europe (location No 5) and Middle East (location No 6). Purple areas are the original region of significant agricultural irrigation; Red boxes are simulated irrigation region in the model. 44
- Figure 2.2** Climatology of monthly irrigation intensity of five selected locations between 2001 to 2010. 45
- Figure 2.3** Climatology of monthly irrigation intensity of three selected locations between 2001 to 2010. Curves of Central Asia (location No 4) and Europe(location No 5) are combined into “minimum of irrigation intensity seasonal cycle”. Also, “maximum of irrigation intensity seasonal cycle” is defined. 46
- Figure 2.4** Standard deviation of monthly area averaged precipitation among 25 years in F_{ctl} 47
- Figure 2.5** Scatter plot of surface net radiation and the FAO grass reference evapotranspiration (PET) in F_{ctl} . The climatological monthly data from five irrigation areas are shown. Different symbols dots represent different places. The black dashed line represents the same magnitude between net radiation and PET. 48
- Figure 2.6** Seasonal cycle of (a) America Great Plains (location No 4) and (b) five



irrigation areas in F_{ctl} as examples of hydroclimatological scatter chart. Green box stands for data under higher net radiation. X axis: top 10 cm soil moisture (kg/m^2) of F_{ctl} ; Y axis: net radiation of F_{ctl} . Different symbols represent different places.

..... 49

Figure 2.7.1 The differences of vertically integrated moisture (blue) and evapotranspiration minus precipitation (red) after irrigation: $F_{self} - F_{ctl}$. X axis: month. 50

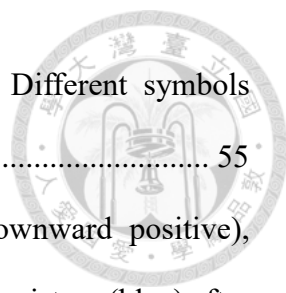
Figure 2.7.2 The differences of vertically integrated moisture (blue) and evapotranspiration minus precipitation (red) after irrigation: $F_{max} - F_{ctl}$. X axis: month. 51

Figure 3.1.1 Hydroclimatological scatter chart of I_{LE} from F_{ctl} . (a) I_{LE} (W/m^2): coupling strength between soil moisture and evapotranspiration, (b) β_{LE} ($(W/m^2)/(kg/m^2)$): the slope between soil moisture and evapotranspiration, (c) S_w (kg/m^2): the standard deviation of daily soil moisture. Different symbols represent different places. 52

Figure 3.1.2 Hydroclimatological scatter chart of I_{LE} from I_{ctl} . (a) I_{LE} (W/m^2): coupling strength between soil moisture and evapotranspiration, (b) β_{LE} ($(W/m^2)/(kg/m^2)$): the slope between soil moisture and evapotranspiration, (c) S_w (kg/m^2): the standard deviation of daily soil moisture. Different symbols represent different places. 53

Figure 3.2 Hydroclimatological scatter chart of I_p , the coupling between evapotranspiration and precipitation, from F_{ctl} . Different symbols represent different places. 54

Figure 3.3 Hydroclimatological scatter chart of I_{PBLH} from F_{ctl} . (a) I_{PBLH} (m): coupling strength between sensible heat flux and boundary layer height, (b) β_{PBLH} ($m/(W/m^2)$): the slope between sensible heat flux and boundary layer height, (c) S_s



(W/m^2): the standard deviation of daily sensible heat flux. Different symbols represent different places. 55

Figure 3.4.1 The differences of surface net radiation (green, downward positive), evapotranspiration (orange, upward positive) and top 10 cm soil moisture (blue) after irrigation: $I_{max} - I_{ctl}$. X axis: month. 56

Figure 3.4.2 The differences of surface net radiation (green, downward positive), evapotranspiration (orange, upward positive) and top 10 cm soil moisture (blue) after irrigation: $I_{self} - I_{ctl}$. X axis: month. 57

Figure 3.4.3 The differences of surface net radiation (green, downward positive), evapotranspiration (orange, upward positive) and top 10 cm soil moisture (blue) after irrigation: $I_{min} - I_{ctl}$. X axis: month. 58

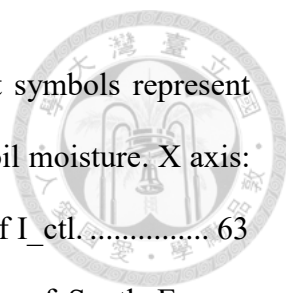
Figure 3.5 Hydroclimatological scatter chart of Δ evapotranspiration/ Δ irrigation (unitless). (a) $I_{max} - I_{ctl}$, (b) $I_{self} - I_{ctl}$, (c) $I_{min} - I_{ctl}$. X axis: top 10 cm soil moisture (kg/m^2) of I_{ctl} ; Y axis: net radiation of I_{ctl} 59

Figure 3.6 Hydroclimatological scatter chart of Δ soil moisture of top 10 cm depth/ Δ irrigation ($(kg/m^2)/(W/m^2)$). (a) $I_{max} - I_{ctl}$, (b) $I_{self} - I_{ctl}$, (c) $I_{min} - I_{ctl}$. X axis: top 10 cm soil moisture (kg/m^2) of I_{ctl} ; Y axis: net radiation of I_{ctl} 60

Figure 3.7.1 Hydroclimatological scatter chart of $\Delta I_{LE}/\Delta sm_{10}$ ($(W/m^2)/(kg/m^2)$): (a) $I_{max} - I_{ctl}$, (b) $I_{self} - I_{ctl}$, (c) $I_{min} - I_{ctl}$. Different symbols represent different places. Δsm_{10} represents change of top 10 cm depth soil moisture. X axis: top 10 cm soil moisture (kg/m^2) of I_{ctl} ; Y axis: net radiation of I_{ctl} 61

Figure 3.7.2 Hydroclimatological scatter chart of $\Delta \beta_{LE} / \Delta sm_{10}$ ($(W/m^2)/(kg/m^2)^2$) after irrigation: (a) $I_{max} - I_{ctl}$, (b) $I_{self} - I_{ctl}$, (c) $I_{min} - I_{ctl}$. Different symbols represent different places. Δsm_{10} represents change of top 10 cm depth soil moisture. X axis: top 10 cm soil moisture (kg/m^2) of I_{ctl} ; Y axis: net radiation of I_{ctl} 62

Figure 3.7.3 Hydroclimatological scatter chart of $\Delta S_w / \Delta sm_{10}$ (unitless) after irrigation:



(a) $I_{max} - I_{ctl}$, (b) $I_{self} - I_{ctl}$, (c) $I_{min} - I_{ctl}$. Different symbols represent different places. Δsm_{10} represents change of top 10 cm depth soil moisture. X axis: top 10 cm soil moisture (kg/m^2) of I_{ctl} ; Y axis: net radiation of I_{ctl} 63

Figure 3.8 The probability density function of daily soil moisture of South Europe (location No 5) over 25 years from November to February. Blue line: I_{ctl} ; red line: I_{max} . Data corresponds to orange circle in Figure 3.7.3(a). 64

Figure 3.9.1 Differences after irrigation: $F_{self} - F_{ctl}$. (a) precipitation, (b) net radiation, (c) I_{LE} , (d) I_P , (e) I_{PBLH} . The color of dots represent month. At each location, data approaching to left X axis represent earlier month, corresponding to the shaded color. 65

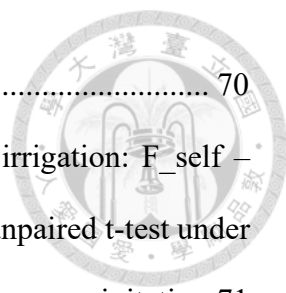
Figure 3.9.2 Differences after irrigation: $F_{max} - F_{ctl}$. (a) precipitation, (b) net radiation, (c) I_{LE} , (d) I_P , (e) I_{PBLH} . The color of dots represent month. At each location, data approaching to left X axis represent earlier month, corresponding to the shaded color. 66

Figure 3.10 Hydroclimatological scatter chart of seasonal mean from F_{ctl} . Red dots: JJA; blue dots: DJF. Numbers represent the magnitude of surface cooling effect (green), moistening effect (purple) and total effect (pink) of $F_{max} - F_{ctl}$. Note that during the same season, irrigated water is same among five areas; also, the irrigation in JJA is stronger than DJF (Figure 2.3). 67

Figure 3.11.1 The differences of MSE vertical structure in JJA after irrigation: $F_{max} - F_{ctl}$ 68

Figure 3.11.2 The differences of MSE vertical structure in DJF after irrigation: $F_{max} - F_{ctl}$ 69

Figure 3.12 Atmospheric column water budget analysis of F_{ctl} : evapotranspiration (upward positive) minus precipitation (downward positive). Negative value indicates non-local water vapor sources for precipitation. X axis: month. LE:



evapotranspiration; prec.: precipitation. 70

Figure 3.13.1 Atmospheric column water budget differences after irrigation: $F_{self} - F_{ctl}$. Black and blue dots represent that the difference pass the unpaired t-test under 95% significant level. X axis: month. LE: evapotranspiration; prec.: precipitation. 71

Figure 3.13.2 Atmospheric column water budget differences after irrigation: $F_{max} - F_{ctl}$. Black and blue dots represent that the differences pass the unpaired t-test under 95% significant level. X axis: month. LE: evapotranspiration; prec.: precipitation. 72

Figure 3.14 Annual mean omega differences after irrigation. (a) $F_{self} - F_{ctl}$, (b) $F_{max} - F_{ctl}$ 73

Figure 3.15 Omega differences after irrigation in North China Plain (location No 3). (a) May to August of $F_{self} - F_{ctl}$, (b) May and June of $F_{max} - F_{ctl}$. Corresponding to blue box in Figure 3.13. 74

Figure 3.16.1 The differences of annual mean evapotranspiration (positive upward) after irrigation: $F_{self} - F_{ctl}$. Black crosses represent annual data which pass the unpaired two-tail t-test under 95% significant level. Green box represents irrigated area in simulations. 75

Figure 3.16.2 The differences of annual mean evapotranspiration (positive upward) after irrigation: $F_{max} - F_{ctl}$. Black crosses represent annual data which pass the unpaired two-tail t-test under 95% significant level. Green box represents irrigated area in simulations. 76

Figure 3.17 The differences of water vapor flux at 850mb from $F_{max} - F_{ctl}$ in (a) May and (b) June. Vector: water vapor flux (m/s) anomaly; shaded: the divergence of water vapor flux (10^{-9} 1/s) anomaly. Green box represents the irrigation area. 77

Figure 3.18 The differences of precipitation (W/m^2) from $F_{max} - F_{ctl}$ in (a) May and (b) June. Black crosses represent annual data which pass the unpaired two-tail t-test under 95% significant level. Green box represents the irrigation area. 78

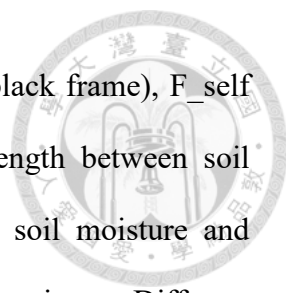


Figure 3.19 Hydroclimatological scatter chart of I_{LE} from F_ctl (black frame), F_self (blue frame) and F_max (pink frame). (a) I_{LE} : coupling strength between soil moisture and evapotranspiration, (b) β_{LE} : the slope between soil moisture and evapotranspiration, (c) S_w : the standard deviation of daily soil moisture. Different symbols represent different places. Color of frame represent different simulations. 79

Figure 3.20 Hydroclimatological scatter chart of I_{PBLH} from F_ctl (black frame), F_self (blue frame) and F_max (pink frame). (a) I_{PBLH} : coupling strength between sensible heat flux and boundary layer height, (b) β_{PBLH} : the slope between sensible heat flux and boundary layer height, (c) S_s : the standard deviation of daily sensible heat flux. Different symbols represent different places. Color of frame represent different simulations. 80

Figure 3.21 Hydroclimatological scatter chart of I_p from F_ctl (black frame), F_self (blue frame) and F_max (pink frame). Different symbols represent different places. Color of frame represent different simulations. 81

Figure 4.1 The illustration of the strength of three land-atmosphere coupling indices (I_{LE} , I_{PBLH} and I_p) and their controlling factors: (a) I_{LE} , (b) I_{PBLH} , (c) I_p . The shift of red dot represents the response of coupling strength due to the change of controlling factors. Blue line represents the changing tendency (i.e., increase or decrease) of coupling index among the shift of the controlling factors, but it does not guarantee “linear” shift of coupling strength. 82

Figure 4.2 The illustration of the responses of land surface fluxes and atmosphere structure with more available water under different hydroclimatological characteristics: (a) approaching to the water-limit condition, (b) the transition zone and (c) approaching to the energy-limit condition. LE: surface latent heat flux; SH: surface sensible heat flux. 83

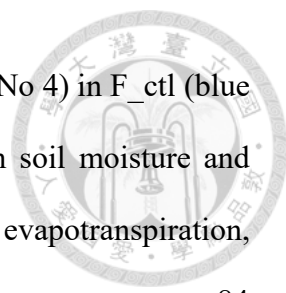


Figure 4.3 Seasonal cycle of I_{LE} in America Great Plains (location No 4) in F_ctl (blue line) and F_Self (red line). (a) I_{LE} : coupling strength between soil moisture and evapotranspiration, (b) β_{LE} : the slope between soil moisture and evapotranspiration, (c) S_w : the standard deviation of daily soil moisture. 84

Figure 4.4 Seasonal cycle of I_{PBLH} in America Great Plains (location No 4) in F_ctl (blue line) and F_Self (red line). (a) I_{PBLH} : coupling strength between sensible heat flux and boundary layer height, (b) β_{PBLH} : the slope between sensible heat flux and boundary layer height, (c) S_s : the standard deviation of daily sensible heat flux... 85

Figure 4.5 Anomaly of (a) precipitation and (b) surface net radiation during El Niño in 1997 and 1998. Reference climatology is calculated from 1984 to 2010. Precipitation comes from GPCP reanalysis data; net radiation comes from ECMWF reanalysis data. 86

Table captions

Table 2.1 The abbreviation of each simulation settings..... 87




Chapter 1 Introduction



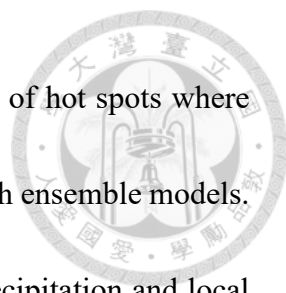
1.1 The limitations of surface evapotranspiration

The Budyko curve (Budyko, 1961) displays a concept that the magnitude of surface evapotranspiration is limited mainly by the availabilities of energy and water. Under wet (dry) conditions, evapotranspiration is primarily controlled by the available energy (water), which can be defined as energy-limit (water-limit) condition. Precipitation and soil moisture are often used as the representation of the available water; net radiation and potential evapotranspiration are often used to express the available energy. Two limitations of evapotranspiration imply that the response of evapotranspiration may be diverse based on different hydroclimatological characteristics. For example, Jung et al. (2010) found that in 1998, terrestrial evapotranspiration in southern hemisphere was primarily limited by land moisture supply, corresponding to the observed soil moisture decrease mainly in Africa and Australia. Miralles et al. (2013) discussed that the increased continental evapotranspiration in the northern hemisphere is strongly related to the increased atmosphere water demand due to the positive temperature trend. Evapotranspiration was inhibited by decreased precipitation during El Niño at several regions of the land.

1.2 Land-atmosphere coupling




Land-atmosphere coupling considered in this study indicates the dependence of precipitation on local soil moisture at sub-seasonal to seasonal time scale. First, soil moisture might affect the surface energy budget and the partition between surface latent heat flux and sensible heat flux. With higher soil moisture, mostly the magnitude of latent heat flux becomes larger, causing moistening effect (the increase of water vapor) and cooling effect (the decrease of temperature) of near surface atmosphere simultaneously (Figure 1.1). When the moistening effect dominates, atmosphere tends to become convection instability and favors moist convection, which may lead to increased precipitation. With a strong positive land-atmosphere coupling, higher soil moisture results in more local precipitation. Further, more local precipitation will cause the increase of soil moisture and establish a positive feedback between soil moisture and local precipitation. In contrast, when the cooling effect dominates, atmosphere favors subsidence and less precipitation, displaying a negative land-atmosphere coupling. In this study, three indices are used for the quantification of different procedure of land-atmosphere coupling: soil moisture's impact on surface fluxes, surface fluxes' impact on boundary layer and surface fluxes' impact on precipitation. Land-atmosphere coupling has been widely discussed, because, besides the ocean, land surface is also regarded as an important driver for the atmosphere. Findell and Eltahir (1997) tested the hypothesis that soil moisture might have positive influences on subsequent precipitation by observation



data from Illinois. Koster et al. (2004) stated the spatial distribution of hot spots where precipitation was strongly affected by soil moisture anomalies through ensemble models. Zeng et al. (2010) proposed an index based on the covariance of precipitation and local evapotranspiration to quantify the strength of land-atmosphere coupling. Dirmeyer (2011) defined a terrestrial coupling strength, representing the influence of soil moisture variations on surface fluxes and found similar spatial patterns to that of Koster et al. (2004). Mei and Wang (2011) examined the impact of soil moisture on terrestrial precipitation and found diverse coupling strength among different sea surface pattern and precipitation amount. Tuttle and Salvucci (2016) also found that soil moisture anomalies could strongly affect precipitation under specific conditions with the dependence on regional aridity through the analysis of observed data in the United States.

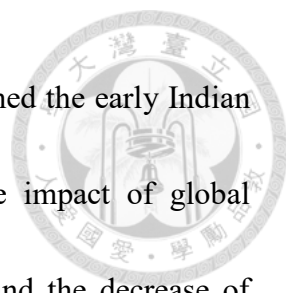
Since the slow variation of land surface characteristics (such as deeper soil moisture and groundwater) can be predicted weeks to months in advance, land-atmosphere coupling may contribute toward the improvement in seasonal climate forecasts. The strength of land-atmosphere coupling strongly relates to two limitations of surface evapotranspiration: the available water and energy. Thus, the “hot spots” of land-atmosphere coupling, where soil moisture anomalies strongly affect local precipitation, are found in the transition zones between wet and dry climates (Dirmeyer, 2011; Koster et al., 2004). The evapotranspiration of these transition zones is limited by the available



water, but at the same time, the surface latent heat flux is large enough to affect the local atmospheric stability (Koster et al., 2004). With the foundation that the different land-atmosphere coupling strength results from the competing effect between the available energy and water, the shift of the available energy and water might alter land-atmosphere coupling.

1.3 Agricultural irrigation's impact on land-atmosphere coupling

Agricultural irrigation is an artificial process adding excessive water to land surface in order to grow crops. Due to irrigation's rapid expansion of land area and magnitude, it is regarded as one of the major forcing causing climate changes in the 20th century (DeFries et al., 2004; Diffenbaugh, 2009; Green et al., 2005; Hirsch et al., 2015; Mahmood et al., 2014; Matson et al., 1997; McDermid et al., 2017; Pielke et al., 2011; Quesada et al., 2017; Ramankutty et al., 2008; Sacks et al., 2009). Irrigation occurs intensely in India, North China Plain, Southwest and Eastern Europe, California, Great Plains, and Middle East (Figure 1.2). Recently, the impacts of irrigation on climate have gained much attention, including the changes of surface temperature, surface fluxes, atmospheric circulation, precipitation and its impacts on land-atmosphere coupling. For example, Douglas et al. (2006) explored that irrigation caused the increase of evapotranspiration in India and such increase was more significant during dry season. Lee



et al. (2009) found that irrigation prior to the India monsoon weakened the early Indian summer monsoon rainfall. Puma and Cook (2010) examined the impact of global historical time-varying irrigation by ensemble simulations and found the decrease of temperature in boreal summer and warming in boreal winter; also, the global precipitation pattern was changed. Harding and Snyder (2012a) discovered that over the Great Plains of America, irrigation might cause different precipitation responses between drought and pluvial years, suggesting that there might be a threshold of soil moisture for triggering convection. They also revealed that the heavy irrigation-induced precipitation corresponded to the observation; in addition, only about 16% of the irrigation-induced evapotranspiration turned into local precipitation, reducing water source over the Great Plains (Harding and Snyder, 2012b). According to Lo and Famiglietti (2013), irrigation in California's Central Valley strengthened the magnitude of evapotranspiration and downwind water vapor transport, enhancing the regional hydrological cycle. Also, irrigation in California's Central Valley cooled the surface and decreased the land-sea temperature contrast, resulting in a weaker sea breeze and less stratocumulus cloud covers over the eastern Pacific subtropical oceans (Lo et al., 2013). Wey et al. (2015) argued that the irrigation over Asian low-latitude regions strengthens the land-sea thermal contrast and monsoon circulation during winter; at the same time, the irrigation caused teleconnection over Aleutian low and North America. Alter et al. (2018) discussed that

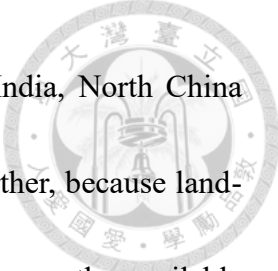
the increased observation of precipitation and humidity and the decreased temperature in the central United States is strongly related to the agricultural irrigation.



The impact of irrigation on land-atmosphere coupling is a salient issue because the weakening of local land-atmosphere coupling strength might further decrease the predictability of sub-seasonal precipitation. Badger and Dirmeyer (2015) analyzed the climate response of Amazon forest replacement by crop with the consideration of irrigation in fully coupled Earth system model, discovering negative effects of adding irrigation water magnitude on the coupling between soil moisture and latent heat flux. In addition, Lu et al. (2017) found remarkable decrease in land-atmosphere coupling strength with the increase in irrigated cropland percentage in the Great Plains of America from May to September. Thus, two studies in Amazon and the Great Plains of America revealed that irrigation is possible to affect land-atmosphere coupling strength via alternating the regional hydroclimatology. However, whether the irrigation process can lead to the overall reduction of the coupling strength worldwide and the mechanisms behind it remain unclear.

1.4 The scientific question of this study

Since irrigation's impact on land-atmosphere coupling is an important issue and only few locations were researched, this study aims to explore irrigation's impact on land-



atmosphere coupling among five intensive irrigation areas: North India, North China Plain, Southwest Europe, America Great Plains and Middle East. Further, because land-atmosphere coupling strength strongly relates to the competing between the available energy and the available water, whether hydroclimatological characteristics can be used to explain the diverse response of land-atmosphere coupling toward irrigation are also investigated. Both offline land surface model simulations and coupled land-atmosphere simulations of Community Earth System Model are used. In offline land surface model simulations, the direct change of land surface and surface fluxes can be investigated. In coupled land-atmosphere simulations, besides the direct change of land surface and surface fluxes, the subsequent shifts in the atmosphere can also be investigated. The shifts in the atmosphere include the boundary layer development, the vertical structure of moist static energy, atmospheric circulation, cloud and precipitation. Also, three coupling indices I_{LE} , I_{PBLH} and I_P (referring to the relationships between changes in soil moisture and evapotranspiration; sensible heat flux and boundary layer height; evapotranspiration and precipitation) are adopted to quantify different coupling processes between the land and the atmosphere.

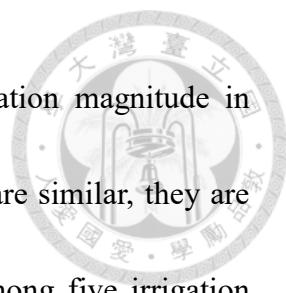


Chapter 2 Methodology

2.1 Irrigation area and intensity

To examine the potential effects of irrigation, five irrigation areas (purple areas in Figure 2.1) are targeted from a monthly irrigation intensity data set, which was estimated from both water balance model and observations, derived by Wada and Bierkens (2014). The original grid size of irrigation data is 0.5°lon by 0.5°lat and is interpolated into 1.25°lon by 0.9°lat (approximately 120 km by 100 km near the equator) to be consistent with the model grid size. Originally six irrigation areas are selected, but considering computational resources, South India (location No 2) is not simulated due to its similarity of climate to North India (location No 1). Because previous studies have described the influence of land use change area on its response to climate (Chagnon, 2005; Ho, 2017; Khanna et al., 2017; Lawrence and Vandecar, 2014), the irrigation areas in model experiments are fixed to a rectangle with 15 grids (three grids by five grids) according to the smallest irrigation grids among five locations (red boxes in Figure 2.1). The orientation of rectangles is determined according to its original shape and irrigation pattern in Figure 1.2. The orientation of rectangle might slightly change the results due to spatial heterogeneity of land surface but it is ignored and not discussed in this study.

Climatology of monthly irrigation intensity of each location (purple areas in Figure 2.1) between 2001 to 2010 is calculated (Figure 2.2) and used as the input forcing of



model experimental simulation. Since the seasonal cycle of irrigation magnitude in America Great Plains (location No 4) and Europe (location No 5) are similar, they are combined into “minimum of irrigation intensity seasonal cycle among five irrigation areas”. Also, “maximum of irrigation intensity seasonal cycle among five irrigation areas” is defined to simulate the most intense situation (Figure 2.3). Considering the possible range of irrigation intensity, each location undergoes three different irrigation scenarios in offline land surface model simulations: maximum, minimum and their own climatology irrigation intensity seasonal cycle; each location undergoes two different irrigation scenarios in coupled land-atmosphere simulations: maximum and their own climatology seasonal cycle (Figure 2.3). Table 2.1 shows the abbreviation of each simulation setting. When applying the same irrigation management in the experiment, the influences caused by different irrigation magnitude could be excluded. Thus, the maximum and minimum of irrigation intensity among five irrigation areas are used although they may be unrealistic at some experimental places. For each grid, irrigation water is treated as effective precipitation, and added directly to the top of the soil layer in Community Land Model. Irrigated water comes from three local sources: unsaturated soil water and groundwater (one fourth of irrigation), unconfined aquifer (one fourth of irrigation) and confined aquifer (one half of irrigation). Because confined aquifer is not originally included in the water cycle of Community Land Model, the total water in the

model would increase after our irrigation strategy is applied.

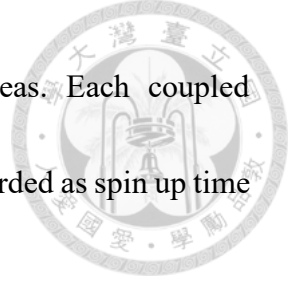


2.2 Model setup

Community Earth System Model (CESM), an atmospheric general circulation model, is used in this study. To distinguish the direct changes caused by irrigation and the indirect effect after coupling with the atmosphere, the model simulations are separated into two parts: offline simulations (Community Land Model 4.0, CLM) and coupled land-atmosphere simulations (CLM coupled with Community Atmosphere Model 5, CAM). Community Land Model has 10 vertical layers of soil; Community Atmosphere Model has 37 vertical layers of atmosphere. Each simulation has the grid size of 1.25°lon by 0.9°lat and integral time step of 30 minutes.

In offline simulation, atmospheric forcing taken from NCAR Reanalysis and Climatic Research Unit (CRU) is used as the atmospheric boundary condition of CLM, including solar radiation, precipitation, temperature, pressure, humidity and wind. Thirty years (1980 to 2009) of forcing is used and repeated once, meaning that each offline simulation has the length of 60 years. Output data of last 25 years are selected for analysis.

In coupled simulation, CAM is coupled with CLM under atmospheric greenhouse gas concentration of year 2000. In addition, ocean is prescribed by climatological sea surface temperature. Irrigation processes in five locations are simulated separately to



exclude non-linear effect and teleconnection among irrigated areas. Each coupled simulation is conducted for 30 years, of which first five years are regarded as spin up time and last 25 years are included in analysis.

2.3 Land-atmosphere coupling indices

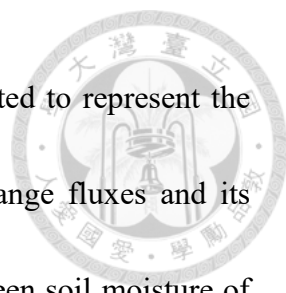
Three coupling indices derived by Dirmeyer (2011) and Zeng et al. (2010) are adopted to quantify the coupling strength between the land and the atmosphere, representing three different land-atmosphere interaction processes.

First, an index I_φ derived by Dirmeyer (2011) quantifies the sensitivity of atmosphere (φ) to land surface (ω). I_φ is a monthly based index calculated by N years of data together. For a specific month (i, i=1~12), this index is the product of two terms: (1) β_φ , the slope of linear regression between monthly anomaly of φ and ω among different years, whose unit is φ divided by ω , and (2) S_ω , the standard deviation of daily ω of the specific month(i) with all among N years (equation 1). Hence, I_φ has the same unit with φ . In addition to β_φ , S_ω is also considered since conditions with high β_φ but low variation of ω are also regarded to have a weak land-atmosphere coupling.

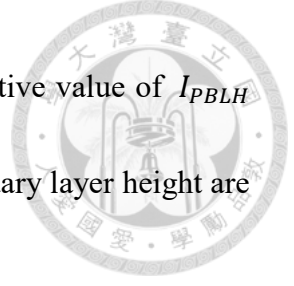
$$I_\varphi = S_\omega \beta_\varphi \quad (1)$$

$$I_{LE} = S_w \beta_{LE} \quad (1. a)$$

$$I_{PBLH} = S_s \beta_{PBLH} \quad (1. b)$$



Two combinations of φ and ω used by Lu et al. (2017) are adopted to represent the influence of land surface characteristics on land-atmosphere exchange fluxes and its subsequent impact on the atmosphere. First, I_{LE} , the coupling between soil moisture of top 10 cm deep (as ω) and surface latent heat flux (as φ), indicates soil moisture anomaly's impact on land-atmosphere exchange fluxes (equation 1.a). S_w refers to the standard deviation of daily soil moisture; β_{LE} refers to the slope between soil moisture and surface latent heat flux. I_{LE} represents the first step of land surface to affect the atmosphere. The sensitivity test of selected soil depth is shown to have similar results as that in Dirmeyer (2011): the global pattern and magnitude of I_{LE} remains similar with different soil depths. When the value of I_{LE} is positive, it indicates that soil moisture influences evapotranspiration since evapotranspiration is under the water-limit condition. On the contrary, the negative value of I_{LE} indicates that soil moisture is affected mostly by evapotranspiration because of the process that more evapotranspiration results in less soil moisture is more significant under the energy-limit condition. Second, I_{PBLH} , the coupling between surface sensible heat flux (as ω) and planetary boundary layer height (as φ), refers to the impact of land-atmosphere exchange fluxes on the boundary layer (equation 1.b). S_s refers to the standard deviation of daily surface sensible heat flux; β_{PBLH} refers to the slope between surface sensible heat flux and planetary boundary layer height. The positive value of I_{PBLH} displays the phenomenon that with higher surface



sensible heat flux, boundary layer height becomes higher. The negative value of I_{PBLH} might relates to the process that surface sensible heat flux and boundary layer height are affected by other factors simultaneously.

I_p is also a monthly based index derived by Zeng et al. (2010), indicating the ratio of the covariance between precipitation anomalies (P') and evapotranspiration anomalies (ET') divided by the variance of precipitation anomalies (equation 2).

$$I_p = \frac{\sum_{y=1}^N P'_y ET'_y}{\sum_{y=1}^N (P'_y)^2} \quad (2)$$

The physical meaning of I_p is the ratio that the variations of precipitation anomalies can be explained by the variations of evapotranspiration anomalies. Zeng et al. (2010) excluded the data where the standard deviation of monthly precipitation is less than 0.2 mm/day since they considered that data with very low standard deviation of precipitation could cause large value of I_p without practical meanings. However, this filter is not used in this research because only few standard deviations of monthly area averaged precipitation are less than 0.2 mm/day among five irrigation areas (Figure 2.4). The positive value of I_p indicates a necessary but not sufficient condition that atmosphere (i.e., precipitation) is positively affected by the land surface (i.e., evapotranspiration). In contrast, the negative value of I_p refers to the situation that atmosphere is negatively affected by the land surface or that the land surface is affected by atmosphere.


In our study, we focus on the process that soil moisture influences the local

precipitation. This process corresponds to the positive value of I_{LE} , I_{PBLH} and the larger absolute value of I_p which represent different parts of land-atmosphere coupling.




2.4 Hydroclimatological characteristics

The Budyko curve displays a concept that the magnitude of evapotranspiration is limited mainly by the availabilities of energy and water. Hence, hydroclimatological characteristics in this study refer to the competing between the available energy and the available water rather than only the consideration of the available water. Under wet (dry) conditions, due to excessive available water (energy), evapotranspiration is mainly limited by the available energy (water), which is also defined as the energy-limit (water-limit) condition. Monthly soil moisture of top 10 cm depth is selected to signify the available water; monthly surface net radiation is selected to denote the available energy. The comparison between soil moisture of top 10 cm depth and precipitation shows that for monthly and seasonal analyses, soil moisture of top 10 cm might be a better representative of the available water because it displays the moisture memory effect of the land. Although deeper soil column might show more significant moisture memory effect, the soil moisture with the depth of top 10 cm is chosen to consist with the soil moisture used to calculate I_{LE} . Surface net radiation is compared with the FAO grass reference evapotranspiration (Allen et al., 1998). Although the FAO grass reference



evapotranspiration consider more variables such as vapor pressure deficit and near surface wind speed, its assumption of fixed grass cover might cause additional bias while comparing between different locations and time, whose surface condition may be diverse. Since monthly surface net radiation and the FAO grass reference evapotranspiration shows similar tendency among five irrigation areas (Figure 2.5), surface net radiation is used to represent the available energy to simplify the analysis. In this study, precipitation is multiplied by the latent heat of evaporation and turned the unit into W/m^2 to compare with net radiation.

To discriminate different hydroclimates, a hydroclimatological scatter chart is used frequently in the analyses. Figure 2.6(a) is an example of hydroclimatological scatter charts using seasonal cycle of America Great Plains (location No 4). Area weighted mean of 15 grids is taken and the climatology of each month from each irrigated area is used to display a datapoint on a hydroclimatological scatter chart. When approaching to the upper left-hand corner of the scatter chart, less soil moisture and more net radiation are shown that indicate the water-limit condition; in contrast, when approaching to lower right-hand corner, more soil moisture and less net radiation refers to the energy-limit condition. In this study, the concept of wet and dry relates to not only the available water but also the available energy. Figure 2.6(b) shows the combined data from five irrigation areas; different symbols represent different places and the shaded color represent different



month. Overall, net radiation is higher during summer and lower during winter. We could recognize that in this study, a specific hydroclimate may consist of data from different places and time. It is shown that the data from Southwest Europe (location No 5) and Middle East (location No 6) during summer, approaching the most to the water-limit condition. On the other hand, the data in North China Plain (location No 3) and Southwest Europe (location No 5) during winter approach the most to the energy-limit condition.

2.5 Budget analyses

2.5.1 Vertically integrated moisture budget

The vertically integrated moisture budget equation is adopted to explore the precipitation changes:

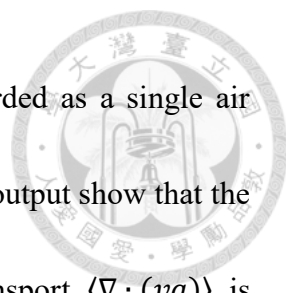
$$\left\langle \frac{\partial q}{\partial t} \right\rangle = ET - P - \langle \nabla \cdot (vq) \rangle \quad (3)$$

where q is specific humidity, ET is evapotranspiration, P is precipitation, v is three-dimensional wind vector. Sign ∇ equals to three-dimensional vector $\frac{\partial}{\partial x}i + \frac{\partial}{\partial y}j + \frac{\partial}{\partial p}k$.

Sign $\langle \rangle$ indicates mass integration from the surface to the top of the troposphere, which is assumed at 100 hPa in this study:

$$\langle X \rangle = \frac{1}{g} \int_{ps}^{pt} X dP \quad (4)$$

Where g is the acceleration of gravity, pt is the pressure of tropopause and ps is the surface pressure.



The atmosphere above each irrigation area (15 grids) is regarded as a single air column to investigate its moisture budget. Calculations from model output show that the numerical error from terrain on vertically integrated lateral water transport $\langle \nabla \cdot (vq) \rangle$ is non-negligible with our irrigation spatial scale. Hence, the water exchanges between atmosphere and land surface (i.e., evapotranspiration and precipitation) are applied to indirectly derive the magnitude of vertically integrated lateral water transport. The changing percentage and seasonal variation of water storage in the atmosphere is less than the change of evapotranspiration minus precipitation after applying the irrigation (Figure 2.7). Consequently, the assumption that the change of evapotranspiration minus precipitation largely contributes to the alteration of vertically integrated lateral water transport is made in this study.

2.5.2 Moist static energy

The moist static energy (MSE) helps the clarification of atmospheric thermodynamic structure:

$$\text{MSE} = C_p T + L_v q + gz \quad (5)$$

where C_p is the heat capacity of air under constant pressure, T is temperature, L_v is the latent heat of vaporization, q is specific humidity, g is the acceleration of gravity and z is height.



Chapter 3 Results

3.1 Relationships between land-atmosphere coupling and local hydroclimates

We investigate the relationship of three land-atmosphere coupling indices (I_{LE} , I_{PBLH} and I_P) and its local hydroclimates both before and after applying the irrigation process in the model in order to explore how the irrigation modulates its relationship.

I_{LE} , the coupling strength between soil moisture and evapotranspiration, has larger magnitude with higher net radiation (green box in Figure 3.1(a)). A strong positive coupling is found over the transition zones between water-limit conditions and energy-limit conditions (Figure 3.1(a)). Through equation 1.a, we can calculate the coupling strength, and we will also analyze the contributions from its partitioning, the slope between soil moisture and evapotranspiration (β_{LE}) and the standard deviation of daily soil moisture (S_w). β_{LE} is usually higher under the water-limit condition (Figure 3.1(b)), indicating that evapotranspiration is more sensitive to soil moisture. β_{LE} decreases while approaching to the energy-limit condition because the major limitation on evapotranspiration changes from the available water to the available energy. S_w is usually larger at the transition zones (Figure 3.1(c)). Therefore, the strong coupling usually happens at the transition condition, with the combined effect of β_{LE} and S_w . The major inhibition of I_{LE} under the water-limit condition is S_w because its corresponding β_{LE} is higher than the magnitude under transition zones and the energy-limit condition.

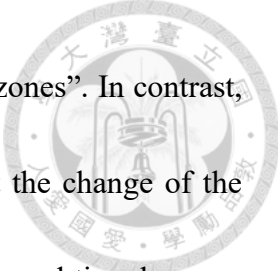


The major inhibition of I_{LE} under the energy-limit condition results from both near-zero β_{LE} and low S_w .

The pattern of I_P , the coupling between evapotranspiration and precipitation, on hydroclimatological scatter chart is similar to the pattern of β_{LE} . I_P is higher when approaching to the water-limit condition (Figure 3.2). This result implies that under the water-limit condition, evapotranspiration anomalies may better explain the variations of precipitation.

Unlike I_{LE} and I_P , I_{PBLH} , the coupling strength between sensible heat flux and boundary layer height, has higher dependence on the net radiation rather than the competing between the available energy and the available water (Figure 3.3). The slope between sensible heat flux and boundary layer height (β_{PBLH}) does not have significant tendency between the water-limit condition and the energy-limit condition. In addition, the standard deviation of daily sensible heat flux (S_s) contributes remarkably to the pattern of I_{PBLH} that it is higher under strong net radiation. The positive relationship between I_{PBLH} and net radiation demonstrates that with more net radiation, which often happens in summer, surface fluxes could have more intense impact on the development of the boundary layer. Strong turbulence mixing resulting from surface heating under high net radiation condition might be a possible reason.

In sum, I_{LE} and I_P have a stronger relationship with the local hydroclimatic




conditions, although I_p shows no feature of “hot spots at transition zones”. In contrast, I_{PBLH} depends more on net radiations. These diversities imply that the change of the coupling indices after irrigation may be different at the same location and time because of the different controlling factors. In fact, results from coupled simulations indeed show such diverse responses (Figure 3.9 (c)~(e)).

3.2 Irrigation’s impact on land-atmosphere coupling in offline simulations

Irrigation directly affects the soil moisture, evapotranspiration, and net radiation of the surface. In offline simulations, because of fixed atmospheric conditions, the change in net radiation is relatively smaller than the changes in soil moisture and evapotranspiration (Figure 3.4). This phenomenon is especially apparent with more irrigation and more excessive available energy (i.e., approaching to the water-limit condition). The slight increase in net radiation results from two aspects: (1) the decrease in albedo causing more absorbed solar radiation and (2) the surface cooling causing less outgoing long wave radiation. Consequently, the change in the available energy is neglected and the available water’s impact on land-atmosphere coupling will be the focus in offline simulations.

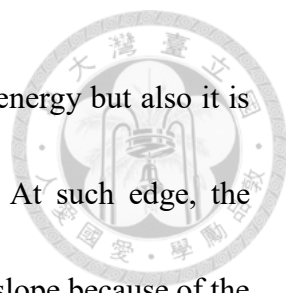
There is a strong tendency on irrigation’s impact on soil moisture and evapotranspiration among different hydroclimates. Because irrigated water might be



different among different places/time and result in distinct magnitude of response, added water is used to normalize the response of evapotranspiration and soil moisture. The proportion of irrigation water which turns into evapotranspiration is higher when approaching to water-limit conditions because of more excessive available energy (Figure 3.5). This also results in stronger surface cooling at the same time. Irrigated water tends to remain more in soil layers under semi-arid conditions (Figure 3.6). Under extreme dry conditions, a higher ratio of irrigated water turns into evapotranspiration and less remains in the soil. In comparison, a higher ratio of irrigated water turns into runoff under extreme wet conditions due to the saturation of soil moisture. Furthermore, the results are similar among three offline scenarios.

We only analyze the changes in I_{LE} in offline simulations since I_{PBLH} and I_P do not change under the fixed atmosphere conditions. To exclude the factor that the irrigated water may have distinct magnitude among different location and time, the change of soil moisture is used to normalize the change of coupling index. Figure 3.7.1 shows that considering changes of the available water only, I_{LE} has significant decline at the transition zones, slightly increase under extreme dry conditions and less alteration while approaching the energy-limit condition.

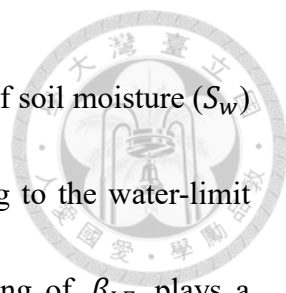
The slope between soil moisture and evapotranspiration (β_{LE}) generally decreases with more available water, especially at the transition zones (Figure 3.7.2). The transition



zone is a state that its mainly controlling factor is still the available energy but also it is at the edge of water-limit conditions and energy-limit conditions. At such edge, the increase of the available water might cause significant decline of the slope because of the transform from water-limit conditions to energy-limit conditions.

On the other hand, the standard deviation of daily soil moisture (S_w) increases (decreases) more under water-limit (energy-limit) conditions (Figure 3.7.3). The higher proportion of irrigation water which turns into evapotranspiration under water-limit conditions might be the cause of the increased S_w . The processes of adding water and the subsequent evapotranspiration make the variation of daily soil moisture larger. The decrease of S_w under energy-limit conditions might be due to the saturation of soil moisture. Figure 3.8 shows the probability density function of daily soil moisture under original extreme wet conditions, corresponding to the orange circle in Figure 3.7.3 (a). The whole probability density function shifts to the right except the right-end part. That is because with the originally higher soil moisture, the water content in the soil reaches the upper limit more easily and narrows the variability of daily soil moisture.

In summary, because of fixed atmospheric boundary conditions in offline simulations, the diversity of irrigation's impact could be explained well by hydroclimatological characteristics. The significant decrease of I_{LE} at transition zones is largely contributed by the decline of the slope between soil moisture and



evapotranspiration (β_{LE}) since its corresponding standard deviation of soil moisture (S_w) only slightly changes. The slight increase of I_{LE} when approaching to the water-limit condition mainly results from the increase of S_w , and the declining of β_{LE} plays a compensating role to reduce the effects of S_w . Few outliers might result from the slight change of the net radiation. In addition, three irrigation scenarios show similar results.

3.3 Irrigation's impact on land-atmosphere coupling in coupled simulations

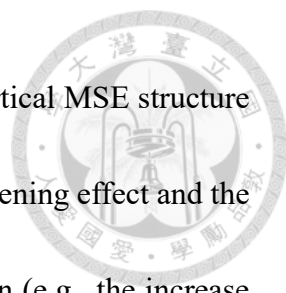
Different from offline land surface model simulations, the atmospheric conditions in coupled land-atmosphere simulations also change in response to surface irrigation. The change of precipitation caused by irrigation (Figure 3.9 (a)) could further result in the alteration of the available water on the surface through the land-atmosphere feedbacks. For example, in some cases, the decline of precipitation might cancel out the purpose of irrigation and cause the decrease of the available water, which is an important water recycling issue (Harding and Snyder, 2012b; Ho, 2017; Lo and Famiglietti, 2013; Wey et al., 2015). The change of cloud and air temperature also affects the surface net radiation (Figure 3.9 (b)). Hence, the shift of land-atmosphere coupling may be different from offline simulations even with the same irrigation magnitude. Also, the alterations in the three coupling indices are not consistent in sign at the same month and location (Figure 3.9 (c)~(e)). The increase of I_{LE} does not guarantee to the increase of I_P or I_{PBLH} in

corresponding time and location. This inconsistency might result from different dependence of each index on the hydroclimate.



The static stability of the atmosphere is affected by the moistening effect and the cooling effect of irrigation. Analysis of the moist static energy at near surface atmosphere in JJA and DJF shows that more added irrigation water (via the comparison between JJA and DJF) under drier conditions (via the comparison of different locations in the same season) seems to result in more significant moistening effect and cooling effect (Figure 3.10). In addition, the magnitude of moistening effect is often larger than the cooling effect, leading to a higher moist static energy and instability of the near surface atmosphere. This tendency shows that while approaching to the water-limit condition, irrigation might more greatly change land-atmosphere coupling because of more significant direct changes of surface fluxes. In contrast, while approaching to the energy-limit condition, excessive available water does not lead to great change of surface fluxes and the subsequent shift of land-atmosphere coupling. Simulated results in the North China Plain (location No 3) during JJA might be an exception because its significant increase of near surface water vapor might result from low-level water vapor convergence rather than from increased evapotranspiration (discussed later with Figure 3.12 ~ 3.18).

However, the higher moist static energy at the low-level atmosphere is not directly linked to more convection because its instability is released only after the saturation of

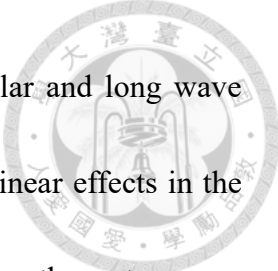


water vapor in the atmosphere (Lu et al., 2017). Also, the shift of vertical MSE structure (Figure 3.11 as an example) shows not only the signals of local moistening effect and the cooling effect but also the signals of changed atmospheric circulation (e.g., the increase of temperature and the decrease of water vapor in the lower atmosphere). Hence, in addition to the response of thermodynamic processes, the attribution of dynamic response (e.g., large scale atmospheric circulation) induced by irrigation should also be considered.

The atmospheric column water budget analysis in control simulation is used to clarify the proportion of local and non-local water vapor sources for precipitation (Figure 3.12). Besides the hydroclimate, the different of water vapor sources might also cause the diversity of atmospheric response to the irrigation. Negative values of evapotranspiration (upward positive) minus precipitation (downward positive) significantly appear in North India (location No 1) and North China Plain (location No 3) during the summer (orange circle in Figure 3.12). In such cases, even with the assumption that 100% of evapotranspiration becomes local precipitation, the local water vapor source (i.e., evapotranspiration) could not provide enough water vapor for forming the precipitation. Thus, the notable larger precipitation indicates strong water vapor convergence and large proportion of non-local water vapor sources for precipitation, which is possibly due to the monsoon circulation in both India and China. In contrast, due to near-zero evapotranspiration minus precipitation in other places and time, we can only state that the

magnitude of evapotranspiration is similar to that of precipitation. However, there is less confidence in the proportion of local and non-local water vapor sources for precipitation.

In general, evapotranspiration increases after irrigation (Figure 3.13). But the change in precipitation is more diverse. In most cases the change in local precipitation is less than that in evapotranspiration. The cooling effect of irrigation causes the local subsidence (Figure 3.14) and the low-level water vapor divergence. North China Plain is the most obvious exception during the early summer (blue circle in Figure 3.13) accompanying with ascending anomaly (Figure 3.15). Since North China Plain is the place where approaches the most to the energy-limit condition due to the monsoon in the summer, the increase of evapotranspiration and surface cooling is small (Figure 3.16 as an example and data during summer shows the similar pattern). In North China Plain, less increase of irrigation-induced evapotranspiration due to the approaching of the energy-limit condition might inhibit the local direct atmospheric response caused by irrigation. Contrarily, this property might more significantly reflects the non-local signal of changing large scale circulation due to slightly different land surface properties. In North China Plain during the early summer, the affected regions of changed water vapor divergence (Figure 3.17) and precipitation (Figure 3.18) are larger than the irrigation area. Consequently, this great increase of precipitation could be the result of changing large scale circulation. In addition to the available water, the available energy is also affected



by the atmospheric circulation through changes in the incoming solar and long wave radiation compared to offline simulations. Moreover, there are non-linear effects in the atmospheric process among different irrigation scenarios. For instance, the water vapor convergence anomaly in China is larger in F_self scenario compared to that in F_max scenario, although the added irrigation water is less in the F_self scenario.

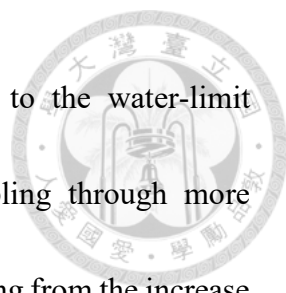
Although the conversion of the available energy and water resulting from both irrigation and its subsequent shifts of atmospheric circulation could not be explained perfectly only by their original local hydroclimatology characteristics, the land-atmosphere coupling before and after irrigation shows similar characteristic with the hydroclimate (Figure 3.19~3.21), which is described in section 3.1. It indicates that with identical change in the available water and/or energy, the alteration of land-atmosphere coupling could be dissimilar depending on original hydroclimate characteristics.

Chapter 4 Summary, discussion and future work



4.1 Summary

Three land-atmosphere coupling indices adopted in this study have different dependence on the hydroclimate (Figure 4.1). I_{LE} and I_P clearly relate to hydroclimatological characteristics (i.e., competing effect between the available energy and water), while I_{PBLH} depends more on the surface net radiation. In offline land surface model simulations, when there is more significant increase in the available water than the available energy, irrigation's impact on I_{LE} could be explained perfectly by the hydroclimate. At transition zones, I_{LE} decreases dramatically due to the intensive decrease of β_{LE} (Figure 4.1(a)). However, I_{LE} increases slightly while approaching to the water-limit condition primarily because of the higher S_w . While approaching to the energy-limit condition, I_{LE} changes less mainly because of constant β_{LE} . In coupled land-atmosphere simulations, with complex nonlinear interaction with the atmosphere, the alteration of land-atmosphere coupling shows larger diversity. The diversity could not be clarified only by the hydroclimate; the mean state of atmospheric circulation should also be considered. As the aspect of static stability, more added water approaching to the water-limit condition seems to result in more significant surface moistening effect and cooling effect because of greater increase in the latent heat flux (Figure 4.2). At the same time, the moistening effect is larger than the cooling effect and potentially leading to an



unstable atmosphere. This result implies that while approaching to the water-limit condition, irrigation might affect more on land-atmosphere coupling through more significant direct changes of surface fluxes. But this instability resulting from the increase moisture does not guarantee more convections or anomalous upward motions. Generally, irrigation cools the surface due to the increase in the latent heat flux, causing subsidence and low-level water vapor divergence in our simulations. A noticeable exception appears in North China Plain during early summer with stronger water vapor convergence. According to Figure 2.6(b), simulations in North China Plain approach the most to the energy-limit condition during summer. Hence, this exception is possibly due to weaker surface cooling while approaching to the energy-limit condition (Figure 4.2(c)) and its unique characteristics of atmospheric circulation (i.e., East Asian monsoon). Because of irrigation's subsequent impact on the atmosphere, the shift of the available energy and water (e.g., cloud responses and precipitation's feedback to the surface accessible water) is rather difficult to expect only by the local hydroclimate characteristics. Despite these complex reactions, both strength of three land-atmosphere coupling indices before and after irrigation still follow their original tendency toward the available water and energy (Figure 4.1). The tendency of land-atmosphere coupling toward the hydroclimate indicates that with the same magnitude of the available water (energy) difference, the alteration of land-atmosphere coupling (or a coupling index) could be dissimilar under

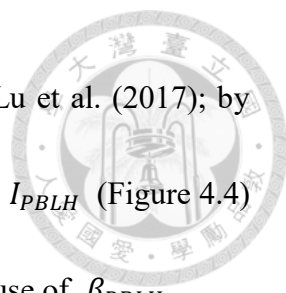
the water-limit condition, the transition zones, or the energy-limit condition.



4.2 Discussion

The dependence of I_{LE} on the local hydroclimate found in this study is consistent with Koster et al. (2004) and Dirmeyer (2011) that stronger land-atmosphere coupling mostly happens in the summer hemisphere and “hot spots at transition zones” are more significant. The weak coupling of I_{LE} approaching to the water-limit condition mainly results from low S_w in our study. This feature is similar to the explanation of Koster et al. (2004) that evapotranspiration at extreme dry conditions is not large enough to affect the local atmospheric stability even with the strong relationship between soil moisture and evapotranspiration.


Mostly irrigation-induced surface cooling causes local subsidence in our coupled simulations, corresponding to the results of Im et al. (2014) that large-scale irrigation in the West African results in the suppress of moist convection. In comparisons with the coupled simulations (F_self) in summer America Great Plains (location No 4) (Figure 4.3) to the study of Lu et al. (2017), I_{LE} from July to September in our simulations declines mainly due to the decrease of β_{LE} . Because oppositely, the corresponding S_w increases except for July in our study, while their results show the decline of I_{LE} , β_{LE} and S_w . Furthermore, their main contribution of decreased I_{LE} also comes from β_{LE} . The



response of I_{LE} and β_{LE} are similar in our research and study of Lu et al. (2017); by contrast, the responses of S_w are different. Besides, the response of I_{PBLH} (Figure 4.4) is also similar with Lu et al. (2017) that I_{PBLH} declines mostly because of β_{PBLH} .

The diverse compared to Lu et al. (2017) might come from the different models and irrigation simulation strategy. The CESM, an atmospheric general circulation model, is used in our study while Lu et al. (2017) used WRF3.3–CLM4crop, which is a regional climate model including the process of dynamic crop growth. Irrigation is only added to 15 grids area in this study, while they irrigated the whole America with realistic data. In our study, three coupling indices may respond dissimilarly under the same time and the same location. This result is distinct from Lu et al. (2017) that both I_{LE} and I_{PBLH} are declined after irrigation at America Great Plains. The results from section 3.1 display a possible reason that the dependence of three indices on the hydroclimate is not exactly the same.

Increases in precipitation after irrigation in North China Plain in the summer was also simulated by Puma and Cook (2010) as they irrigated globally by historical data from 1980 to 2000 in Goddard Institute for Space Studies (GISS) ModelE. Xie et al. (2017) also indicated increases in precipitation in this region by a modified regional climate model with the consideration of human water withdrawal and use. However, both studies did not indicate the possible mechanisms of increased precipitation. We think that the




increase of precipitation in North China Plain during the summer might result from the change of large scale circulation in our study, but the mechanisms of this result still remain unclear and need further investigations. Several studies (Lo and Famiglietti, 2013; Lu et al., 2017; Puma and Cook, 2010) displayed the phenomenon that irrigated water mostly formed precipitation in downwind regions rather than irrigation area, corresponding to our finding of water vapor divergence in most of the irrigation area except for North China Plain.

4.3 Future work and application

4.3.1 The limitation of experiment design

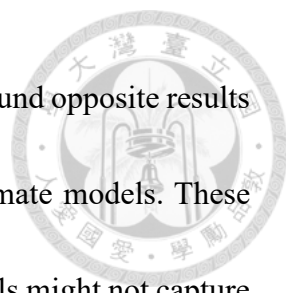
The sensitivity tests for the spatial scale of irrigation area should be investigated further because the size of land used changes may impact its climate response, which is referred in section 2.2 (Chagnon, 2005; Ho, 2017; Khanna et al., 2017; Lawrence and Vandecar, 2014). Different shape of irrigation area should be tested since the shape of the irrigation area might also affect the result and the realistic shape of irrigation field could be more complex than rectangle, which is used in our study. The strategy of adding water could be more realistic by adding water during the day time rather than each time step. Also, despite three irrigation scenarios used in this study, more detailed sensitivity test of added water amount might contribute to a clearer explanation of non-linear precipitation



response between F_{self} and F_{max} . The unrealistic irrigation management of “maximum/minimum of irrigation intensity seasonal cycle among five irrigation areas” may overestimate or underestimate the result and require further concern. For example, Sacks et al. (2009) found that with extreme irrigation which is over 100 times of actual magnitude, the response showed larger magnitude although with similar changing tendency.

The sensitivity test of the depth of the soil moisture which represents the available water should also be investigated because usually deeper soil column displays stronger memory effect of moisture. The reaction of lifting condensation level (LCL) could be further analyzed to explain why the irrigation-induced moist static instability does not result in more convection. This was done by Lu et al. (2017) for the case of America irrigation through regional model and showed a larger reduction of the planetary boundary layer height than LCL, inhibiting the transport of water vapor to a higher level. The irrigation-induced increase of water vapor at near surface is not transported to LCL and does not condense. Consequently, this excessive water vapor does not release their latent heat to the atmosphere, which leads to an unchanged precipitation.

The results (e.g., the response of LCL) might be model dependent since irrigation's impact might be distinct with different model resolution, domain and boundary layer and convection parameterizations (e.g., Hirsch et al., 2015). For instance, Taylor et al. (2012)

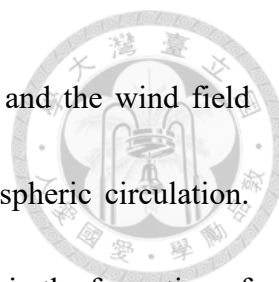


examined the coupling between soil moisture and precipitation and found opposite results between observation and six state-of-the-art global weather and climate models. These inconsistent results indicated that coarse grid resolution in such models might not capture the mesoscale structure, which is crucial for convection triggering. Hence, simulations with different grid size should be investigated. In addition, the adoption of cloud resolving model might contribute to the clarification of diverse results due to boundary layer and convection parameterizations (Cheng and Cotton, 2004).

Since ocean is prescribed by climatological sea surface temperature in coupled land-atmosphere simulations, the interaction between ocean and land/atmosphere is excluded in our study. However, the same land-used change process under different sea surface temperature pattern might show diverse result through the interaction with the ocean dynamics (Chen, 2017). Hence different prescribed sea surface temperature patterns (e.g., ENSO) and fully couple ocean experiment are worth doing to examine more realistic response of land-atmosphere coupling toward irrigation.

4.3.2 Other factors that result in the diversity of LAC responses

The mean state of atmospheric circulation should be further considered because from our conclusion, the mean state of atmospheric circulation is also an important factor which influences the atmospheric response of irrigation, such as the alteration of cloud



cover (Sacks et al., 2009). The dominative synoptic environments and the wind field could be the aspect of considering the different of the mean atmospheric circulation.

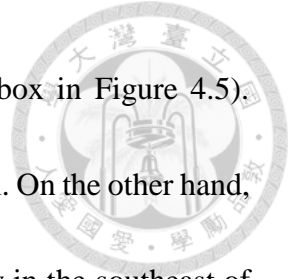
Several research stated that synoptic environments play a primal role in the formation of precipitation (Barnston and Schickedanz, 1984; Harding and Snyder, 2012a; Zhou et al., 2016). Ho (2017) revealed that different atmospheric vorticity corresponded to distinct response of irrigation, displaying the non-negligible influence of prevailing wind fiend.

The soil moisture spatial gradient between irrigation area and its surrounding could be further analyzed because such moisture gradient might also influence the response of the atmospheric circulation through large scale effects (Hsu et al., 2017). The consideration of soil moisture spatial gradient might contribute to the explanation of atmospheric response in our simulations.

4.3.3 Application

In summary, the results of this study show that the potential response of LAC after irrigation might be different based on the original local hydroclimatological characteristics although the hydroclimate could not explain all the response perfectly. The conclusion could be applied to the shift of LAC under ENSO and climate changes because the alteration of precipitation and/or energy may have similar effects as irrigation. For example, during strong El Niño events in 1997 and 1998, precipitation decreased and

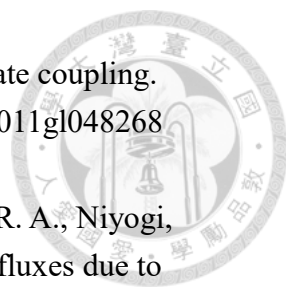
surface net radiation increased obviously in central Africa (green box in Figure 4.5). Hence the hydroclimate there shifted toward the water-limit condition. On the other hand, precipitation increased and surface net radiation decreased obviously in the southeast of South America (purple box in Figure 4.5), shifting the hydroclimate toward the energy-limit condition. How the LAC might shift is an important topic to explore.





References

- Allen, R. G., Pereira, L. S., Raes, D., & Smith, M. (1998). Crop evapotranspiration-Guidelines for computing crop water requirements-FAO Irrigation and drainage paper 56. Fao, Rome, 300(9), D05109.
- Alter, R. E., Douglas, H. C., Winter, J. M., & Eltahir, E. A. (2018). Twentieth century regional climate change during the summer in the central United States attributed to agricultural intensification. *Geophysical Research Letters*, *45*(3), 1586-1594.
- Badger, A. M., & Dirmeyer, P. A. (2015). Climate response to Amazon forest replacement by heterogeneous crop cover. *Hydrology and Earth System Sciences*, *19*(11), 4547-4557. doi:10.5194/hess-19-4547-2015
- Barnston, A. G., & Schickedanz, P. T. (1984). The effect of irrigation on warm season precipitation in the southern Great Plains. *Journal of Climate and Applied Meteorology*, *23*(6), 865-888.
- Budyko, M. I. (1961). The Heat Balance of the Earth's Surface. *Soviet Geography*, *2*(4), 3-13. doi:10.1080/00385417.1961.10770761
- Chagnon, F. J. F. (2005). Contemporary climate change in the Amazon. *Geophysical Research Letters*, *32*(13). doi:10.1029/2005gl022722
- Chen, C.-C. (2017). The Relation between Climate and Deforestation in the Maritime Continent.
- Cheng, W. Y., & Cotton, W. R. (2004). Sensitivity of a cloud-resolving simulation of the genesis of a mesoscale convective system to horizontal heterogeneities in soil moisture initialization. *Journal of Hydrometeorology*, *5*(5), 934-958.
- DeFries, R. S., Foley, J. A., & Asner, G. P. (2004). Land-use choices: balancing human needs and ecosystem function. *Frontiers in Ecology and the Environment*, *2*(5), 249-257.
- Diffenbaugh, N. S. (2009). Influence of modern land cover on the climate of the United States. *Climate Dynamics*, *33*(7-8), 945.


- 
- Dirmeyer, P. A. (2011). The terrestrial segment of soil moisture-climate coupling. *Geophysical Research Letters*, 38(16), n/a-n/a. doi:10.1029/2011gl048268
- Douglas, E. M., Niyogi, D., Frohking, S., Yeluripati, J. B., Pielke Sr, R. A., Niyogi, N., . . . Mohanty, U. (2006). Changes in moisture and energy fluxes due to agricultural land use and irrigation in the Indian Monsoon Belt. *Geophysical Research Letters*, 33(14).
- Findell, K. L., & Eltahir, E. A. B. (1997). An analysis of the soil moisture-rainfall feedback, based on direct observations from Illinois. *Water Resources Research*, 33(4).
- Green, R. E., Cornell, S. J., Scharlemann, J. P., & Balmford, A. (2005). Farming and the fate of wild nature. *SCIENCE*, 307(5709), 550-555.
- Harding, K. J., & Snyder, P. K. (2012a). Modeling the Atmospheric Response to Irrigation in the Great Plains. Part I: General Impacts on Precipitation and the Energy Budget. *Journal of Hydrometeorology*, 13(6), 1667-1686. doi:10.1175/jhm-d-11-098.1
- Harding, K. J., & Snyder, P. K. (2012b). Modeling the Atmospheric Response to Irrigation in the Great Plains. Part II: The Precipitation of Irrigated Water and Changes in Precipitation Recycling. *Journal of Hydrometeorology*, 13(6), 1687-1703. doi:10.1175/jhm-d-11-099.1
- Hirsch, A. L., Pitman, A., Kala, J., Lorenz, R., & Donat, M. (2015). Modulation of land-use change impacts on temperature extremes via land-atmosphere coupling over Australia. *Earth Interactions*, 19(12), 1-24.
- Ho, A.-C. (2017). Responses of Land-Atmosphere Interactions to the Change in Irrigation Area Size. doi:10.6342/NTU201701733
- Hsu, H., Lo, M. H., Guillod, B. P., Miralles, D. G., & Kumar, S. (2017). Relation between precipitation location and antecedent/subsequent soil moisture spatial patterns. *Journal of Geophysical Research: Atmospheres*.
- Im, E.-S., Marcella, M. P., & Eltahir, E. A. (2014). Impact of potential large-scale irrigation on the West African monsoon and its dependence on location of irrigated area. *Journal of Climate*, 27(3), 994-1009.



- Jung, M., Reichstein, M., Ciais, P., Seneviratne, S. I., Sheffield, J., Goulden, M. L., . . . Zhang, K. (2010). Recent decline in the global land evapotranspiration trend due to limited moisture supply. *Nature*, *467*(7318), 951-954. doi:10.1038/nature09396
- Khanna, J., Medvigy, D., Fueglistaler, S., & Walko, R. (2017). Regional dry-season climate changes due to three decades of Amazonian deforestation. *Nature Climate Change*, *7*(3), 200-204. doi:10.1038/nclimate3226
- Koster, R. D., Dirmeyer, P. A., Guo, Z., Bonan, G., Chan, E., Cox, P., . . . Yamada, T. (2004). Regions of Strong Coupling Between Soil Moisture and Precipitation. *SCIENCE*, *305*, 3. doi:10.1126/science.1100217
- Lawrence, D., & Vandecar, K. (2014). Effects of tropical deforestation on climate and agriculture. *Nature Climate Change*, *5*(1), 27-36. doi:10.1038/nclimate2430
- Lee, E., Chase, T. N., Rajagopalan, B., Barry, R. G., Biggs, T. W., & Lawrence, P. J. (2009). Effects of irrigation and vegetation activity on early Indian summer monsoon variability. *International Journal of Climatology*, *29*(4), 573-581.
- Lo, M. H., & Famiglietti, J. S. (2013). Irrigation in California's Central Valley strengthens the southwestern US water cycle. *Geophysical Research Letters*, *40*(2), 301-306.
- Lo, M. H., Wu, C. M., Ma, H. Y., & Famiglietti, J. S. (2013). The response of coastal stratocumulus clouds to agricultural irrigation in California. *Journal of Geophysical Research: Atmospheres*, *118*(12), 6044-6051.
- Lu, Y., Harding, K., & Kueppers, L. (2017). Irrigation Effects on Land–Atmosphere Coupling Strength in the United States. *Journal of Climate*, *30*(10), 3671-3685.
- Mahmood, R., Pielke, R. A., Hubbard, K. G., Niyogi, D., Dirmeyer, P. A., McAlpine, C., . . . Beltrán-Przekurat, A. (2014). Land cover changes and their biogeophysical effects on climate. *International Journal of Climatology*, *34*(4), 929-953.
- Matson, P. A., Parton, W. J., Power, A., & Swift, M. (1997). Agricultural intensification and ecosystem properties. *SCIENCE*, *277*(5325), 504-509.



- McDermid, S., Mearns, L., & Ruane, A. (2017). Representing agriculture in Earth System Models: Approaches and priorities for development. *Journal of Advances in Modeling Earth Systems*, 9(5), 2230-2265.
- Mei, R., & Wang, G. (2011). Impact of Sea Surface Temperature and Soil Moisture on Summer Precipitation in the United States Based on Observational Data. *Journal of Hydrometeorology*, 12(5), 1086-1099. doi:10.1175/2011jhm1312.1
- Miralles, D. G., van den Berg, M. J., Gash, J. H., Parinussa, R. M., de Jeu, R. A. M., Beck, H. E., . . . Johannes Dolman, A. (2013). El Niño–La Niña cycle and recent trends in continental evaporation. *Nature Climate Change*, 4(2), 122-126. doi:10.1038/nclimate2068
- Pielke Sr, R. A., Pitman, A., Niyogi, D., Mahmood, R., McAlpine, C., Hossain, F., . . . Fall, S. (2011). Land use/land cover changes and climate: modeling analysis and observational evidence. *Wiley Interdisciplinary Reviews: Climate Change*, 2(6), 828-850.
- Puma, M. J., & Cook, B. I. (2010). Effects of irrigation on global climate during the 20th century. *Journal of Geophysical Research*, 115(D16). doi:10.1029/2010jd014122
- Quesada, B., Arneth, A., & Noblet-Ducoudré, N. (2017). Atmospheric, radiative, and hydrologic effects of future land use and land cover changes: A global and multimodel climate picture. *Journal of Geophysical Research: Atmospheres*, 122(10), 5113-5131.
- Ramankutty, N., Evan, A. T., Monfreda, C., & Foley, J. A. (2008). Farming the planet: 1. Geographic distribution of global agricultural lands in the year 2000. *Global biogeochemical cycles*, 22(1).
- Sacks, W. J., Cook, B. I., Buening, N., Levis, S., & Helkowski, J. H. (2009). Effects of global irrigation on the near-surface climate. *Climate Dynamics*, 33(2-3), 159-175.
- Taylor, C. M., de Jeu, R. A., Guichard, F., Harris, P. P., & Dorigo, W. A. (2012). Afternoon rain more likely over drier soils. *Nature*, 489(7416), 423.

- 
- Tuttle, S., & Salvucci, G. (2016). Empirical evidence of contrasting soil moisture–precipitation feedbacks across the United States. *SCIENCE*, 352(6287). doi:0.1126/science.aaa7185
- Wada, Y., & Bierkens, M. F. (2014). Sustainability of global water use: past reconstruction and future projections. *Environmental Research Letters*, 9(10), 104003.
- Wey, H. W., Lo, M. H., Lee, S. Y., Yu, J. Y., & Hsu, H. H. (2015). Potential impacts of wintertime soil moisture anomalies from agricultural irrigation at low latitudes on regional and global climates. *Geophysical Research Letters*, 42(20), 8605-8614.
- Xie, Z.-H., Zeng, Y.-J., Xia, J., Qin, P.-H., Jia, B.-H., Zou, J., & Liu, S. (2017). Coupled modeling of land hydrology–regional climate including human carbon emission and water exploitation. *Advances in Climate Change Research*, 8(2), 68-79.
- Zeng, X., Barlage, M., Castro, C., & Fling, K. (2010). Comparison of Land–Precipitation Coupling Strength Using Observations and Models. *Journal of Hydrometeorology*, 11(4), 979-994. doi:10.1175/2010jhm1226.1
- Zhou, Y., Wu, D., K.-M. Lau, W., & Tao, W.-K. (2016). Scale Dependence of Land–Atmosphere Interactions in Wet and Dry Regions as Simulated with NU-WRF over the Southwestern and South-Central United States. *Journal of Hydrometeorology*, 17(8), 2121-2136.



Figures

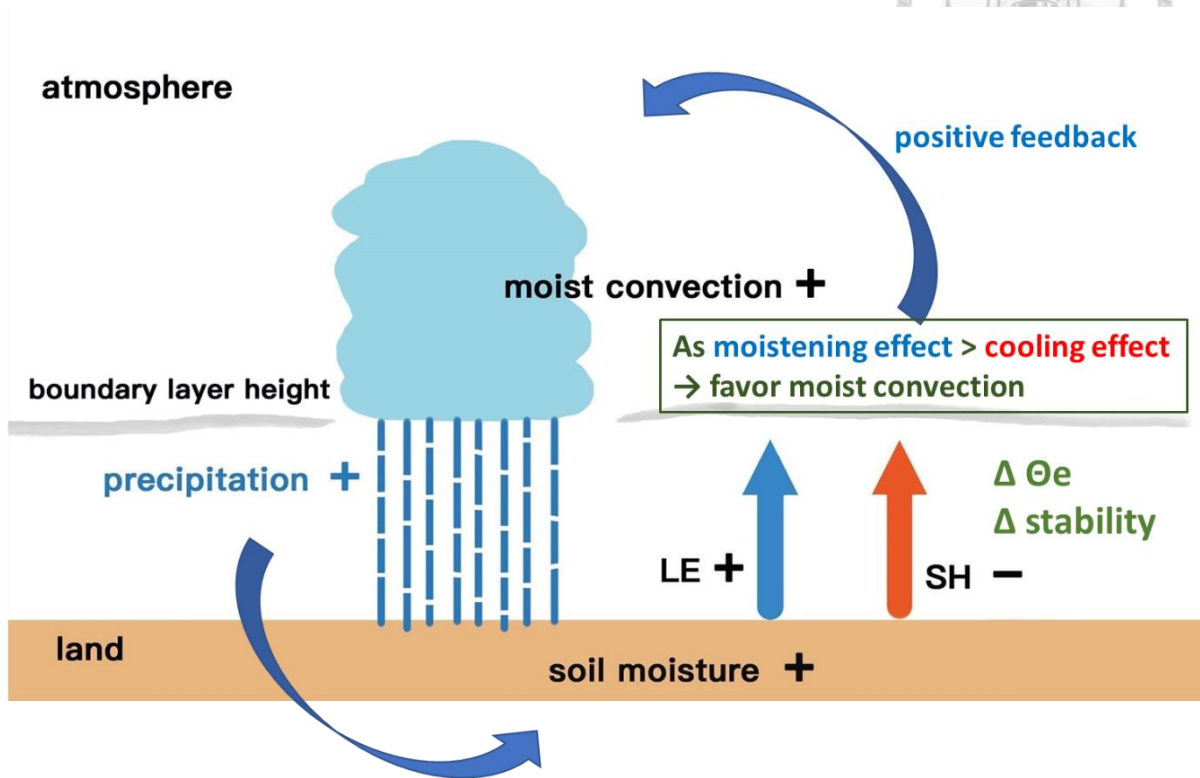


Figure 1.1 The illustration of the land-atmosphere coupling (positive coupling as an example) adopted in this study. LE: surface latent heat flux; SH: surface sensible heat flux; θ_e : equivalent potential temperature; Δx : the change of x.

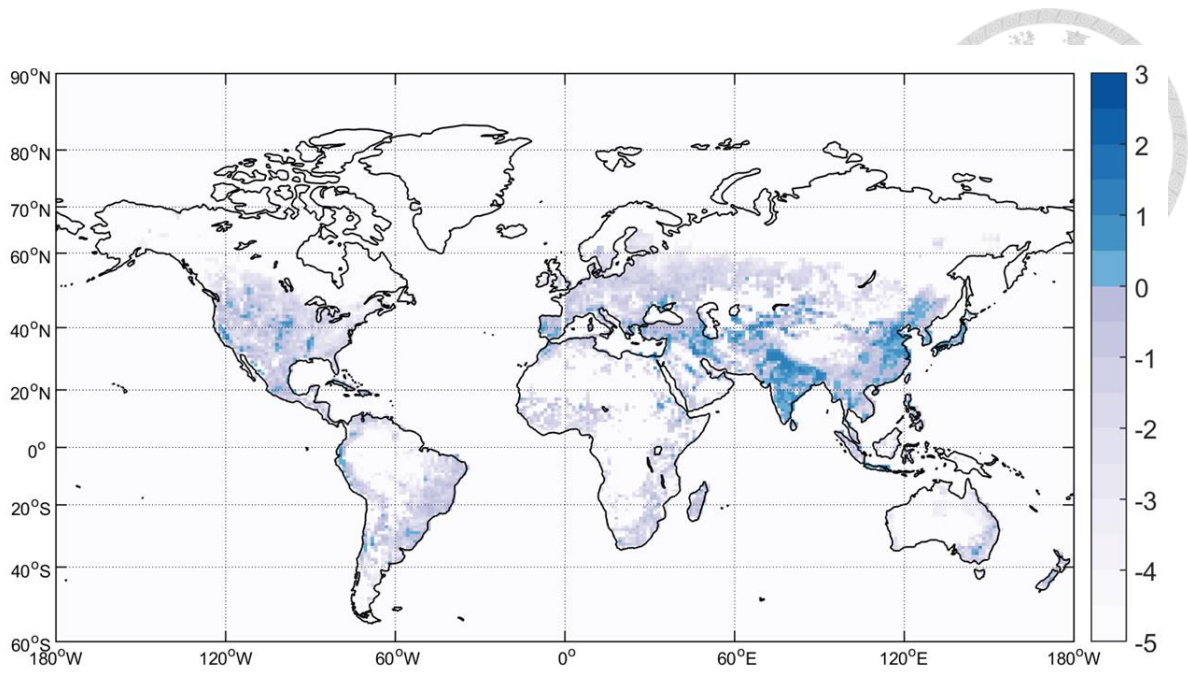


Figure 1.2 Global irrigation map of 2001~2010 average according to Wada and Bierkens (2014). Irrigation unit: \log_{10} (mm/month).

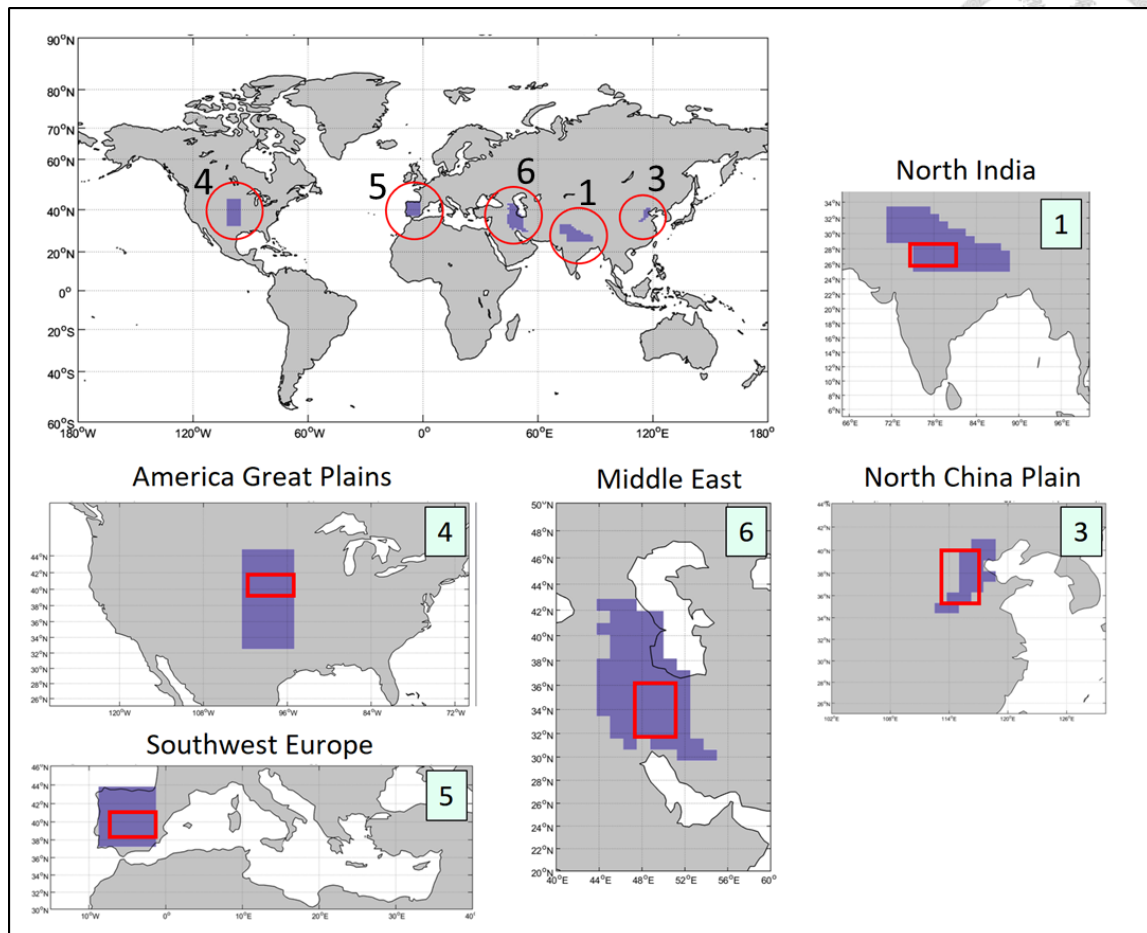


Figure 2.1 Five intense irrigation areas targeted from a monthly irrigation intensity data set derived by Wada and Bierkens (2014): North India (location No 1), North China Plain (location No 3), America Great Plains (location No 4), Southwest Europe (location No 5) and Middle East (location No 6). Purple areas are the original region of significant agricultural irrigation; Red boxes are simulated irrigation region in the model.

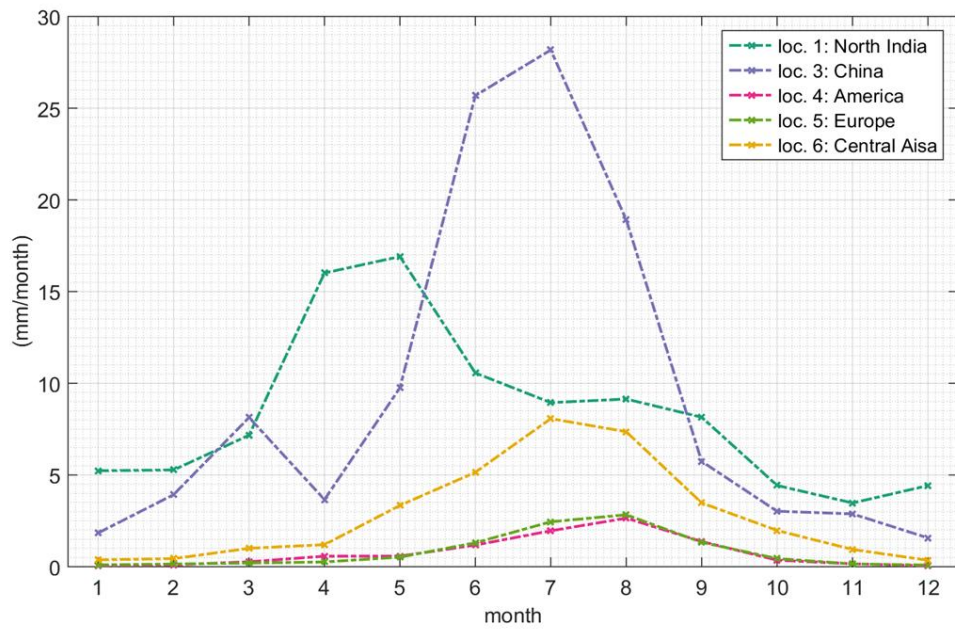


Figure 2.2 Climatology of monthly irrigation intensity of five selected locations between 2001 to 2010.

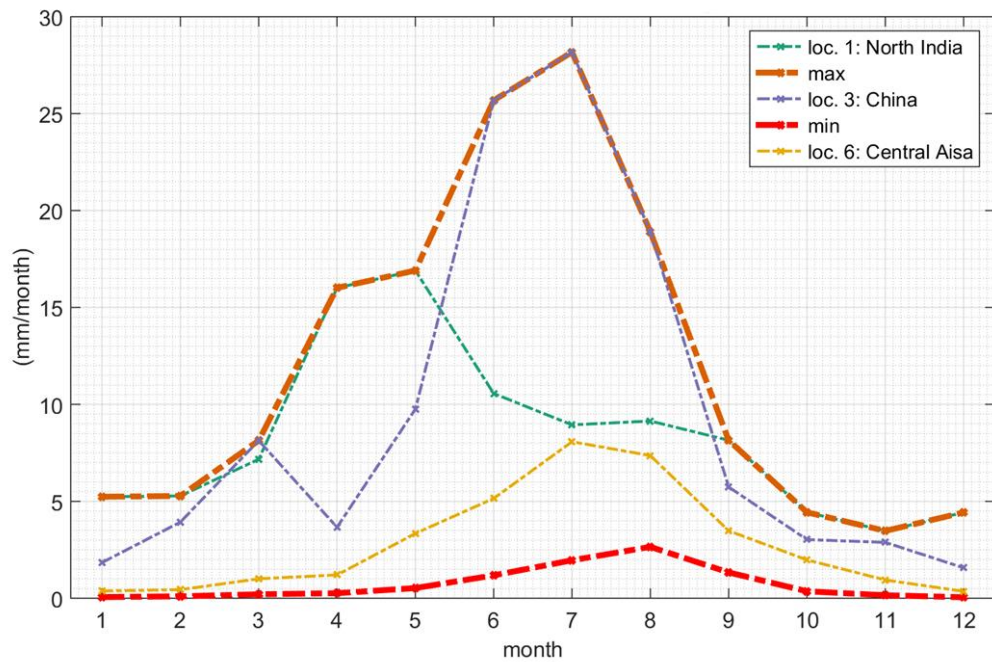


Figure 2.3 Climatology of monthly irrigation intensity of three selected locations between 2001 to 2010. Curves of Central Asia (location No 4) and Europe(location No 5) are combined into “minimum of irrigation intensity seasonal cycle”. Also, “maximum of irrigation intensity seasonal cycle” is defined.

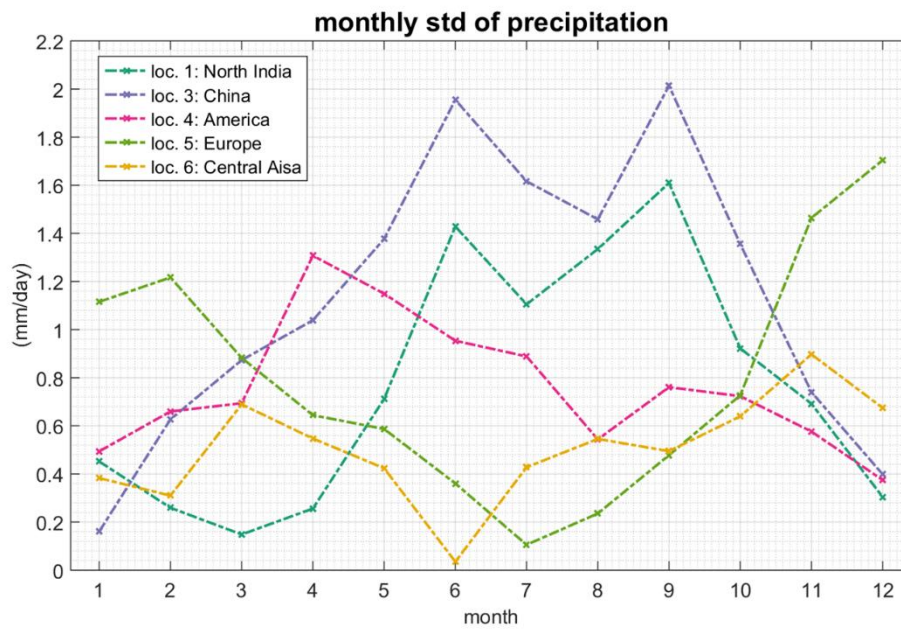
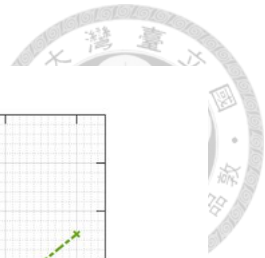


Figure 2.4 Standard deviation of monthly area averaged precipitation among 25 years in F_ctl.

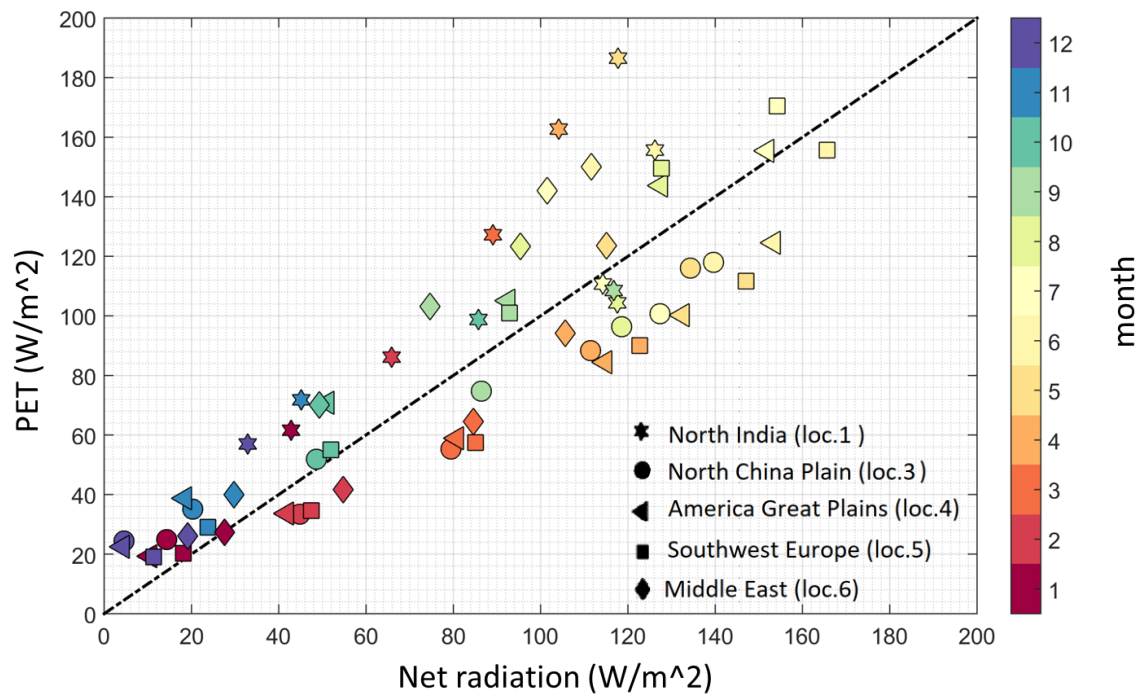


Figure 2.5 Scatter plot of surface net radiation and the FAO grass reference evapotranspiration (PET) in F_ctl. The climatological monthly data from five irrigation areas are shown. Different symbols dots represent different places. The black dashed line represents the same magnitude between net radiation and PET.

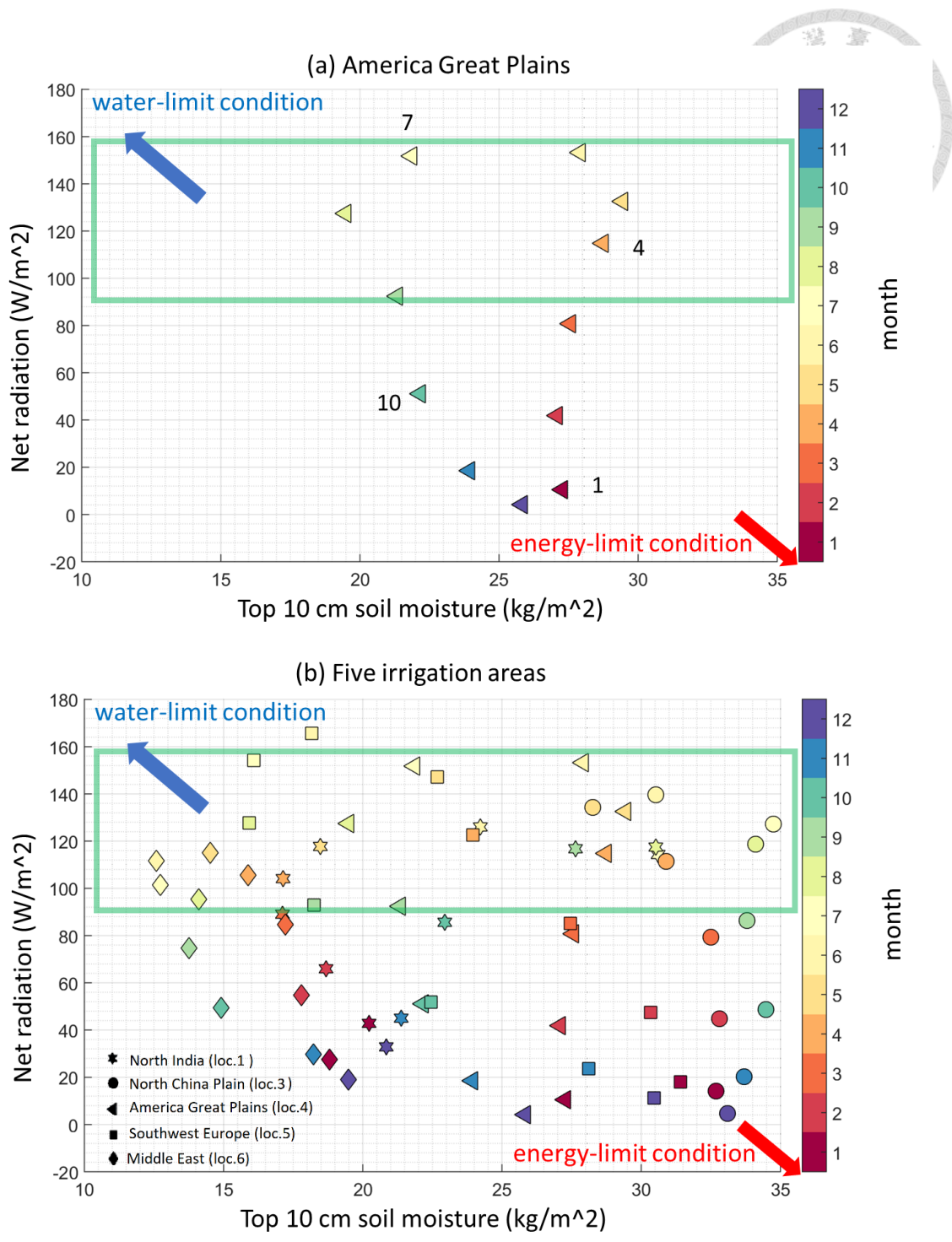


Figure 2.6 Seasonal cycle of (a) America Great Plains (location No 4) and (b) five irrigation areas in F_{ctl} as examples of hydroclimatological scatter chart. Green box stands for data under higher net radiation. X axis: top 10 cm soil moisture (kg/m^2) of F_{ctl} ; Y axis: net radiation of F_{ctl} . Different symbols represent different places.

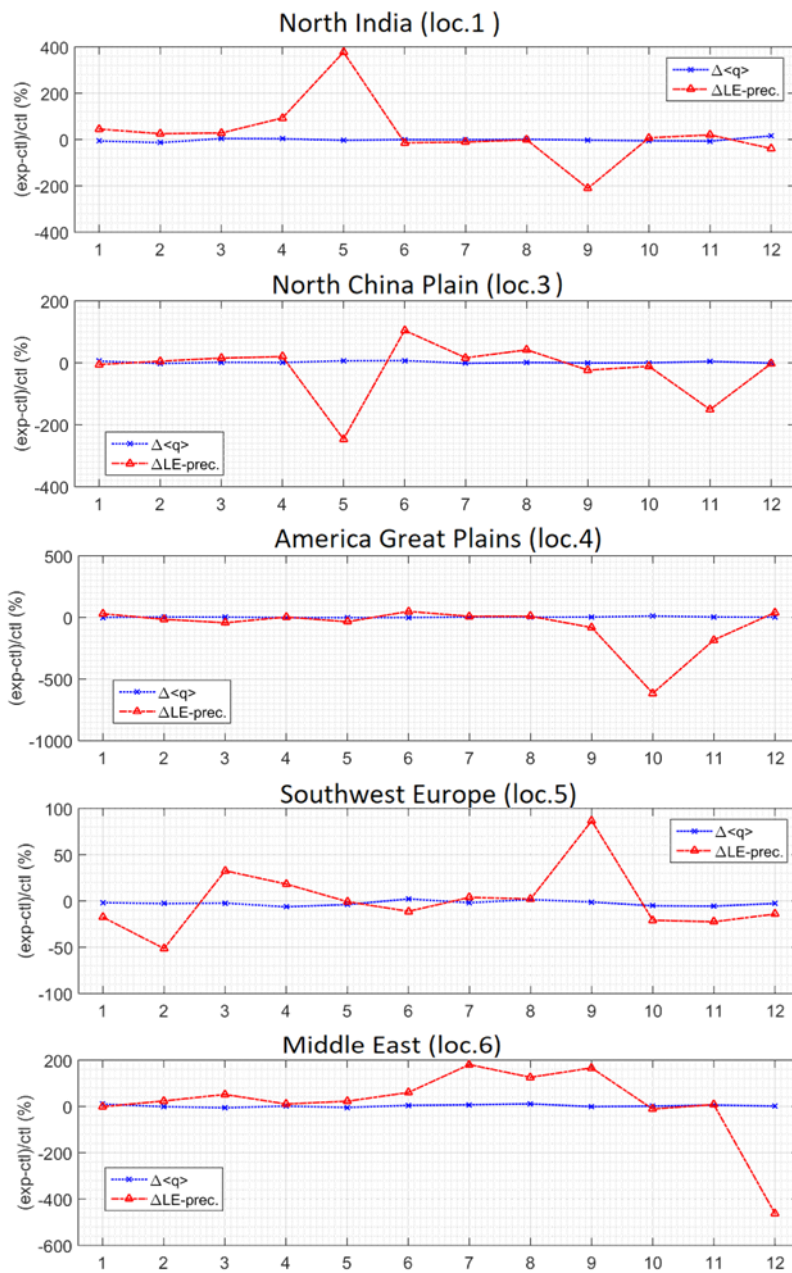


Figure 2.7.1 The differences of vertically integrated moisture (blue) and evapotranspiration minus precipitation (red) after irrigation: $F_{\text{self}} - F_{\text{ctl}}$. X axis: month.

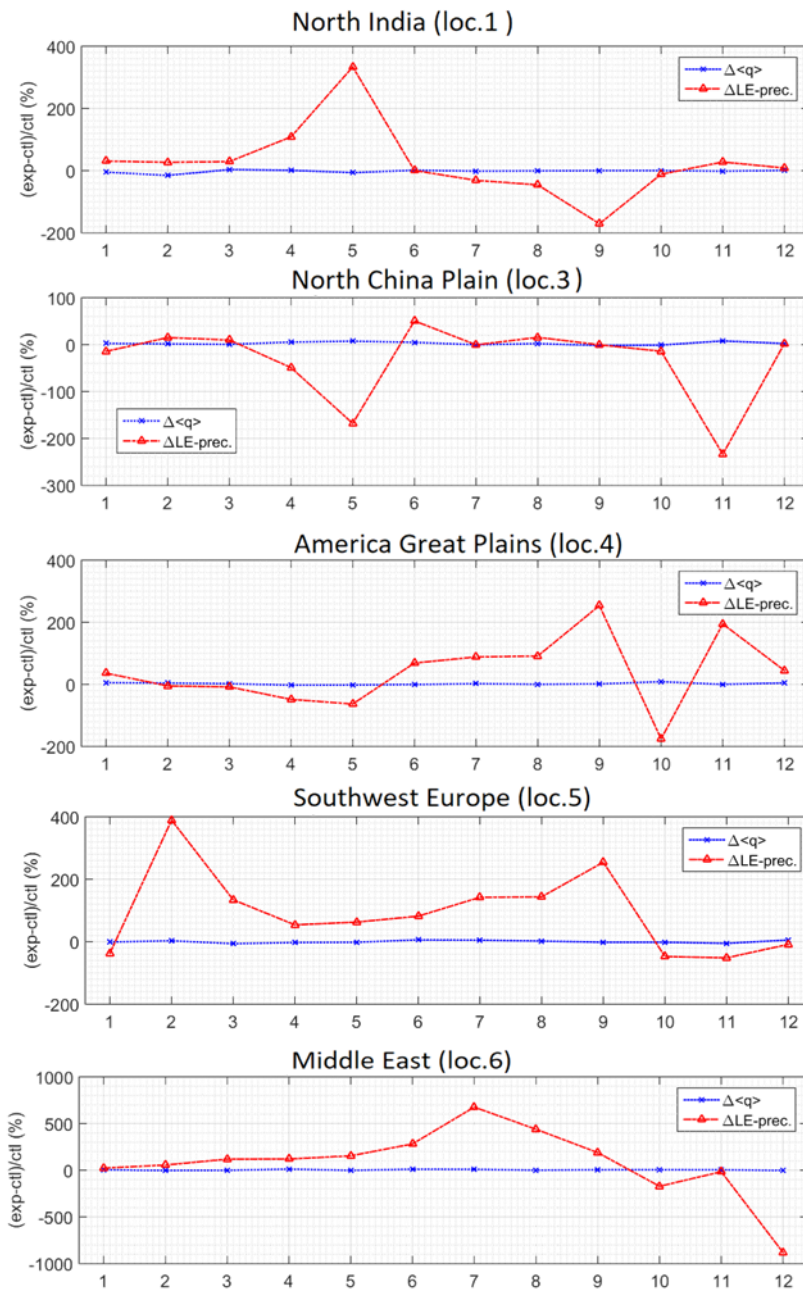


Figure 2.7.2 The differences of vertically integrated moisture (blue) and evapotranspiration minus precipitation (red) after irrigation: $F_{\text{max}} - F_{\text{ctl}}$. X axis: month.

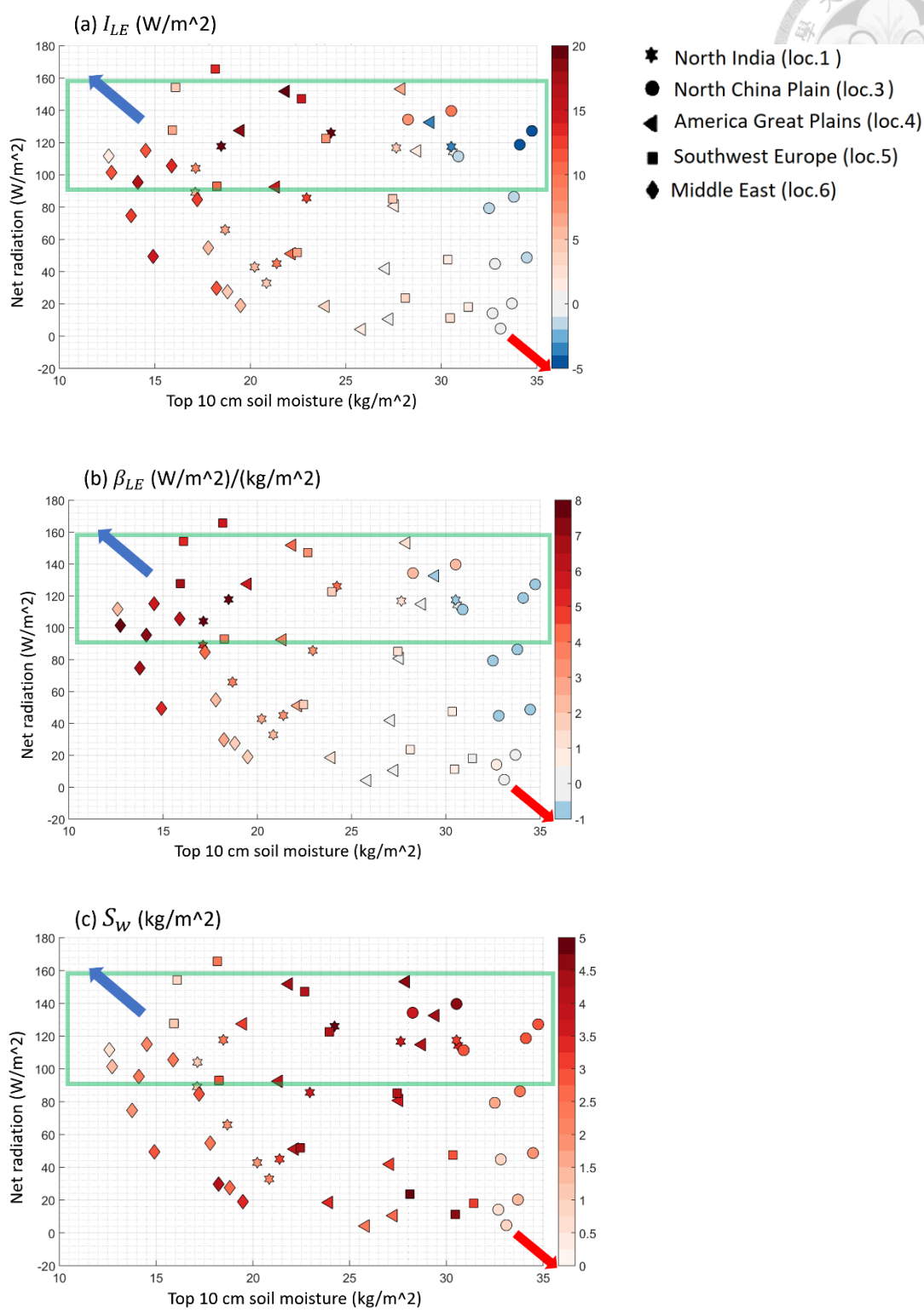


Figure 3.1.1 Hydroclimatological scatter chart of I_{LE} from F_ctl. (a) I_{LE} (W/m^2): coupling strength between soil moisture and evapotranspiration, (b) β_{LE} ($(W/m^2)/(kg/m^2)$): the slope between soil moisture and evapotranspiration, (c) S_w (kg/m^2): the standard deviation of daily soil moisture. Different symbols represent different places.

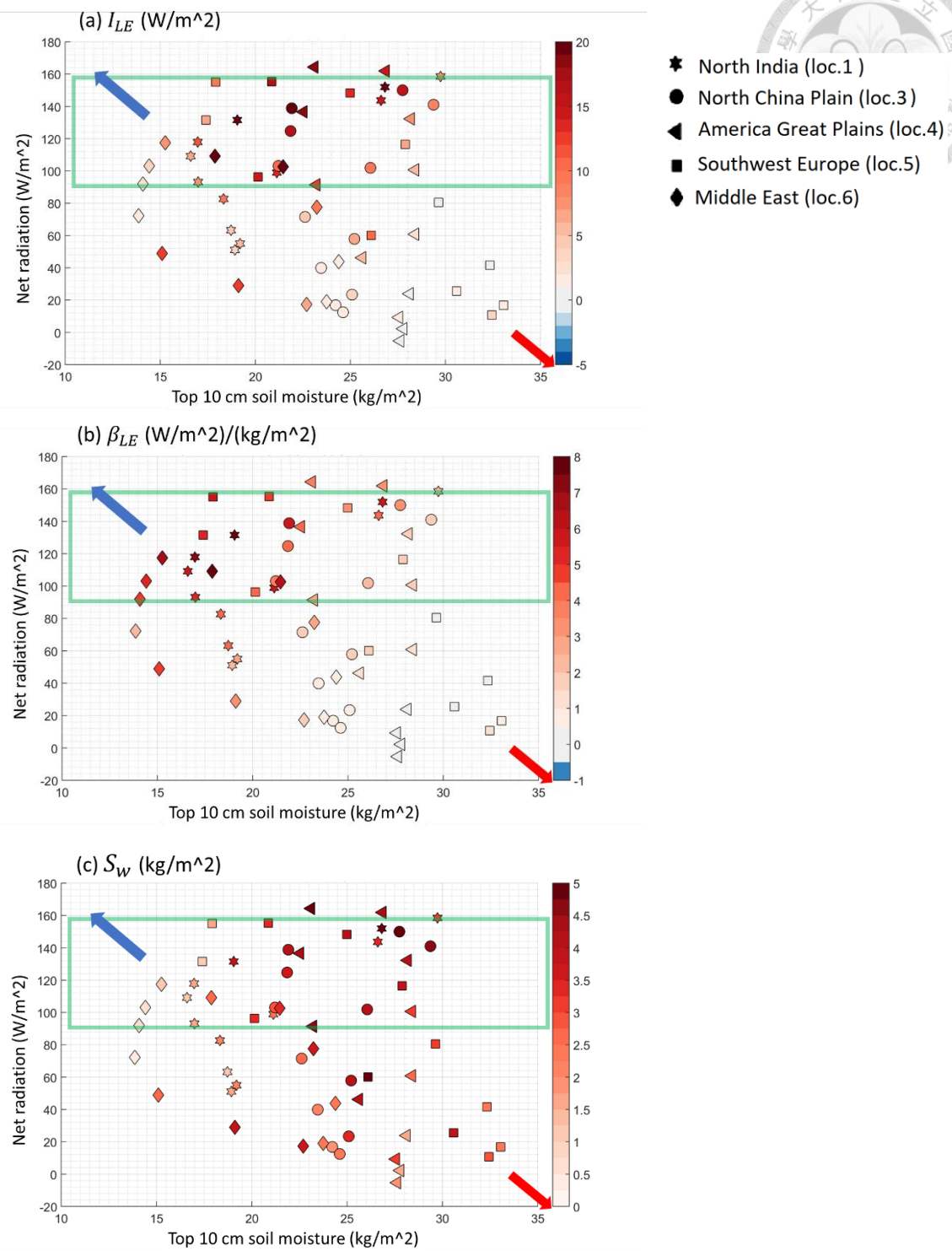


Figure 3.1.2 Hydroclimatological scatter chart of I_{LE} from I_ctl. (a) I_{LE} (W/m^2): coupling strength between soil moisture and evapotranspiration, (b) β_{LE} ($(W/m^2)/(kg/m^2)$): the slope between soil moisture and evapotranspiration, (c) S_w (kg/m^2): the standard deviation of daily soil moisture. Different symbols represent different places.

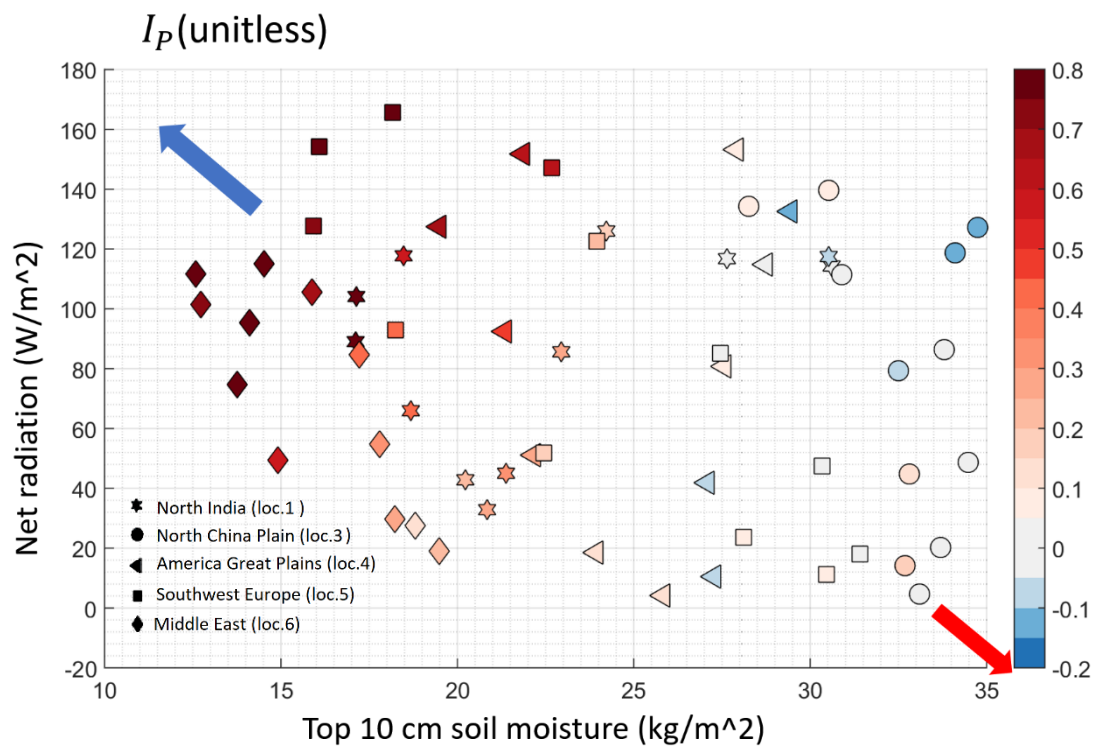


Figure 3.2 Hydroclimatological scatter chart of I_p , the coupling between evapotranspiration and precipitation, from F_ctl. Different symbols represent different places.

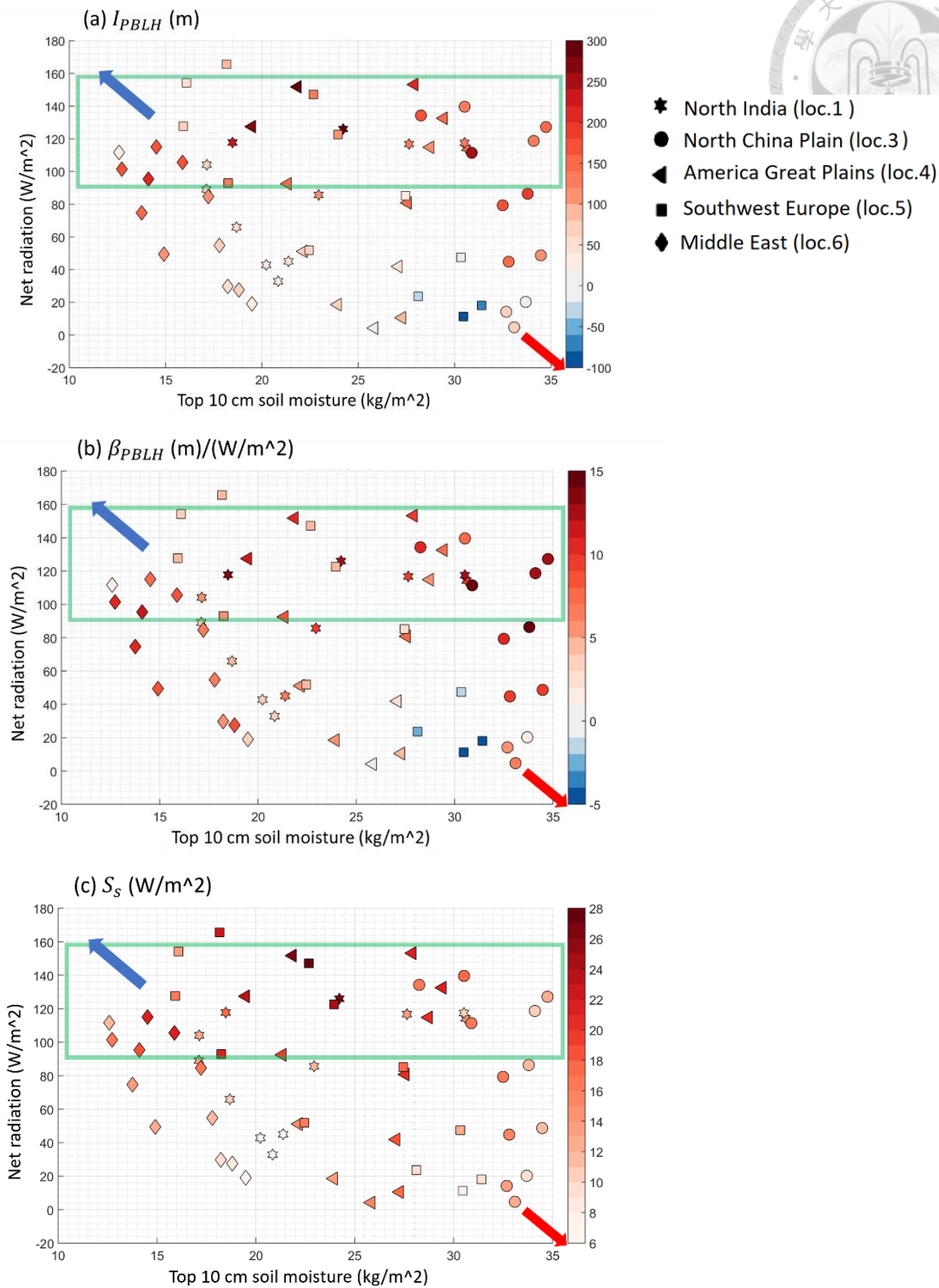


Figure 3.3 Hydroclimatological scatter chart of I_{PBLH} from F_ctl. (a) I_{PBLH} (m): coupling strength between sensible heat flux and boundary layer height, (b) β_{PBLH} (m/(W/m²)): the slope between sensible heat flux and boundary layer height, (c) S_s (W/m²): the standard deviation of daily sensible heat flux. Different symbols represent different places.

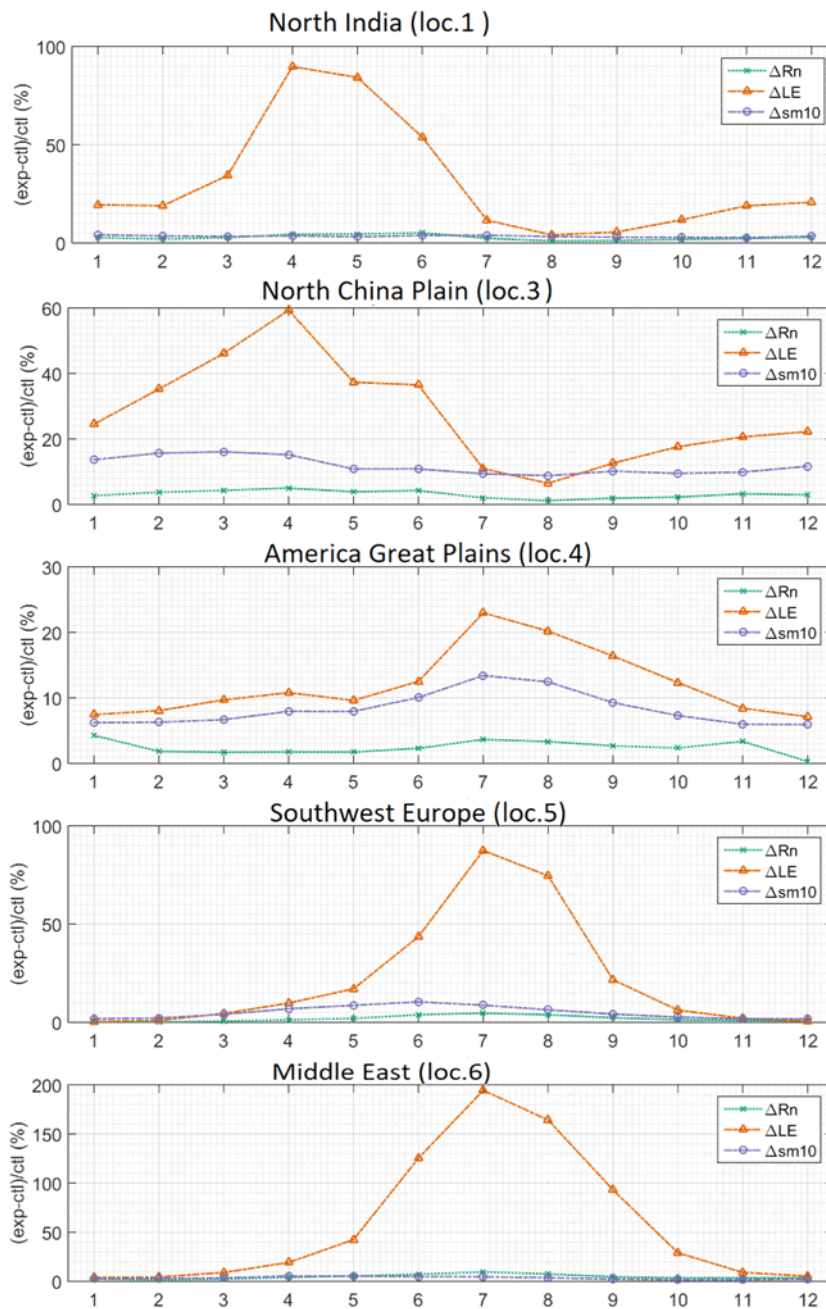


Figure 3.4.1 The differences of surface net radiation (green, downward positive), evapotranspiration (orange, upward positive) and top 10 cm soil moisture (blue) after irrigation: $I_{max} - I_{ctl}$. X axis: month.

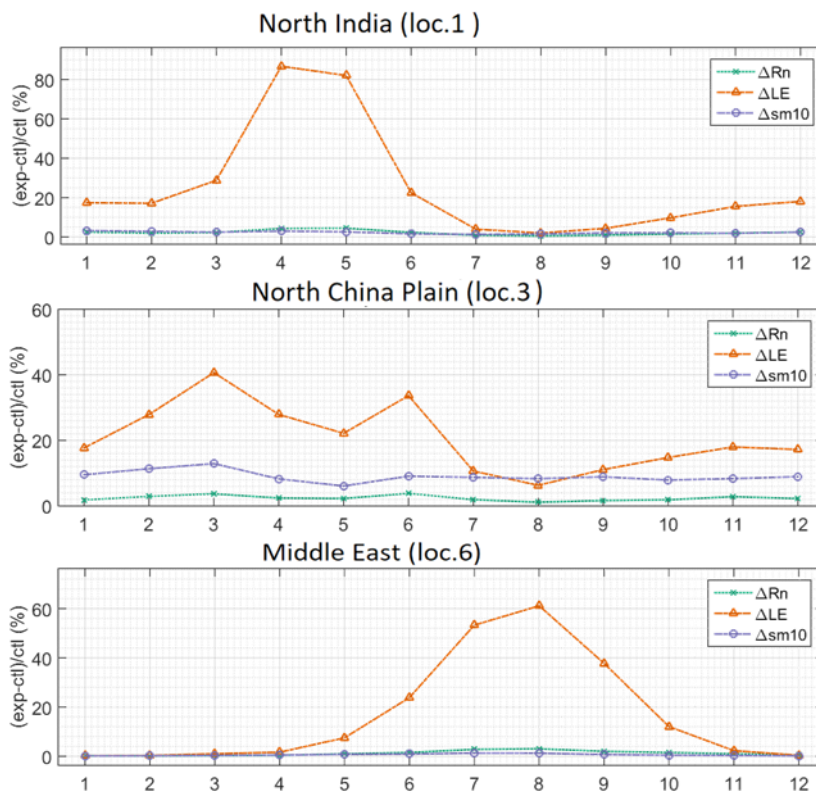
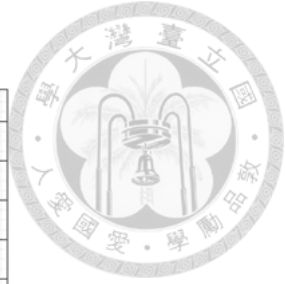


Figure 3.4.2 The differences of surface net radiation (green, downward positive), evapotranspiration (orange, upward positive) and top 10 cm soil moisture (blue) after irrigation: $I_{self} - I_{ctl}$. X axis: month.

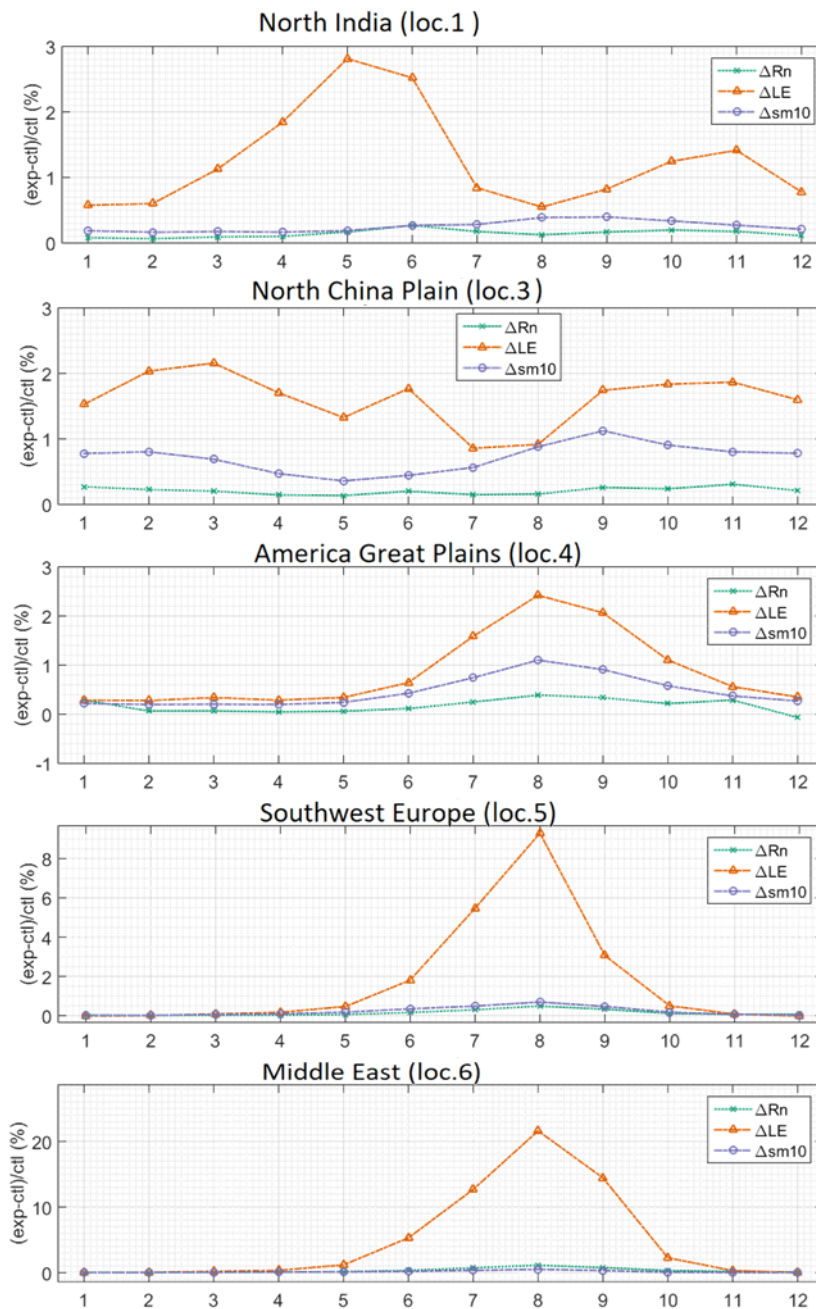
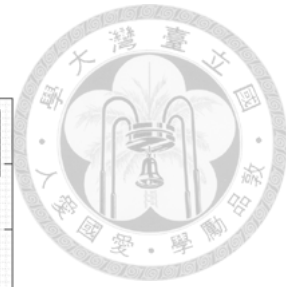


Figure 3.4.3 The differences of surface net radiation (green, downward positive), evapotranspiration (orange, upward positive) and top 10 cm soil moisture (blue) after irrigation: $I_{min} - I_{ctl}$. X axis: month.

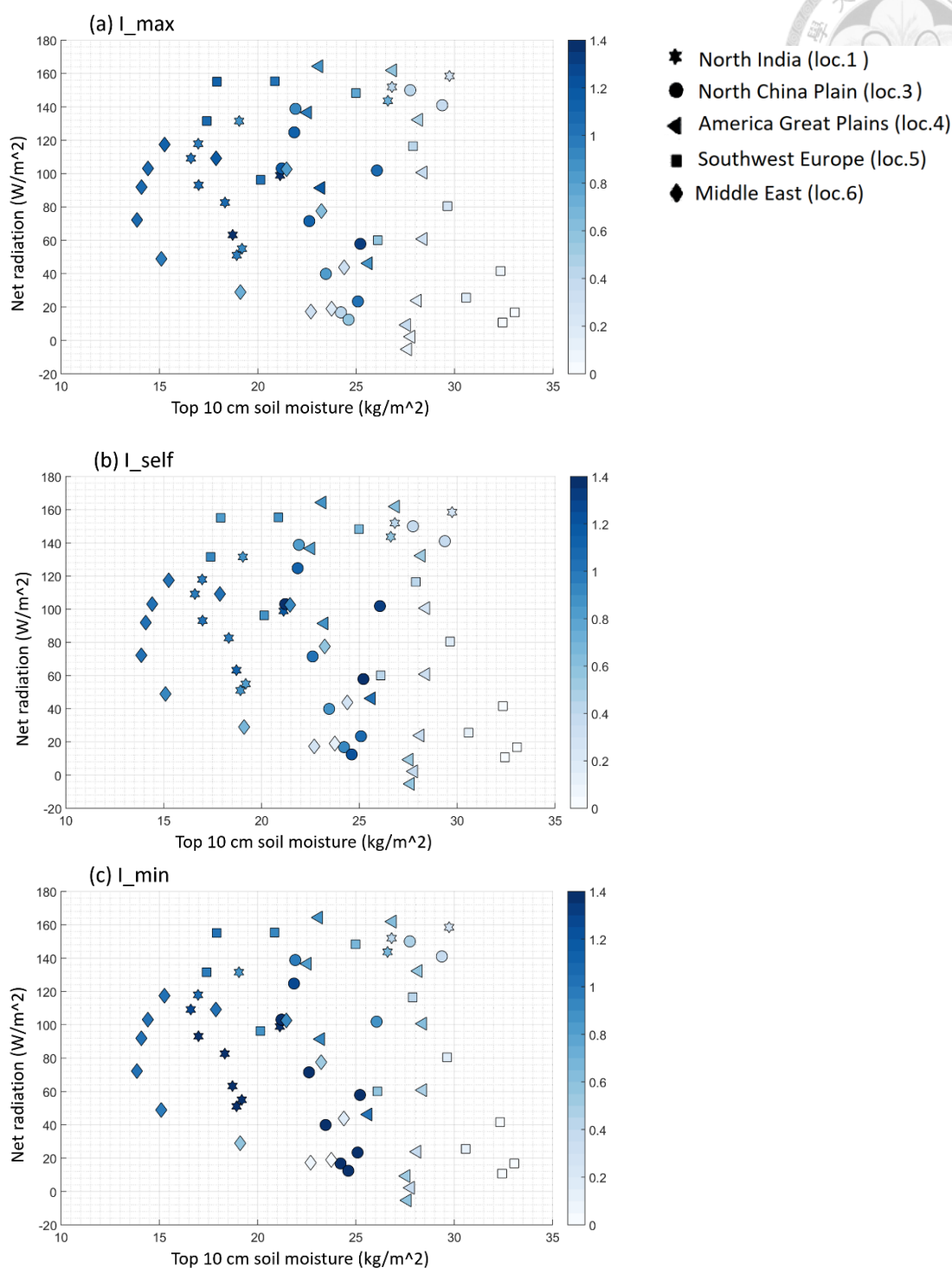


Figure 3.5 Hydroclimatological scatter chart of Δ evapotranspiration/ Δ irrigation (unitless). (a) $I_{max} - I_{ctl}$, (b) $I_{self} - I_{ctl}$, (c) $I_{min} - I_{ctl}$. X axis: top 10 cm soil moisture (kg/m^2) of I_{ctl} ; Y axis: net radiation of I_{ctl} .

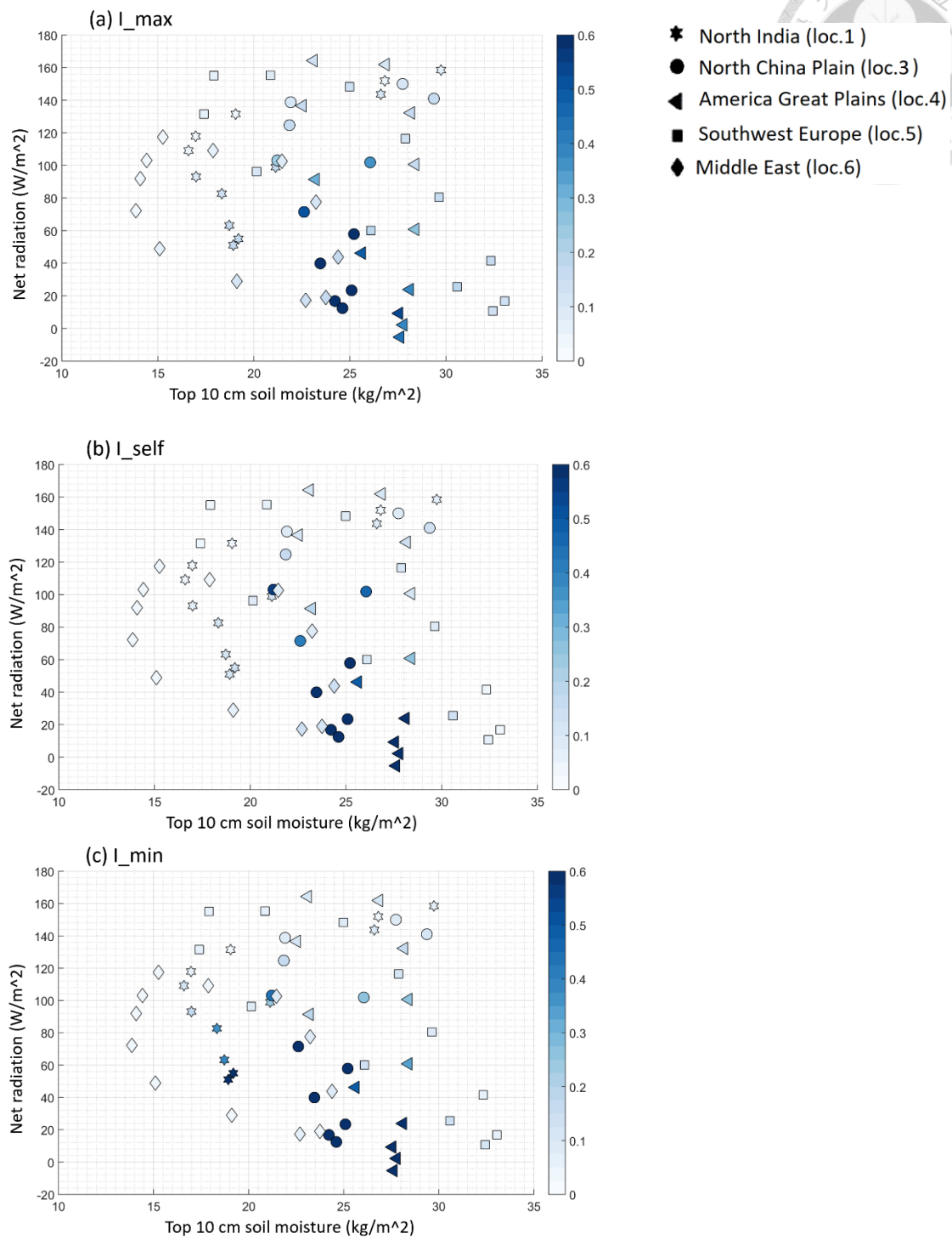


Figure 3.6 Hydroclimatological scatter chart of Δ soil moisture of top 10 cm depth/ Δ irrigation ($(\text{kg/m}^2)/(\text{W/m}^2)$). (a) $I_{\text{max}} - I_{\text{ctl}}$, (b) $I_{\text{self}} - I_{\text{ctl}}$, (c) $I_{\text{min}} - I_{\text{ctl}}$. X axis: top 10 cm soil moisture (kg/m^2) of I_{ctl} ; Y axis: net radiation of I_{ctl} .

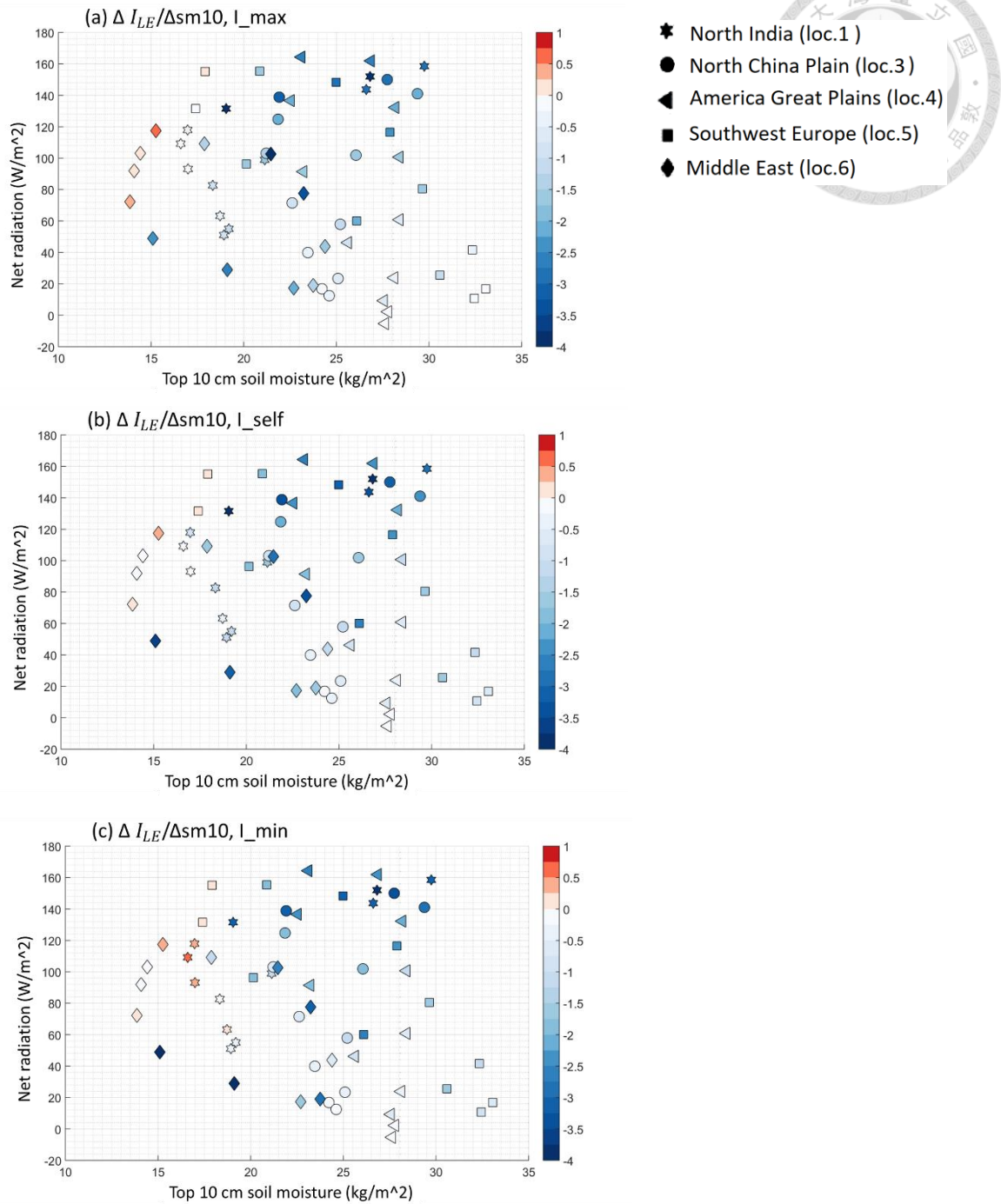


Figure 3.7.1 Hydroclimatological scatter chart of $\Delta I_{LE}/\Delta sm10$ ((W/m²)/(kg/m²)): (a) $I_{max} - I_{ctl}$, (b) $I_{self} - I_{ctl}$, (c) $I_{min} - I_{ctl}$. Different symbols represent different places. $\Delta sm10$ represents change of top 10 cm depth soil moisture. X axis: top 10 cm soil moisture (kg/m²) of I_{ctl} ; Y axis: net radiation of I_{ctl} .

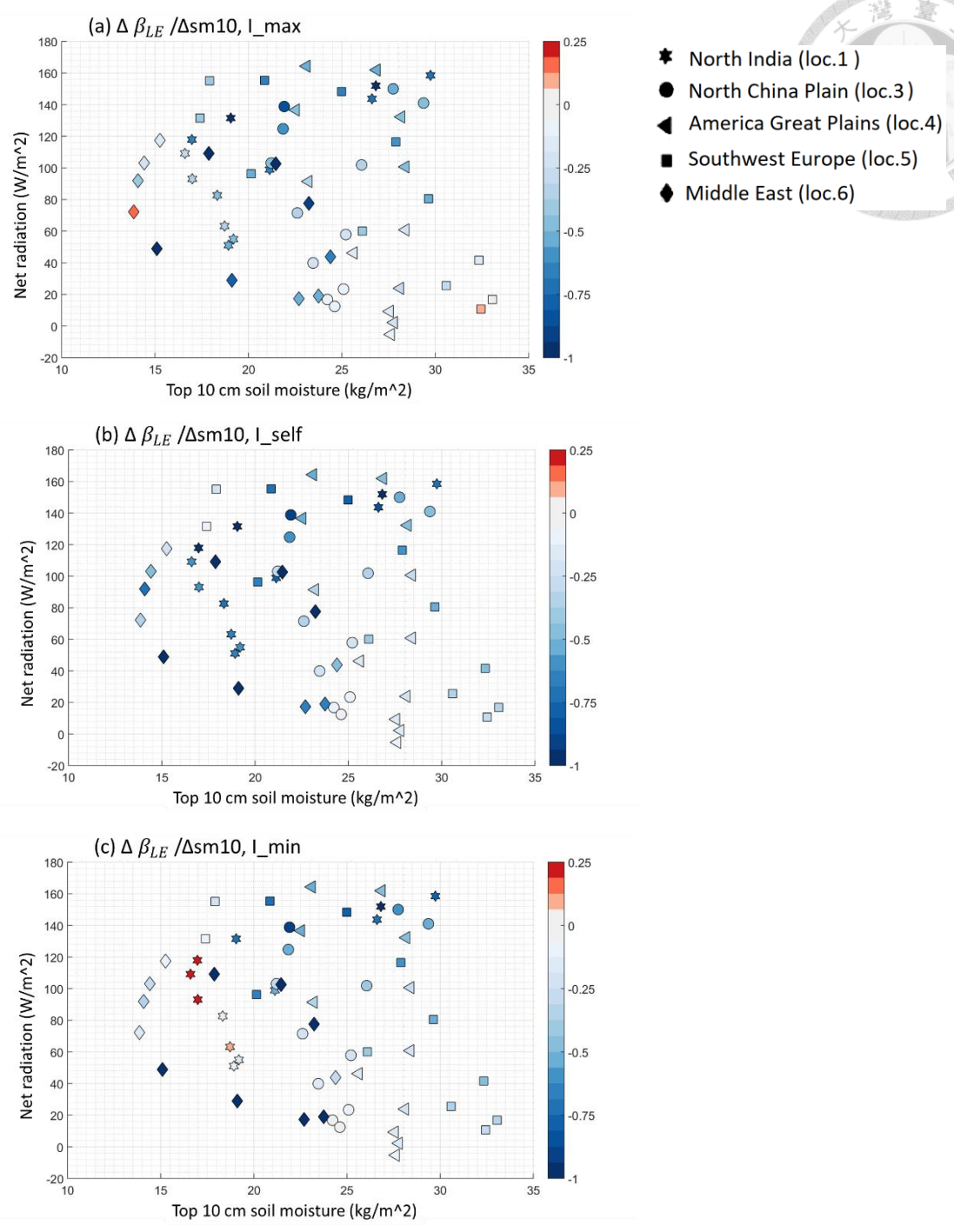
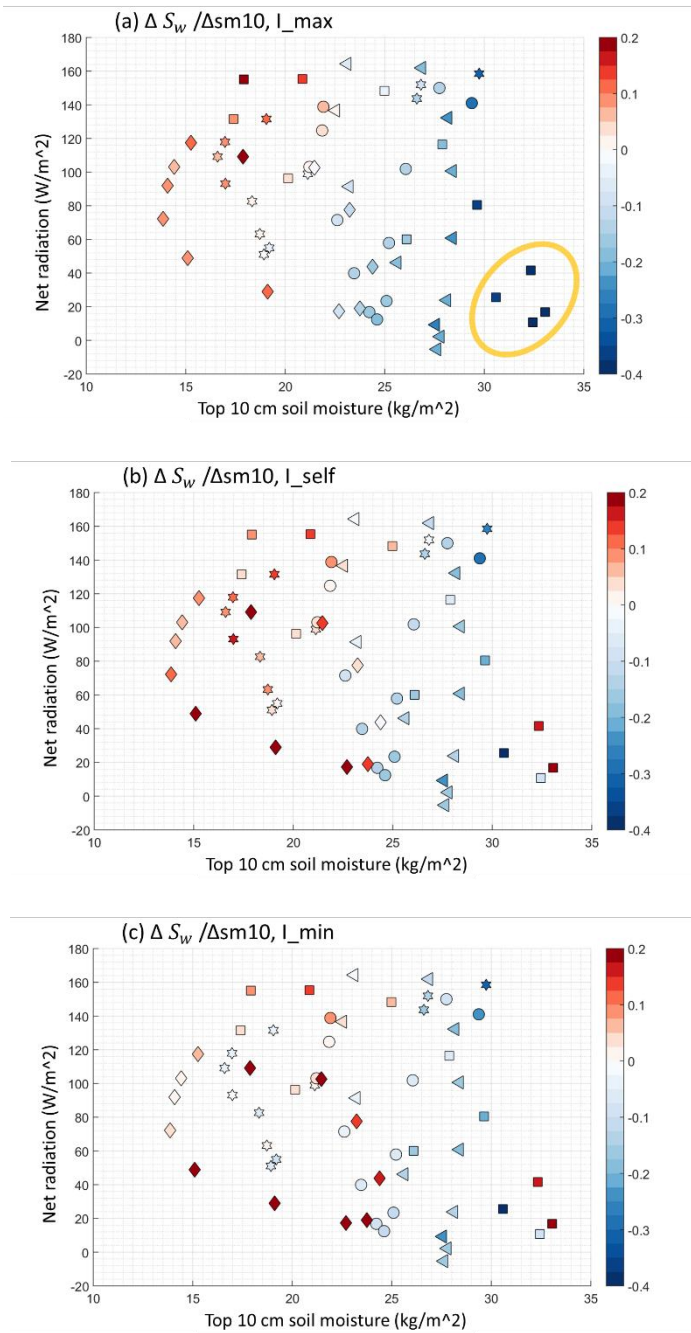


Figure 3.7.2 Hydroclimatological scatter chart of $\Delta \beta_{LE} / \Delta sm_{10}$ ($(W/m^2)/(kg/m^2)^2$) after irrigation: (a) $I_max - I_ctl$, (b) $I_self - I_ctl$, (c) $I_min - I_ctl$. Different symbols represent different places. Δsm_{10} represents change of top 10 cm depth soil moisture. X axis: top 10 cm soil moisture (kg/m^2) of I_ctl ; Y axis: net radiation of I_ctl .



- ★ North India (loc.1)
- North China Plain (loc.3)
- ◀ America Great Plains (loc.4)
- Southwest Europe (loc.5)
- ◆ Middle East (loc.6)

Figure 3.7.3 Hydroclimatological scatter chart of $\Delta S_w / \Delta sm10$ (unitless) after irrigation: (a) $I_{max} - I_{ctl}$, (b) $I_{self} - I_{ctl}$, (c) $I_{min} - I_{ctl}$. Different symbols represent different places. $\Delta sm10$ represents change of top 10 cm depth soil moisture. X axis: top 10 cm soil moisture (kg/m^2) of I_{ctl} ; Y axis: net radiation of I_{ctl} .

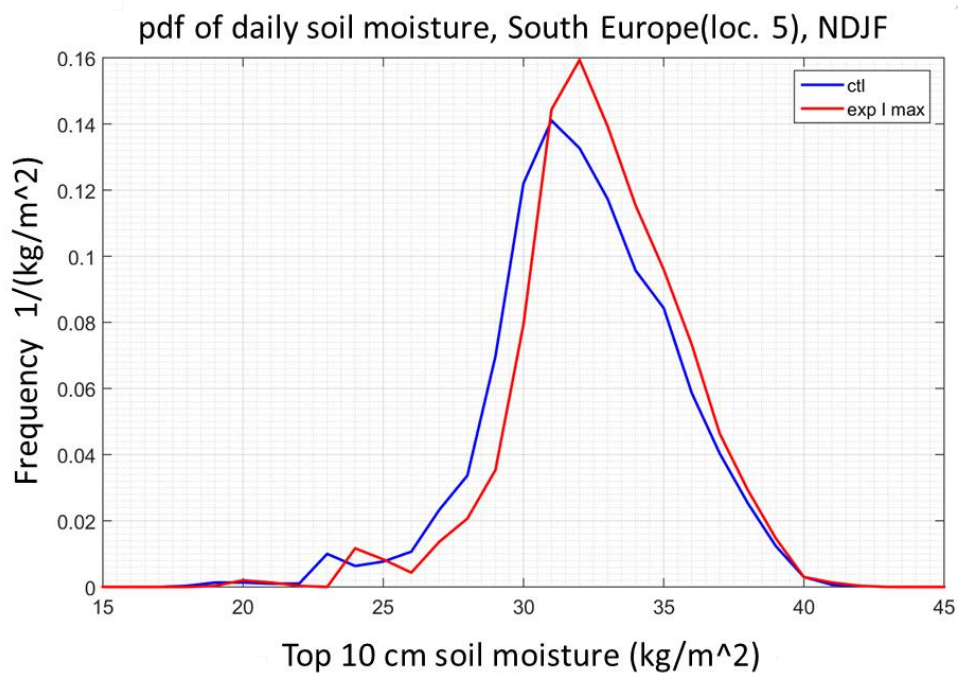


Figure 3.8 The probability density function of daily soil moisture of South Europe (location No 5) over 25 years from November to February. Blue line: I_{ctl} ; red line: I_{max} . Data corresponds to orange circle in Figure 3.7.3(a).

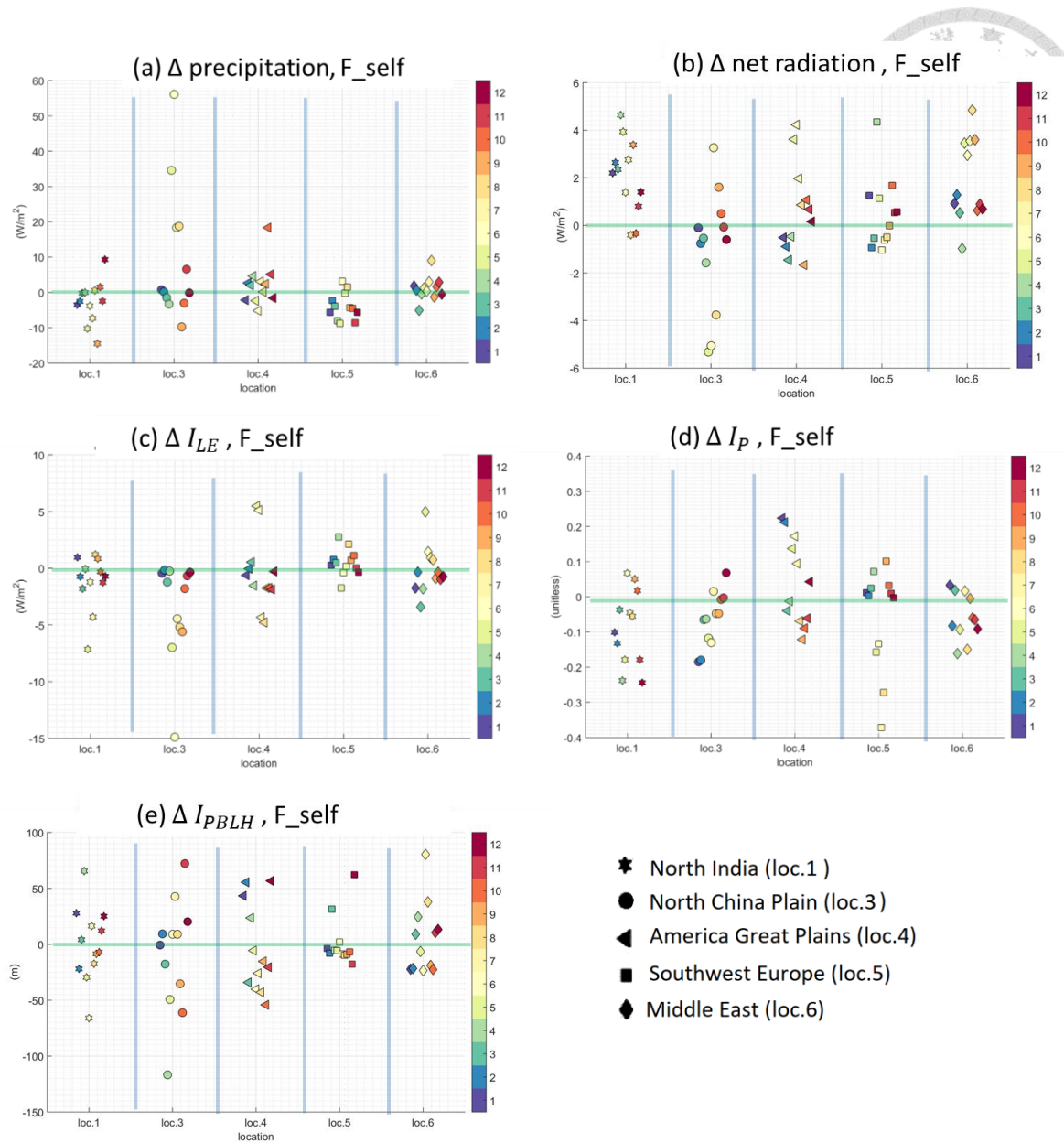


Figure 3.9.1 Differences after irrigation: $F_{self} - F_{ctl}$. (a) precipitation, (b) net radiation, (c) I_{LE} , (d) I_P , (e) I_{PBLH} . The color of dots represent month. At each location, data approaching to left X axis represent earlier month, corresponding to the shaded color.

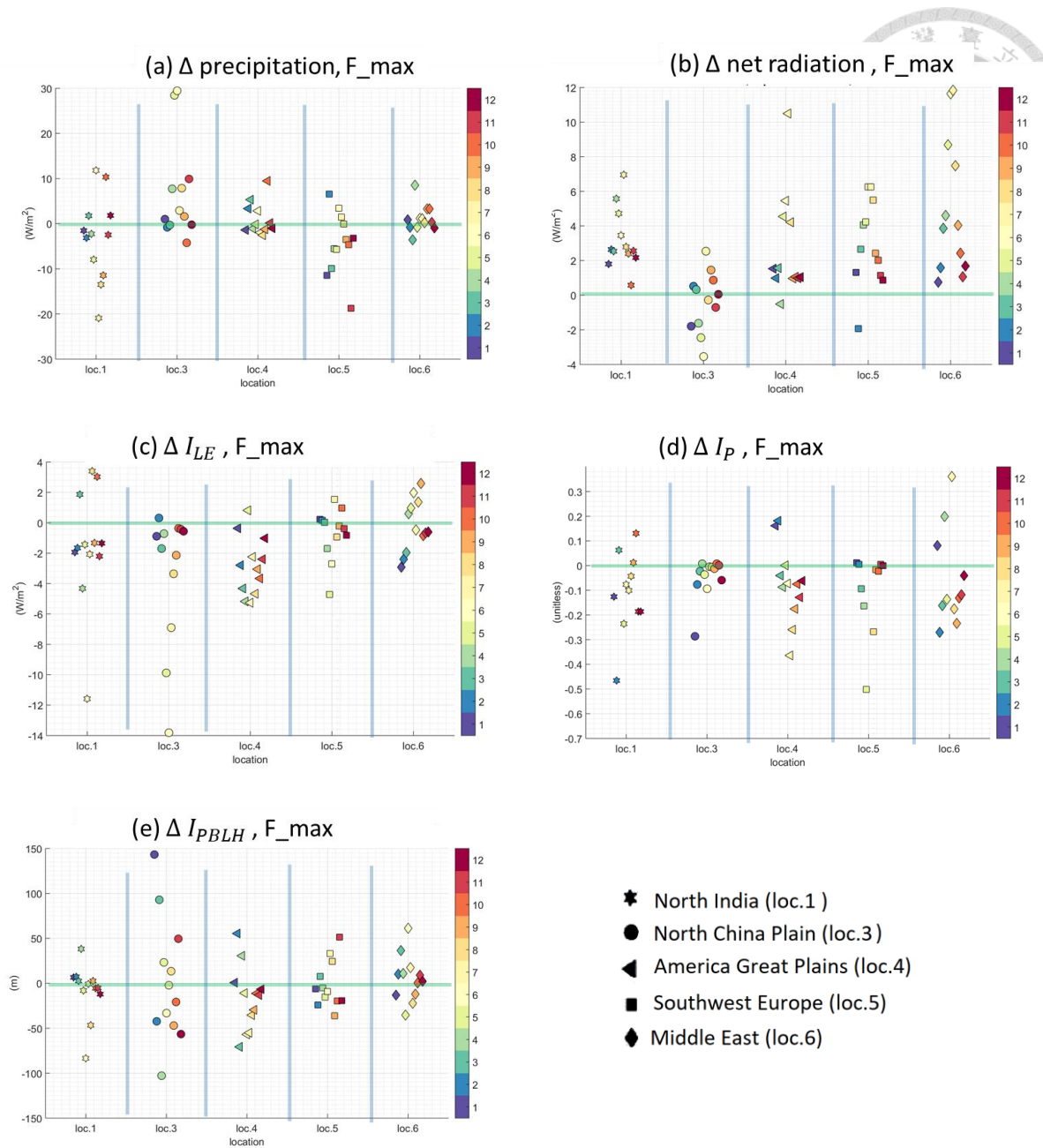


Figure 3.9.2 Differences after irrigation: $F_{\max} - F_{\text{ctl}}$. (a) precipitation, (b) net radiation, (c) I_{LE} , (d) I_P , (e) I_{PBLH} . The color of dots represent month. At each location, data approaching to left X axis represent earlier month, corresponding to the shaded color.

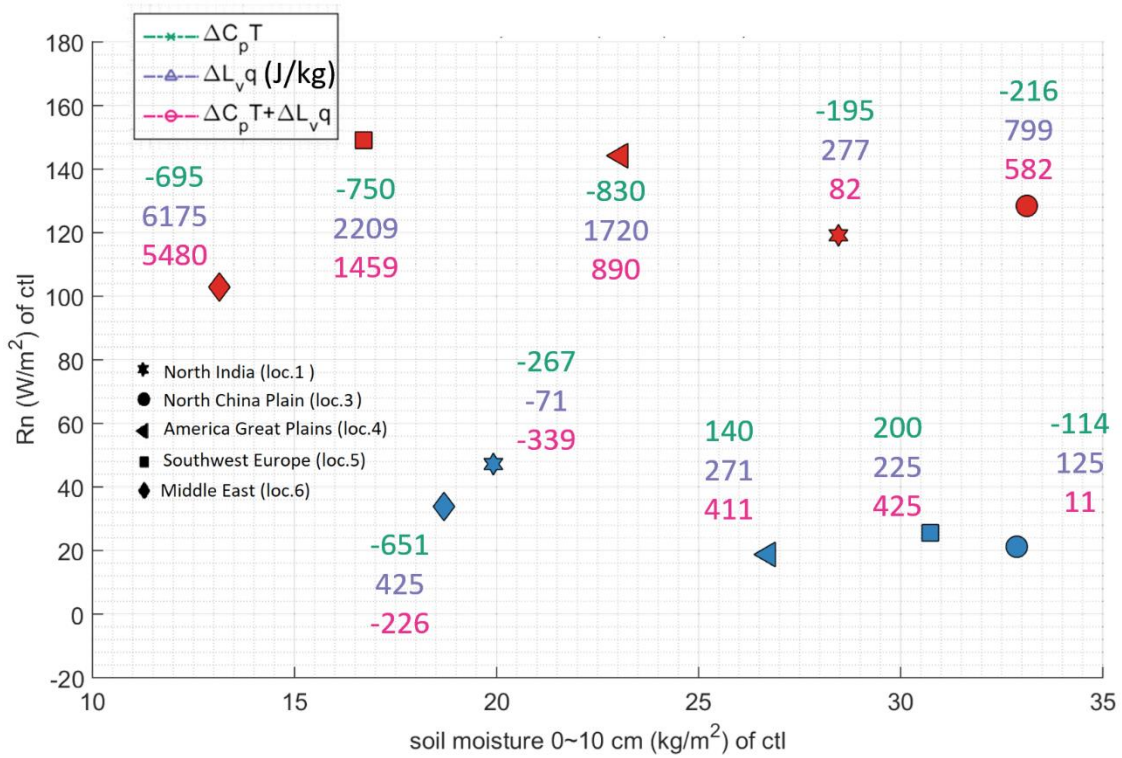


Figure 3.10 Hydroclimatological scatter chart of seasonal mean from F_ctl. Red dots: JJA; blue dots: DJF. Numbers represent the magnitude of surface cooling effect (green), moistening effect (purple) and total effect (pink) of F_max – F_ctl. Note that during the same season, irrigated water is same among five areas; also, the irrigation in JJA is stronger than DJF (Figure 2.3).

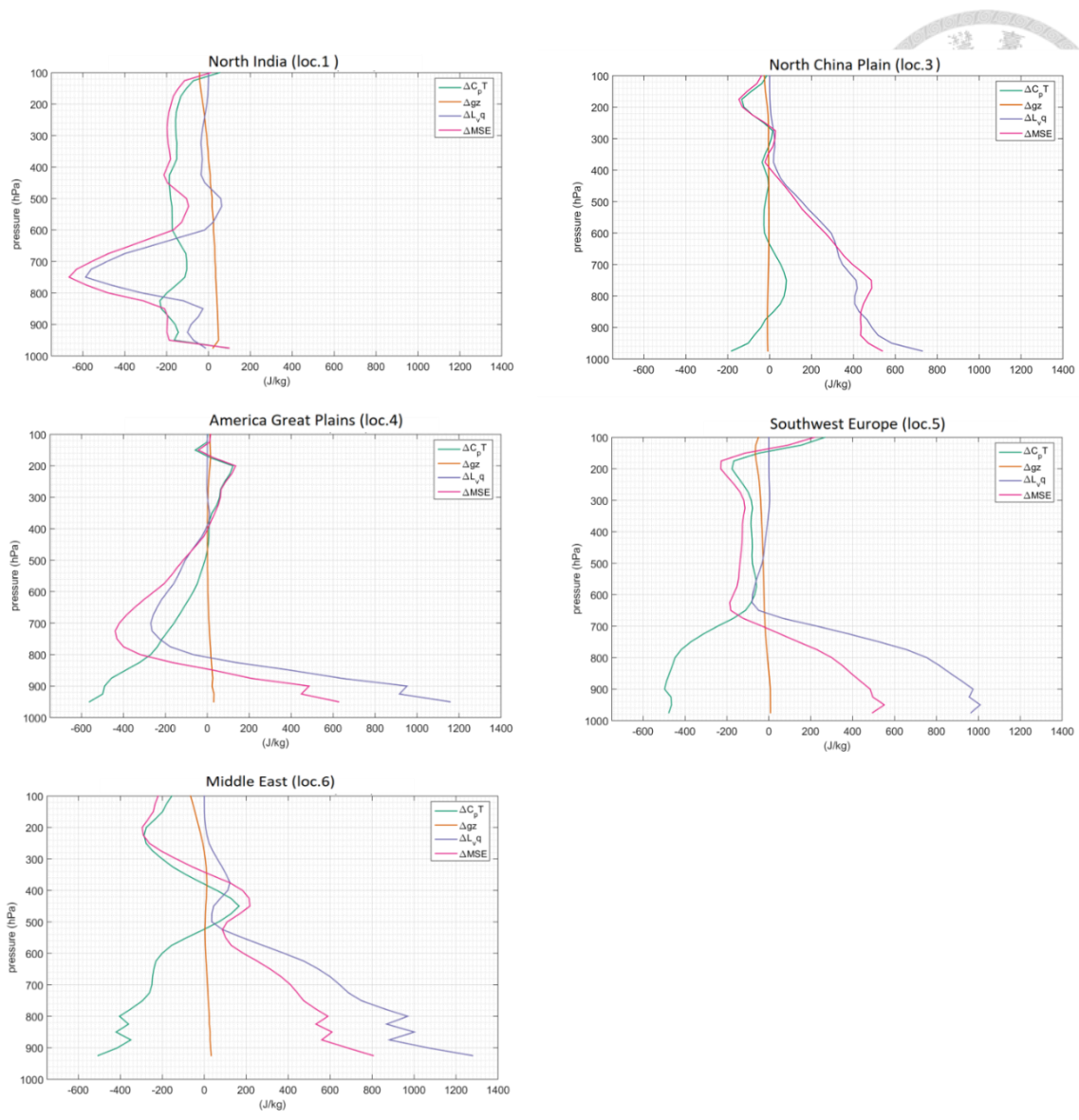


Figure 3.11.1 The differences of MSE vertical structure in JJA after irrigation: $F_{max} - F_{ctl}$.

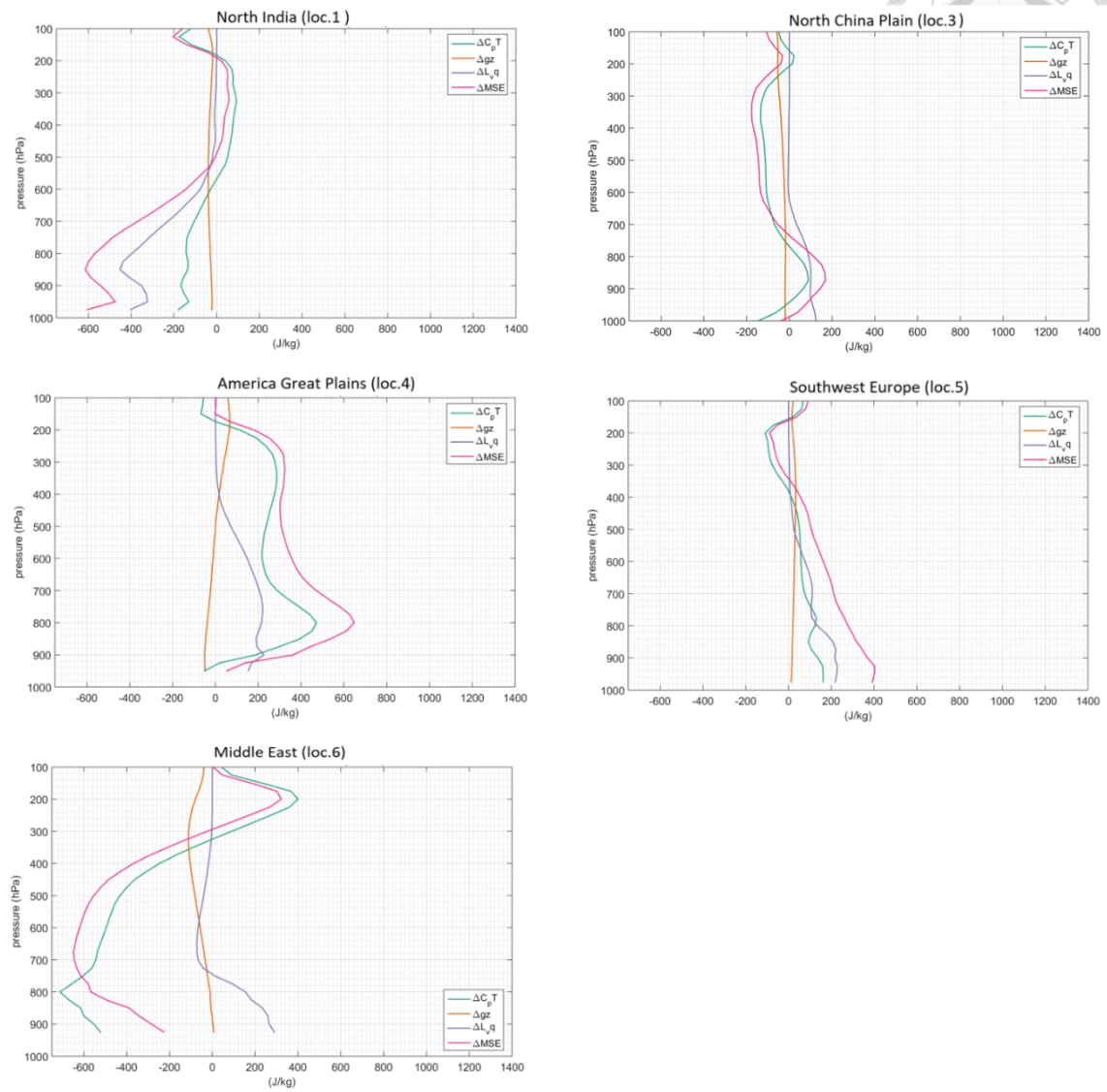


Figure 3.11.2 The differences of MSE vertical structure in DJF after irrigation: $F_{max} - F_{ctl}$.

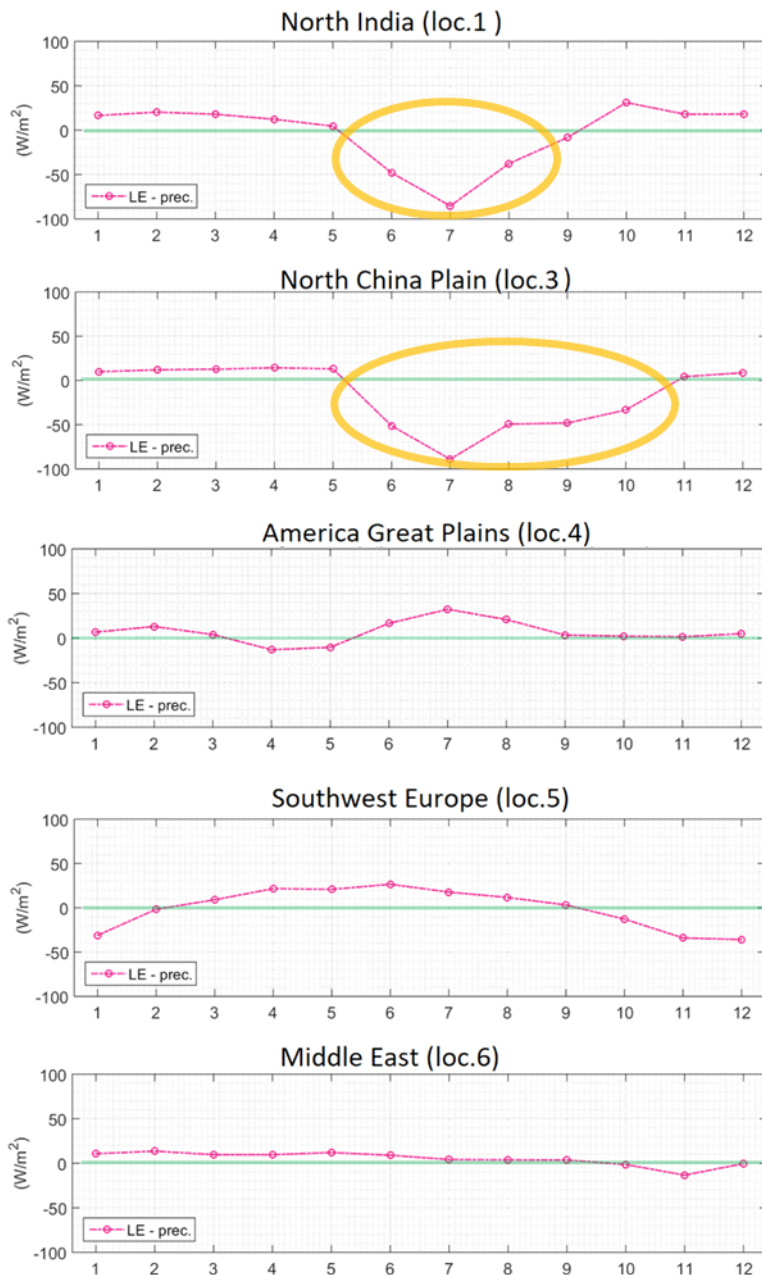


Figure 3.12 Atmospheric column water budget analysis of F_{ctl} : evapotranspiration (upward positive) minus precipitation (downward positive). Negative value indicates non-local water vapor sources for precipitation. X axis: month. LE: evapotranspiration; prec.: precipitation.

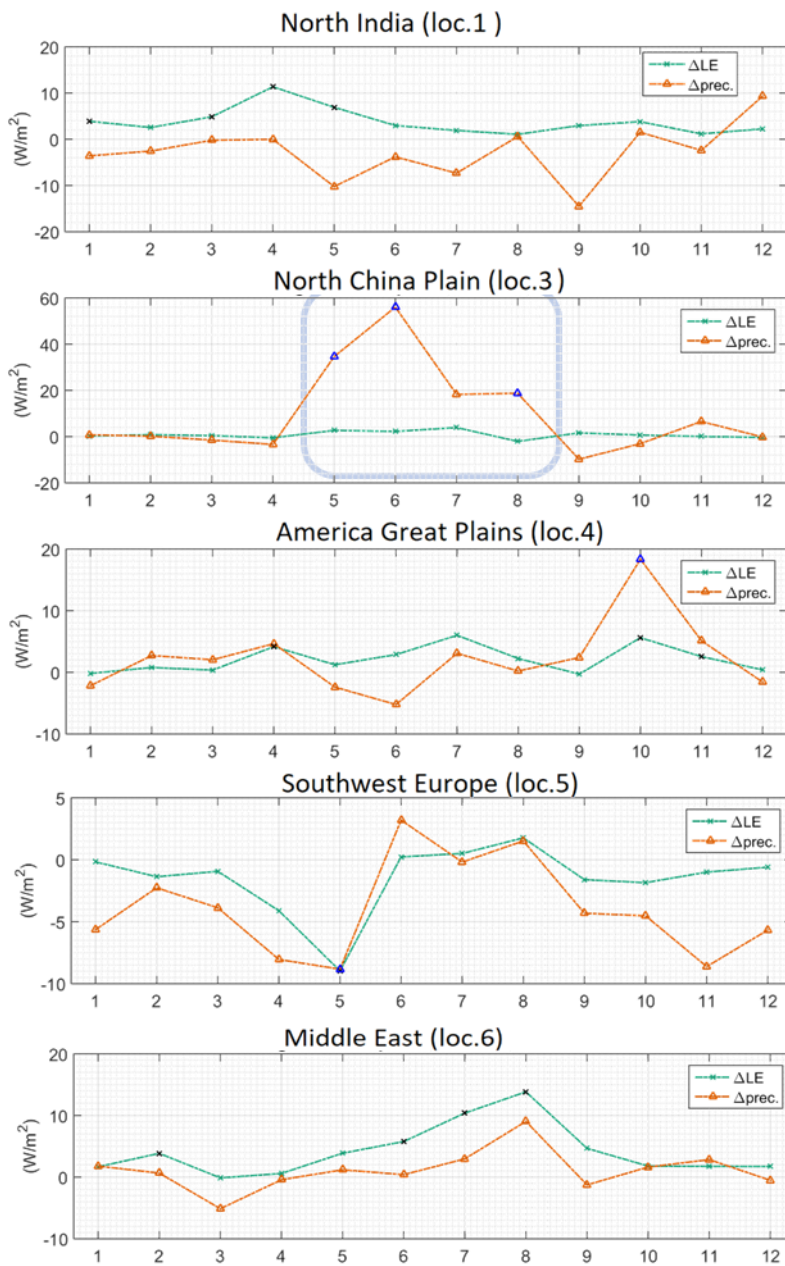


Figure 3.13.1 Atmospheric column water budget differences after irrigation: $F_{self} - F_{ctl}$. Black and blue dots represent that the difference pass the unpaired t-test under 95% significant level. X axis: month. LE: evapotranspiration; prec.: precipitation.

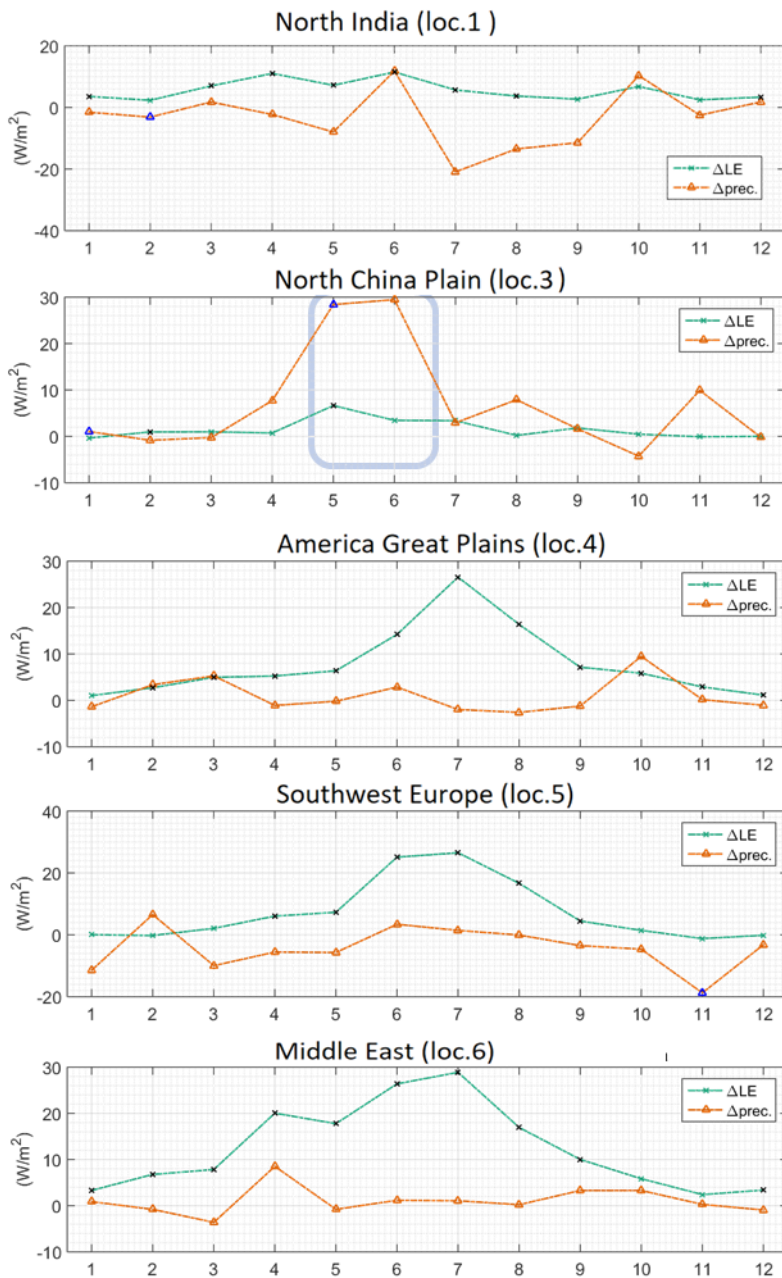


Figure 3.13.2 Atmospheric column water budget differences after irrigation: $F_{max} - F_{ctl}$. Black and blue dots represent that the differences pass the unpaired t-test under 95% significant level. X axis: month. LE: evapotranspiration; prec.: precipitation.

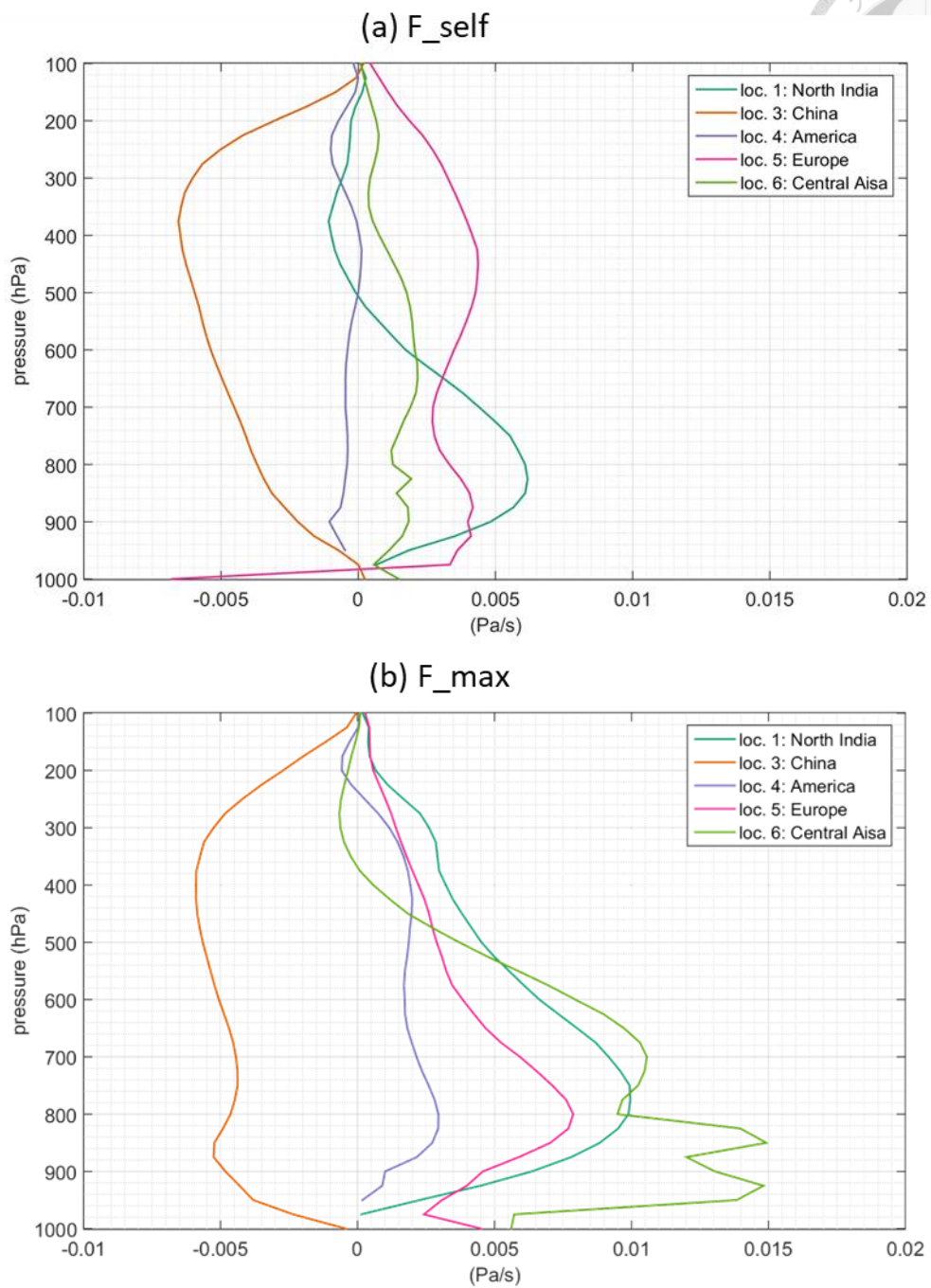


Figure 3.14 Annual mean omega differences after irrigation. (a) $F_{self} - F_{ctl}$, (b) $F_{max} - F_{ctl}$.

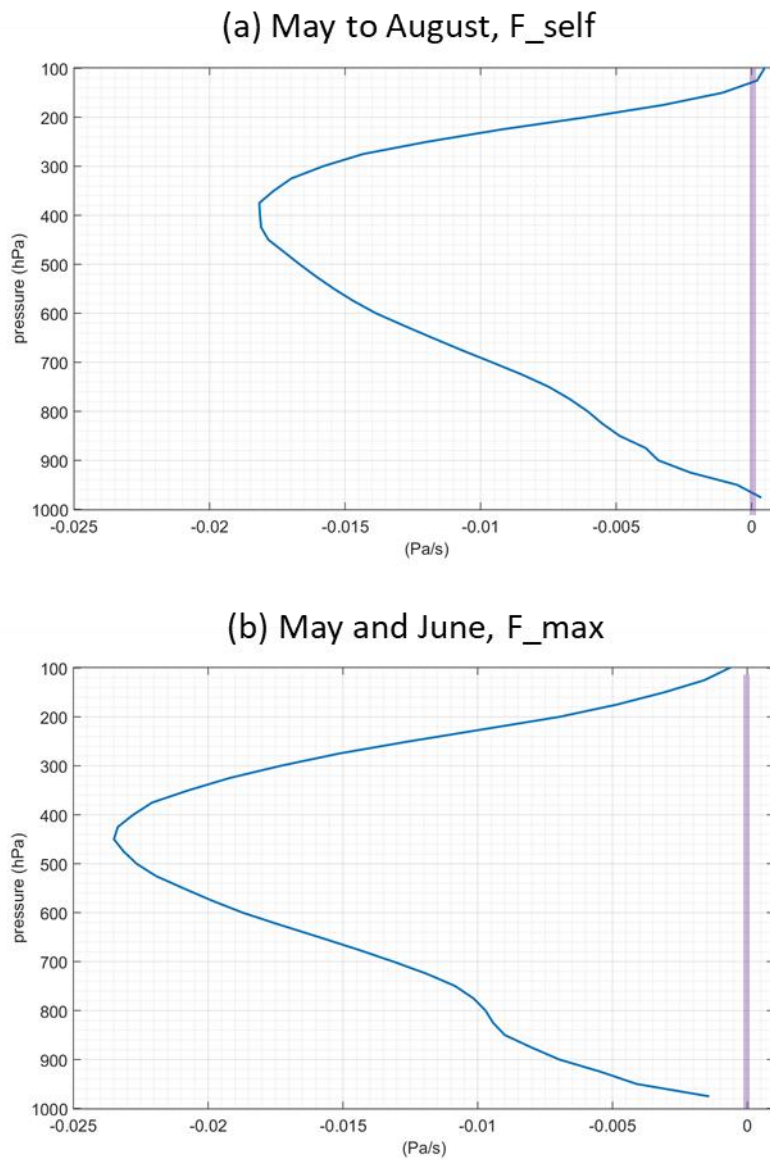


Figure 3.15 Omega differences after irrigation in North China Plain (location No 3). (a) May to August of $F_{self} - F_{ctl}$, (b) May and June of $F_{max} - F_{ctl}$. Corresponding to blue box in Figure 3.13.

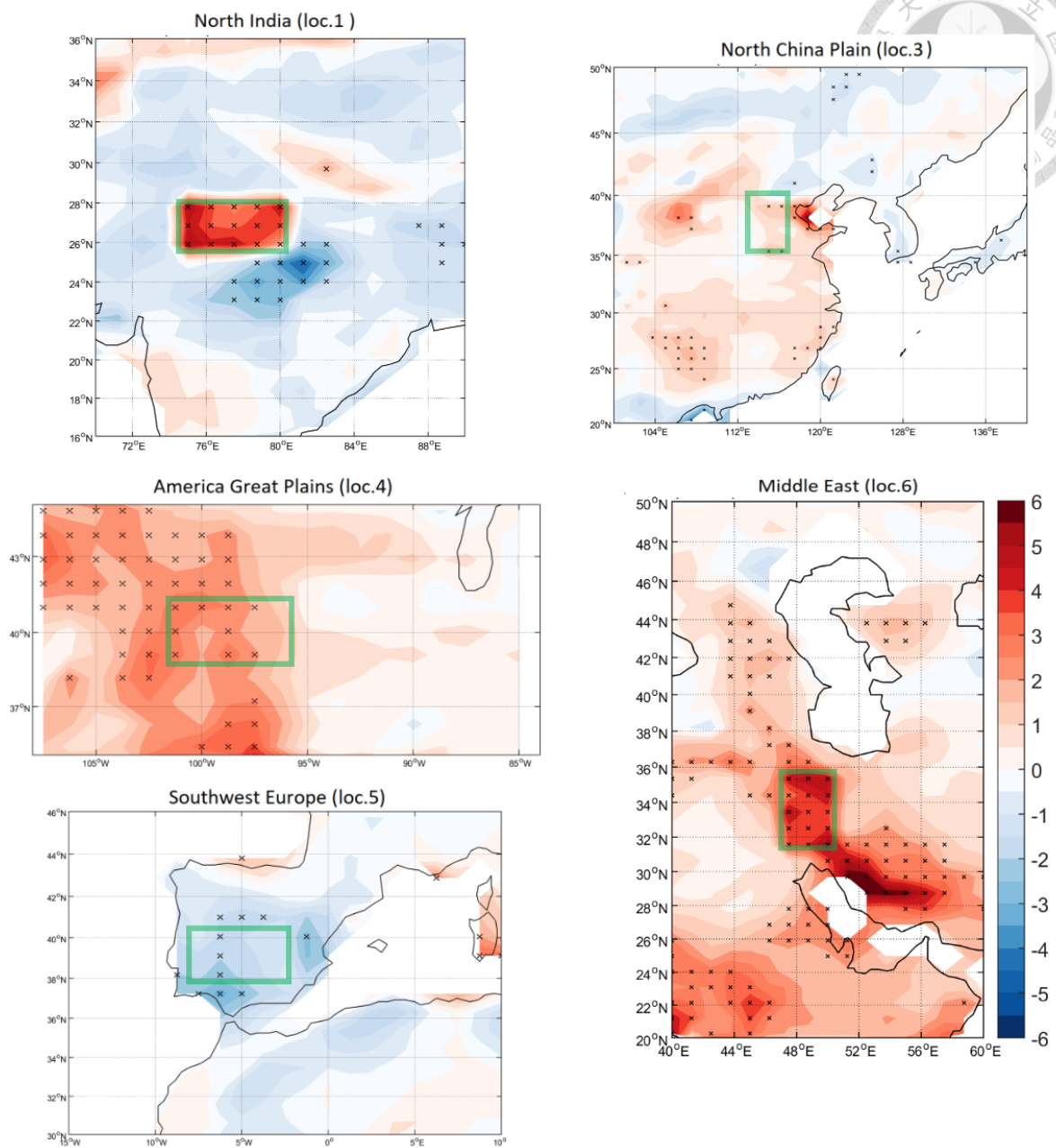


Figure 3.16.1 The differences of annual mean evapotranspiration (positive upward) after irrigation: $F_{self} - F_{ctl}$. Black crosses represent annual data which pass the unpaired two-tail t-test under 95% significant level. Green box represents irrigated area in simulations.

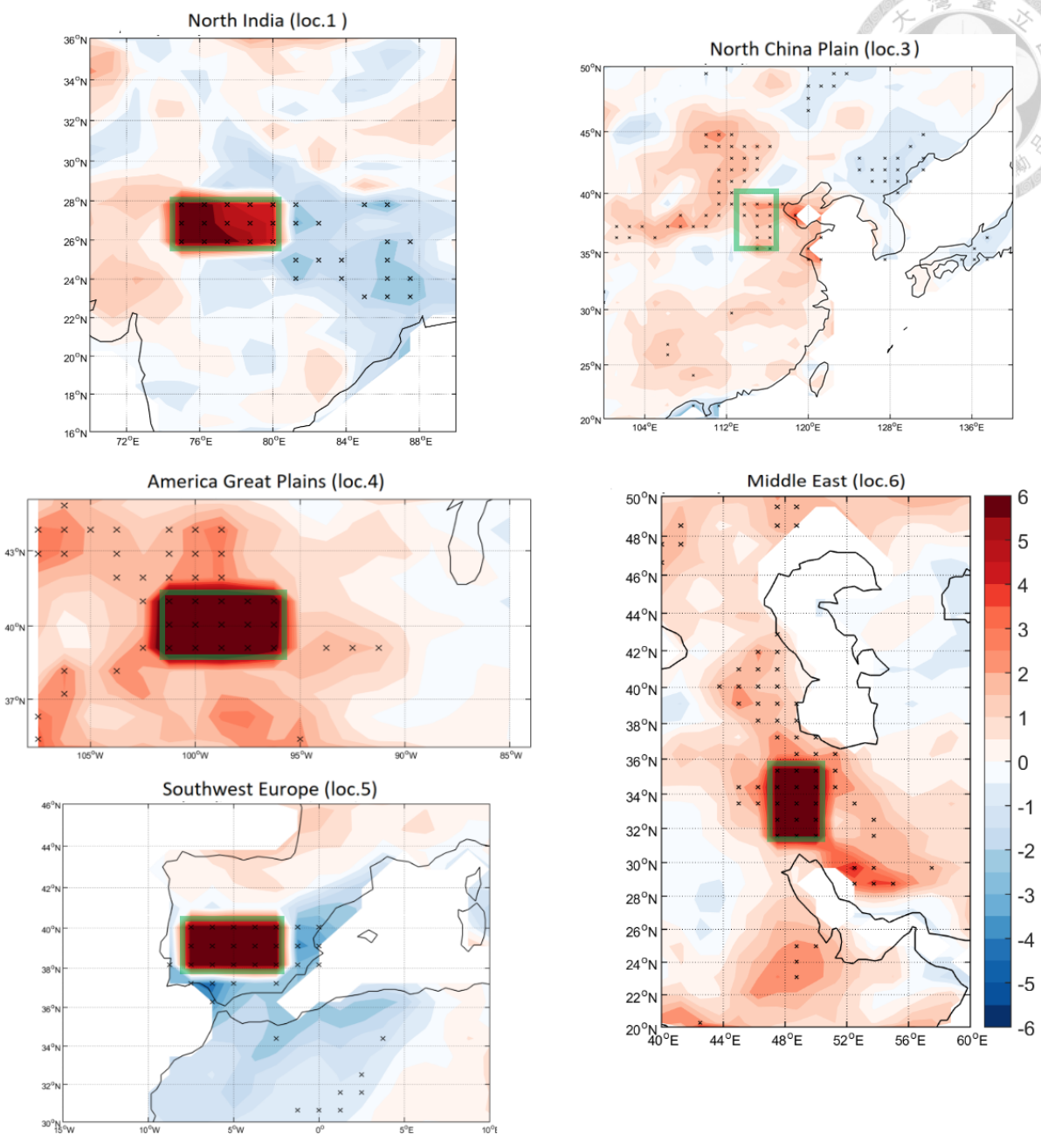
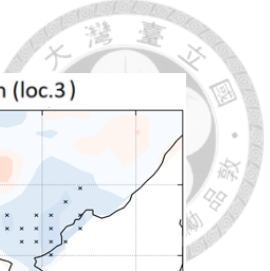


Figure 3.16.2 The differences of annual mean evapotranspiration (positive upward) after irrigation: $F_{max} - F_{ctl}$. Black crosses represent annual data which pass the unpaired two-tail t-test under 95% significant level. Green box represents irrigated area in simulations.

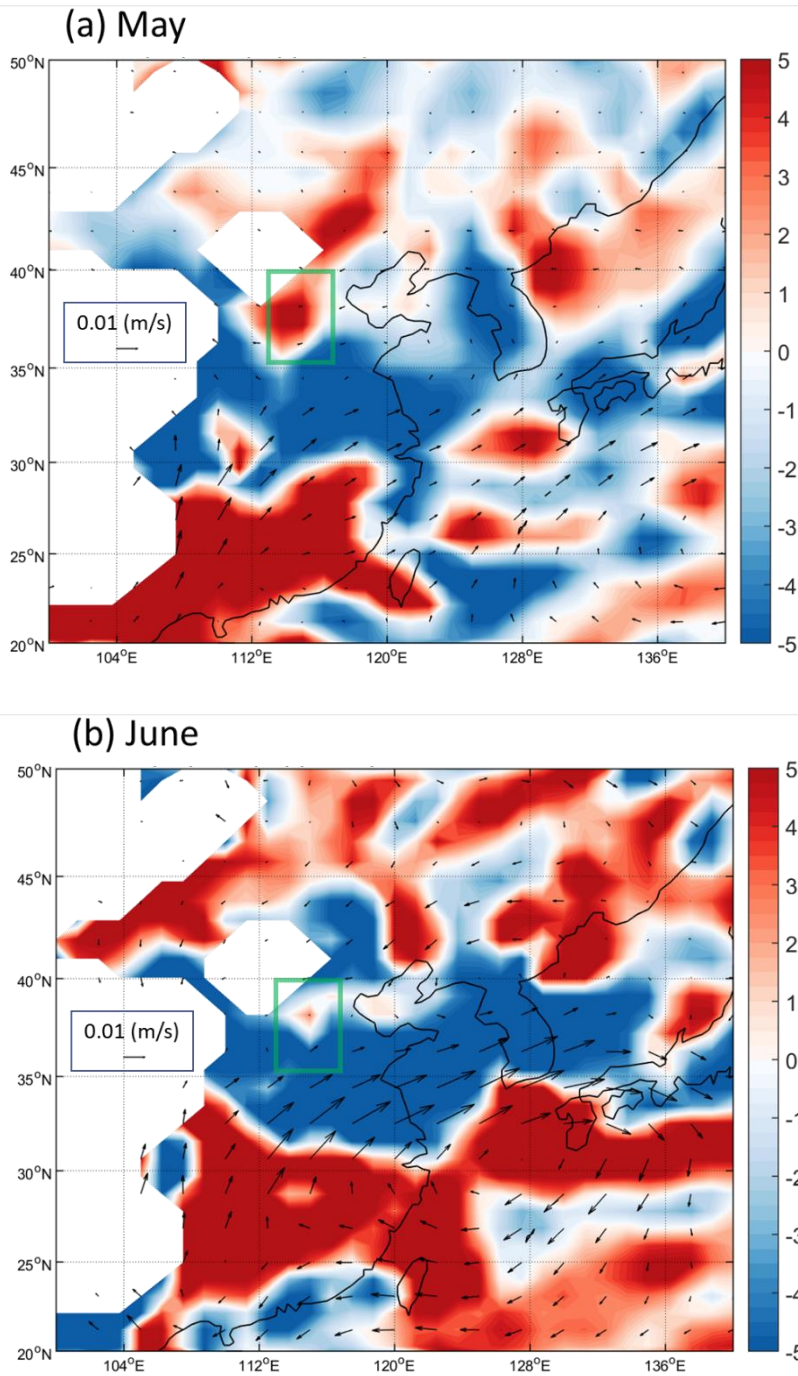


Figure 3.17 The differences of water vapor flux at 850mb from $F_{max} - F_{ctl}$ in (a) May and (b) June. Vector: water vapor flux (m/s) anomaly; shaded: the divergence of water vapor flux (10^{-9} 1/s) anomaly. Green box represents the irrigation area.

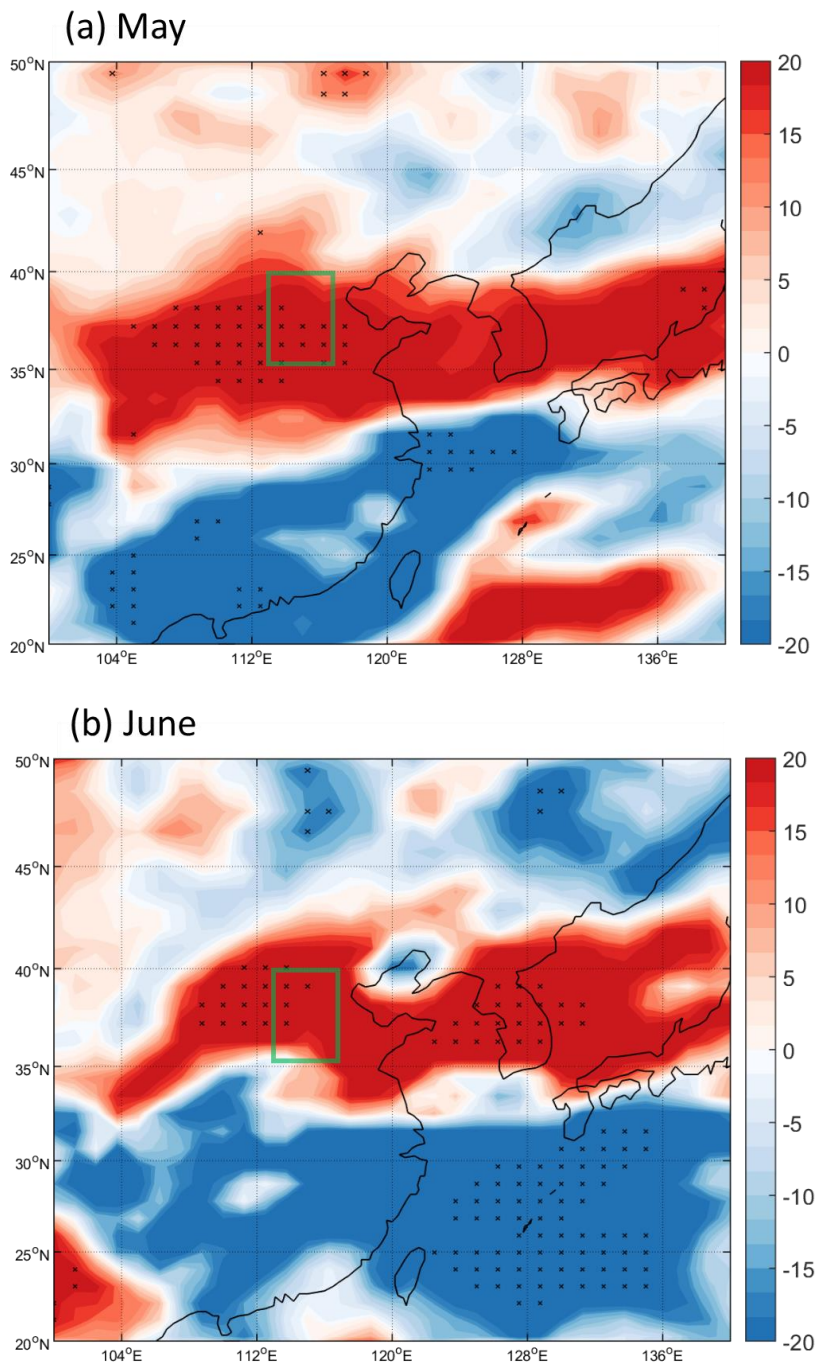


Figure 3.18 The differences of precipitation (W/m^2) from $F_{max} - F_{ctl}$ in (a) May and (b) June. Black crosses represent annual data which pass the unpaired two-tail t-test under 95% significant level. Green box represents the irrigation area.

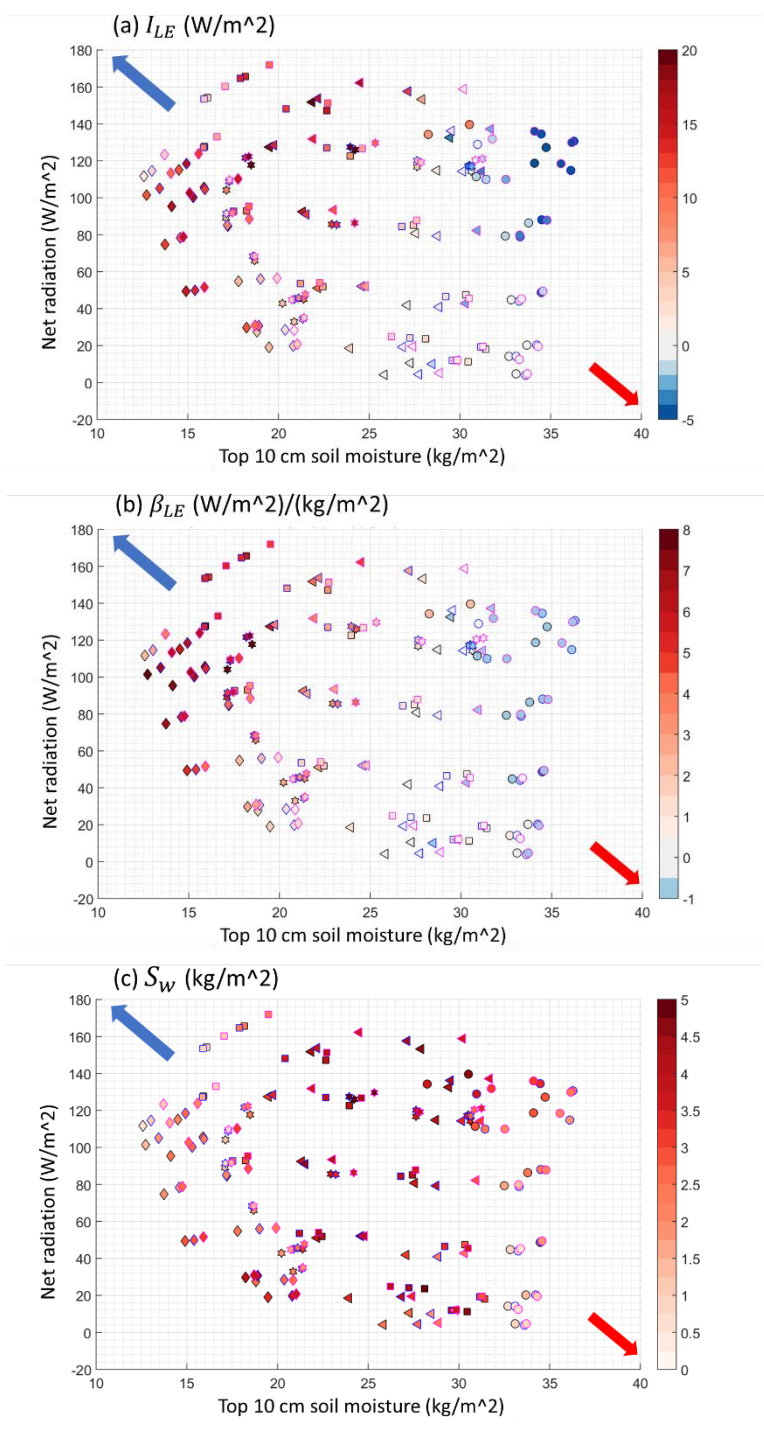


Figure 3.19 Hydroclimatological scatter chart of I_{LE} from F_{ctl} (black frame), F_{self} (blue frame) and F_{max} (pink frame). (a) I_{LE} : coupling strength between soil moisture and evapotranspiration, (b) β_{LE} : the slope between soil moisture and evapotranspiration, (c) S_w : the standard deviation of daily soil moisture. Different symbols represent different places. Color of frame represent different simulations.

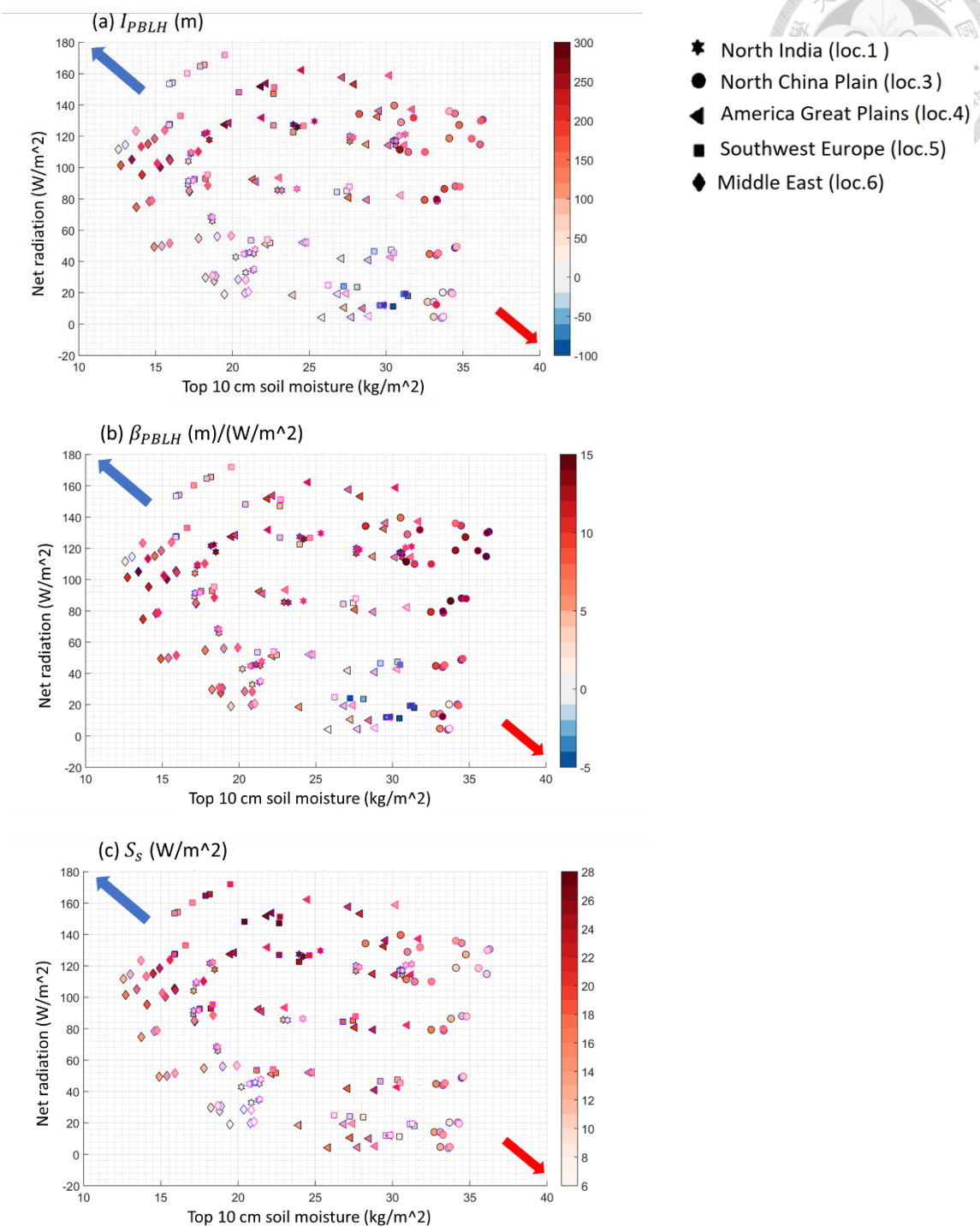


Figure 3.20 Hydroclimatological scatter chart of I_{PBLH} from F_ctl (black frame), F_self (blue frame) and F_max (pink frame). (a) I_{PBLH} : coupling strength between sensible heat flux and boundary layer height, (b) β_{PBLH} : the slope between sensible heat flux and boundary layer height, (c) S_s : the standard deviation of daily sensible heat flux. Different symbols represent different places. Color of frame represent different simulations.

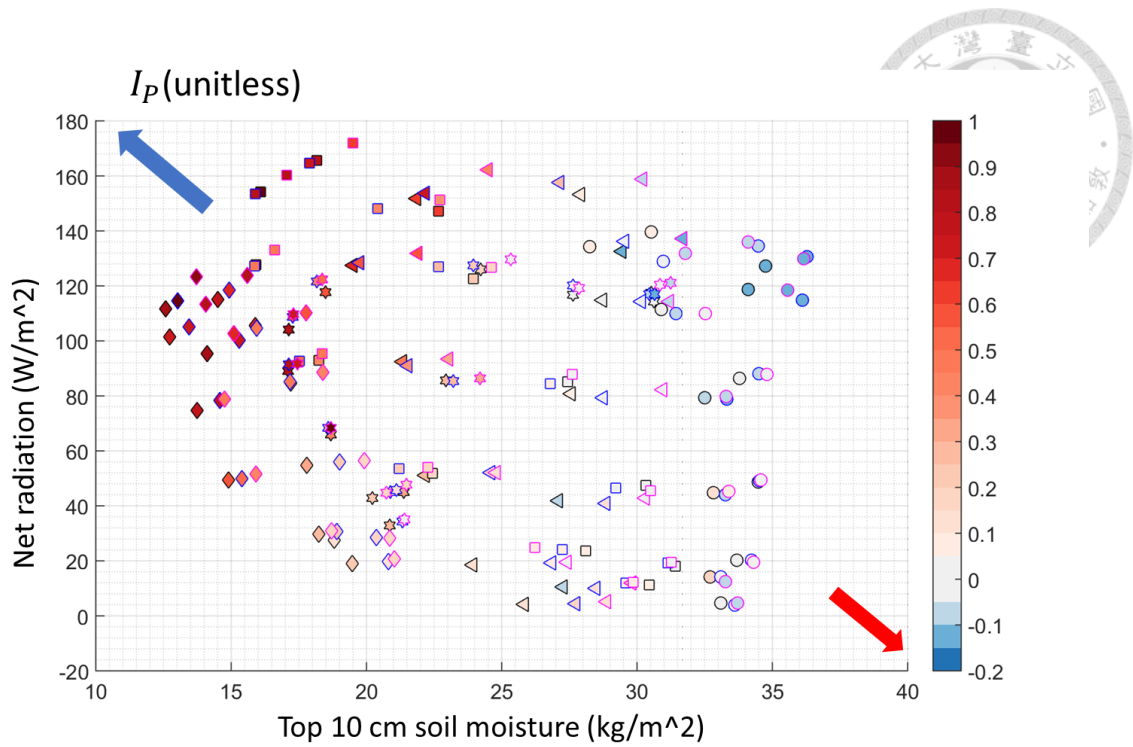


Figure 3.21 Hydroclimatological scatter chart of I_p from F_ctl (black frame), F_self (blue frame) and F_max (pink frame). Different symbols represent different places. Color of frame represent different simulations.

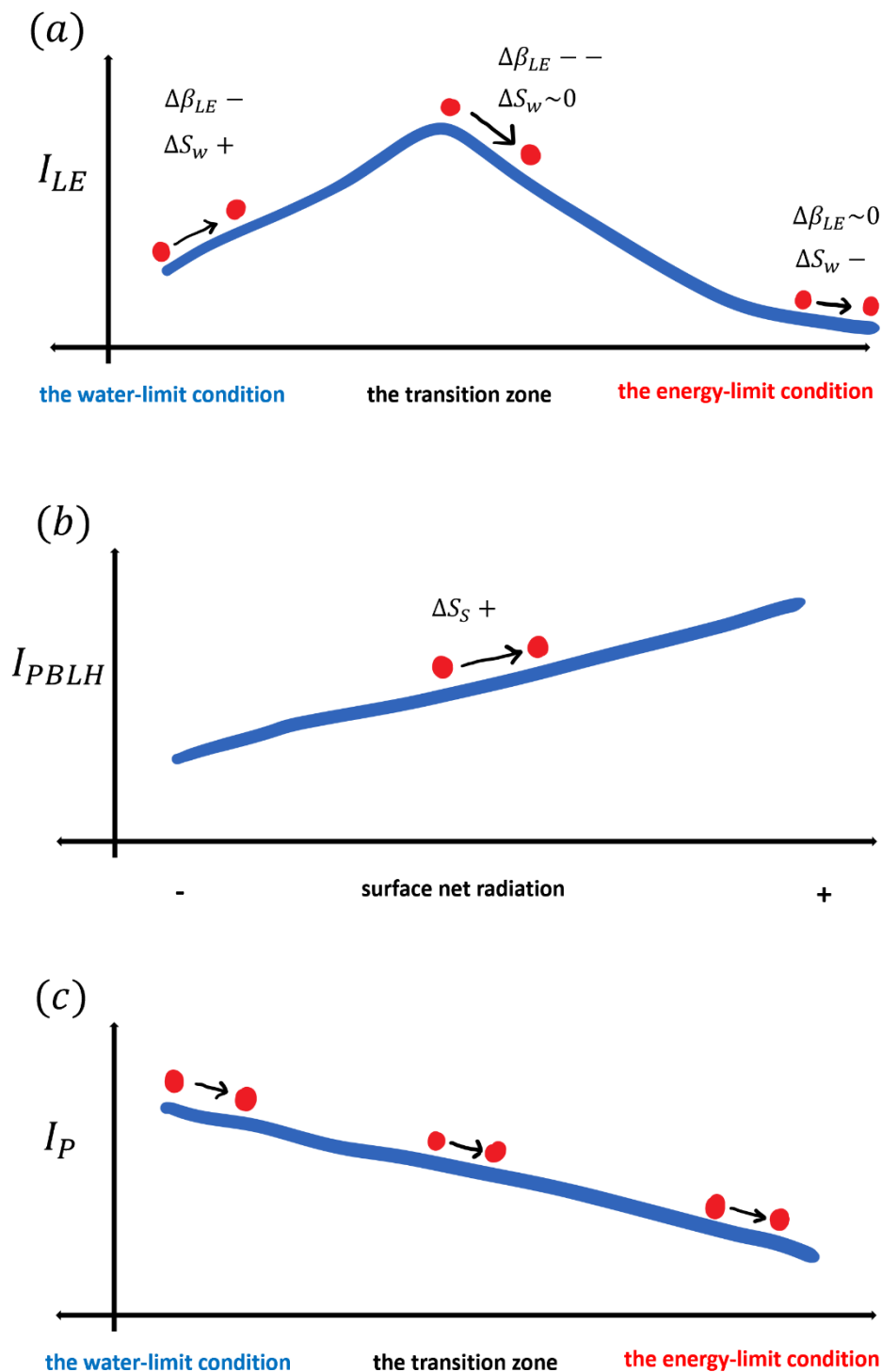


Figure 4.1 The illustration of the strength of three land-atmosphere coupling indices (I_{LE} , I_{PBLH} and I_P) and their controlling factors: (a) I_{LE} , (b) I_{PBLH} , (c) I_P . The shift of red dot represents the response of coupling strength due to the change of controlling factors. Blue line represents the changing tendency (i.e., increase or decrease) of coupling index among the shift of the controlling factors, but it does not guarantee “linear” shift of coupling strength.

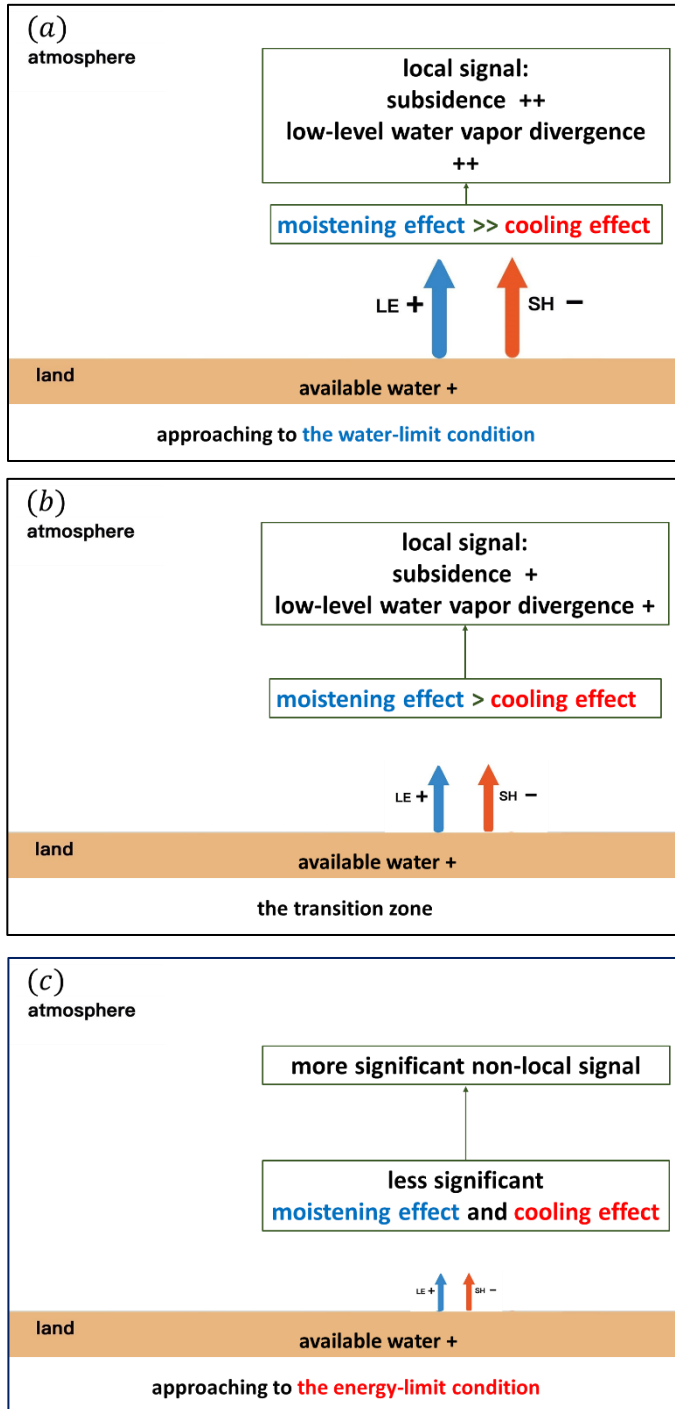


Figure 4.2 The illustration of the responses of land surface fluxes and atmosphere structure with more available water under different hydroclimatological characteristics: (a) approaching to the water-limit condition, (b) the transition zone and (c) approaching to the energy-limit condition. LE: surface latent heat flux; SH: surface sensible heat flux.

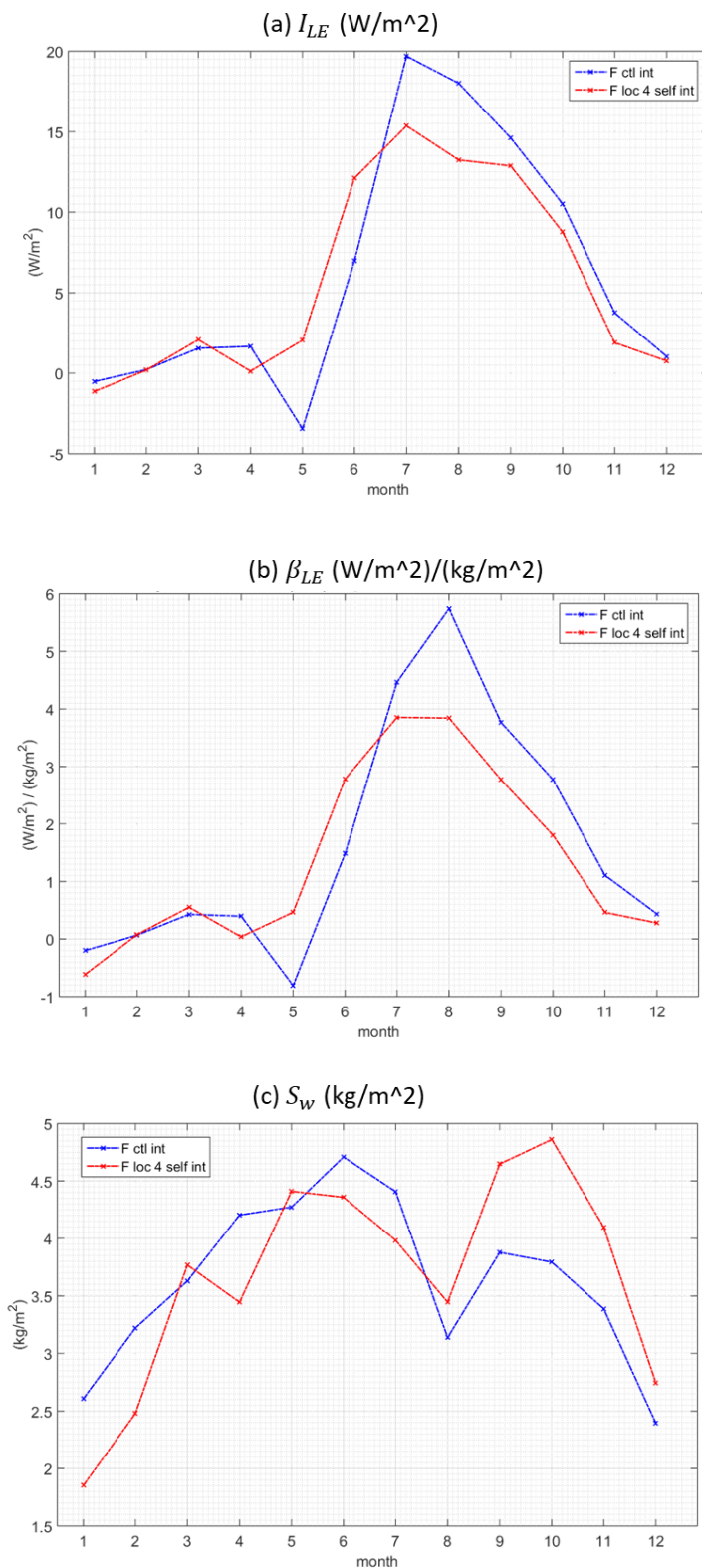


Figure 4.3 Seasonal cycle of I_{LE} in America Great Plains (location No 4) in F_ctl (blue line) and F_Self (red line). (a) I_{LE} : coupling strength between soil moisture and evapotranspiration, (b) β_{LE} : the slope between soil moisture and evapotranspiration, (c) S_w : the standard deviation of daily soil moisture.

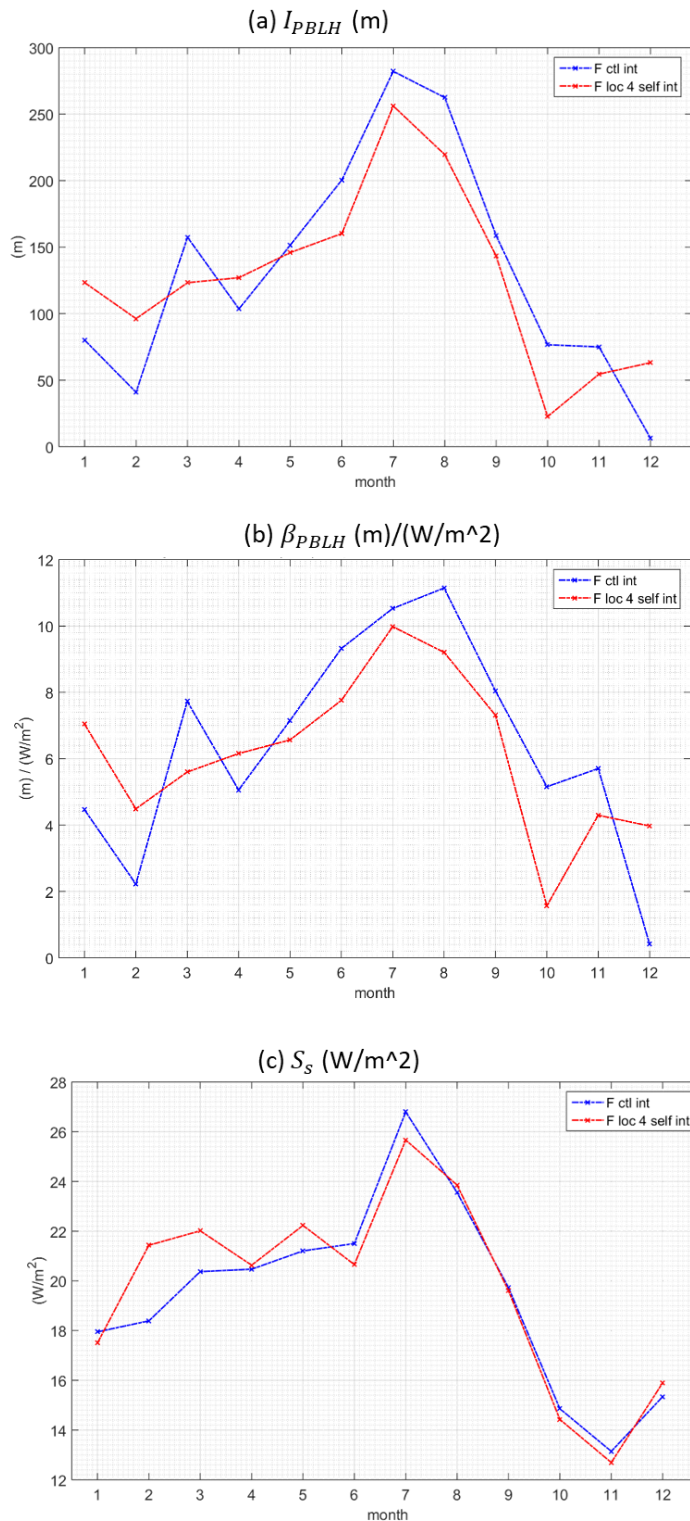


Figure 4.4 Seasonal cycle of I_{PBLH} in America Great Plains (location No 4) in F_ctl (blue line) and F_Self (red line). (a) I_{PBLH} : coupling strength between sensible heat flux and boundary layer height, (b) β_{PBLH} : the slope between sensible heat flux and boundary layer height, (c) S_s : the standard deviation of daily sensible heat flux.

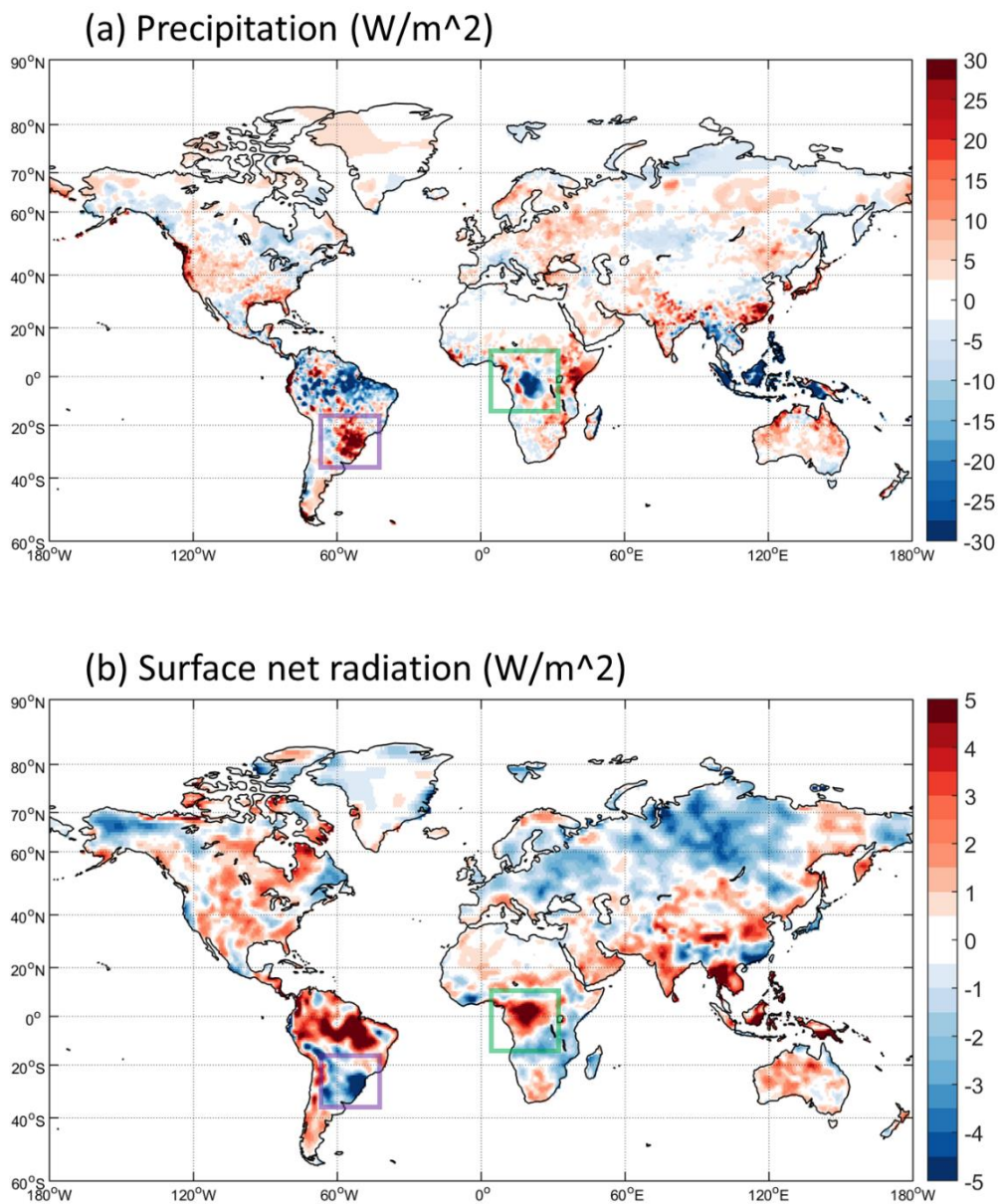


Figure 4.5 Anomaly of (a) precipitation and (b) surface net radiation during El Niño in 1997 and 1998. Reference climatology is calculated from 1984 to 2010. Precipitation comes from GPCP reanalysis data; net radiation comes from ECMWF reanalysis data.

Tables

Table 2.1 The abbreviation of each simulation settings.



abbreviation	long name
I_ctl	offline land surface model control simulation
F_ctl	coupled land-atmosphere control simulation
I_max	offline land surface model simulation with the maximum irrigation scenario
I_self	offline land surface model simulation with the own climatology irrigation intensity seasonal cycle of each area
I_min	offline land surface model simulation with the minimum irrigation scenario
F_max	coupled land-atmosphere simulation with the maximum irrigation scenario
F_self	coupled land-atmosphere simulation with the own climatology irrigation intensity seasonal cycle of each area